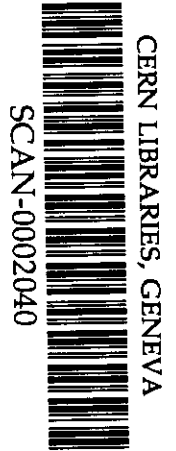


0 CERN-SPSC-1

A PROPOSAL TO BUILD A RING IMAGE CERENKOV DETECTOR FOR USE BY
THE OMEGA PHOTON COLLABORATION IN WA69 (P140)

Bonn¹-CERN²-Lancaster³-Manchester⁴-Rutherford Laboratory⁵-Sheffield⁶

M. Atkinson⁵, T. Axon⁴, D. Barberis⁴, T.J. Brodbeck³, J. Bunn⁶, A.B. Clegg³,
S. Danaher⁶, M. Davenport⁵, B. Dickinson⁴, B. Diekmann¹, A. Donnachie⁴,
J. Eades², R.J. Ellison⁴, P.S. Flower⁵, P.J. Flynn³, W. Galbraith⁶,
G. Halliwell⁵, K. Heinloth¹, R.C.W. Henderson³, S. Holtzkamp¹,
R.E. Hughes-Jones⁴, J.S. Hutton⁵, M. Ibbotson⁴, H.-P. Jakob¹, M. Jung¹,
G. Körsgen¹, G.D. Lafferty⁴, V. Liebenau¹, R.H. McClatchey⁶, R. Maybury⁵,
D. Mercer⁴, J.A.G. Morris⁵, J.V. Morris⁵, D. Newton³, G.N. Patrick²,
E. Paul¹, M. Reidenbach¹, H. Rotscheidt¹, A. Schlösser¹, P.H. Sharp⁵,
R.J. Thompson⁴, J. Waterhouse⁴ and M.J. Worsell⁴



WA69 Spokesman: E. Paul
WA69 Contactman: J.V. Morris
WA69 Ring Image Detector
Contactman: P.H. Sharp

283376

A proposal to build a ring image Cerenkov detector for use by the Omega Photon Collaboration in WA69(P140).

<u>Contents</u>	<u>Page</u>
1. INTRODUCTION.	2
2. OUTLINE OF DETECTOR.	5
3. DESIGN DETAILS.	
3a. Monte Carlo studies of detector response.	10
3b. Details of optics.	15
3c. Time projection chamber.	18
3d. Electronic Readout.	22
3e. Radiator gases and mounting system.	24
4. TIMESCALES AND COST.	
4a. Construction and commissioning timescales.	26
4b. Cost and manpower estimates.	27
5. SUMMARY OF PROPOSAL.	29
Appendix 1. TPC development programme.	30
2. Mirror development programme.	38
3. Vacuum TV measurements.	41
References	
Figure Captions	

1. INTRODUCTION

The Omega photon collaboration has an approved physics program in the upgraded West Area at CERN. This physics program, proposal 231, has been presented to the PPESP at meetings 28 and 32, with addenda given at meetings 33 and 35⁽¹⁾. As part of this proposal to study the photoproduction of high multiplicity states at high energy, we reviewed particle identification at Omega and concluded that an enhancement of the present system of two threshold Cerenkov detectors was most desirable. The minutes of meeting 35 state, "the proposal was approved including continued support for the development of a ring imaging Cerenkov counter for the experiment". In this addendum we report on this development work and show that the major technical problems are now solved. We make the case for replacing both the existing threshold counters C_1 and C_2 with a ring imaging detector (fig 1). This single detector will be capable of identifying pions from 5 GeV/c, the minimum momentum of particles emerging downstream of the Omega magnet, up to 80 GeV/c, and providing kaon-proton discrimination up to 150 GeV/c. A comparison of the ring imaging counter with the existing Cerenkov system at Omega is shown in table 1. As an indication of the implication for physics, the range of Feynman x over which kaons from charm decays could be identified has been presented in Addendum 3 (PPESP/81/20, meeting 35). In addition, the spatial resolution of the ring image detector will be such that particles separated by as little as 2 or 3 millimetres at the entrance to the detector will be independently identified.

For the sake of clarity we have separated the report on development work from the proposal to construct a ring imaging counter for Omega, although clearly the details of the latter depend strongly on our experience with the former. The report on the development work is in appendices 1, 2 and 3, dealing with the work carried out at RAL, particularly since Sept 1981, on time projection chambers, mirror construction, and vacuum UV measurements.

For the proposed ring image detector for Omega, an outline description is given in section 2, with more detail given in section 3. We investigate

the identification power of the detector used with offline analysis, and also as a device which could be used in the experiment trigger. We use a Monte Carlo simulation of high multiplicity jets to study the response of the detector at both low and high interaction rates. In section 4 we outline our proposed plans for building and commissioning the detector, together with an estimate of the cost and manpower required.

The pioneering work of T Ypsilantis, J Seguinot and T Ekelof on ring imaging Čerenkov detectors has made building such a detector for our experiments completely realistic. We gratefully acknowledge their continued help and friendly collaboration during the past two years.

1	2	3	4	5
Momentum Range GeV	C1 (n = 1.0009)	C1 (n = 1.0009) +C2 (n = 1.00013)	Ring Image n = 1.00034	transition radiation det.
5 - 14	π identified K/p ambiguous	π identified K/p ambiguous	π identified K/p ambiguous	-
14 - 19	π /K ambiguous p identified	π identified K identified P identified	π identified K/p ambiguous	-
19 - 26	π /K ambiguous p identified	π identified K identified p identified	π identified K identified p identified	-
26 - 35	no information	π identified K/p ambiguous	π identified K identified p identified	-
35 - 65	no information	π /K ambiguous p identified	π identified K identified p identified	-
65 - 80	no information	no information	π identified K identified p identified	-
80 - 150	no information	no information	π /K ambiguous p identified	π identified K/p ambiguous

TABLE 1

Performance of practicable particle identification configurations for WA69. The vastly superior information given by the Ring Image (column 4) compared to the combination of C1 and C2 (column 3) is manifest. (Note that the table is modified from that in proposal P231 in order to take account of more recent understanding, including increasing the length of C₂ from 5 m to 8 m).

2 OUTLINE OF DETECTOR

2.1 Introduction

The ring image cerenkov detector principle has been used in many forms of differential cerenkov detector for the last twenty years. However most of these detectors only work successfully when used in a well collimated beam of particles. The design of a ring image detector for use with the Omega spectrometer requires the development of a large area single photon detector with good spacial resolution. This could be achieved, as suggested by Ypsilantis et al⁽²⁾, by using the photoionising properties of gases in the ultraviolet together with some form of wire chamber to digitise the photon conversion position. These authors⁽³⁾ have recently successfully demonstrated the detection of cerenkov photons in a time projection chamber using an organic photoionising agent TMAE (Tetrakis (dimethylamine) ethylene). In our design of a ring image cerenkov detector for omega we make use of these developments.

2.2 Cerenkov Radiation and Ring Image Formation.

When a particle travels in a dielectric medium of refractive index (n) at velocity (v) which is greater than the velocity of light in that medium, cerenkov radiation is emitted in a cone of semi angle θ to the particle direction, where $\theta = \cos^{-1} \frac{1}{\beta n}$ and $\beta = v/c$.

The number of photons with Energy E, emitted within this cone, per unit photon energy is given by (where L is the length of radiator):-

$$\frac{dN}{dE} = \frac{L}{137 \hbar c} \sin^2\theta$$

$$\approx 370 L \sin^2\theta/\text{ev}$$

To produce a ring image from this cone of light we need to introduce a focussing element, either a lens or a mirror. In practice large

acceptance detectors working in the ultra violet invariably use mirrors, but to demonstrate the principle we consider a lens as shown in fig 2. Light at constant angle θ in the plane of the paper is focussed to a point A in the focal plane of the lens. The distance of A from the lens axis is $R = f \tan\theta$. If we rotate the diagram about the lens axis, the locus of point A describes a circle, hence a cone of rays at angle θ produce a ring image in the focal plane of the lens. A simple ring image cerenkov detector is shown in fig 3.

In traversing a gas radiator of length L, a particle radiates photons towards a spherical mirror. If the radius of curvature of this mirror is $2L$, a ring image will be focussed at a spherical surface of radius of curvature L having the same centre of curvature as the mirror. We place a photon detector on this focal surface.

Before the Cerenkov photons can be detected, they must pass through the radiator gas, be reflected from the mirror surface, pass through the detector window and be converted into electrons by the photoionising agent in the detector gas. As the efficiency of each of these processes depends on the photon energy, E, the overall response of the device is found by integrating the product of the individual efficiencies over the range of E to which the device is sensitive

The number of photoelectrons produced by a given detector is

$$N_e = 370 \int Q(E)R(E)T_g(E)T_w(E)dE \times L \sin^2\theta$$

$$= N_0 L \sin^2\theta$$

where,

$R(E)$ is the reflectivity of the mirror,

$T_g(E)$ is the transmission of the radiator gas,

$T_w(E)$ is the transmission of the window,

$Q(E)$ is the quantum efficiency of the photoionising vapour.

Figure 4 shows the energy dependence of R for a good quality mirror, T_w for a fused silica window, and Q for TMAE, the proposed photoionising agent.

The transmission of the radiator gas is discussed in section 3e. We assume for this discussion that the radiator gas is Argon at STP. With these parameters the integral under the convoluted response curve is equivalent to an $N_0 > 150$. We will however assume a conservative value of $N_0 = 90$ for the design discussion, since a detector tested by Ypsilantis et al⁽³⁾ has achieved this value. The radii of the ring images and the number of photoelectrons detected for pions, kaons, and protons, as a function of momentum, will be as shown in figure 5. We see that such a ring image detector would identify pions from 5 GeV/c up to the momentum at which the pion and kaon ring radii are too close to be resolved. The rings have a convenient radius and contain a large number of photoelectrons.

2.3 Resolution and detection of ring image

In the above discussion it was observed that the response of a photoionising agent such as TMAE used with fused silica windows produces a useful photon energy range of 1.2 eV (fig 4). In this energy (wavelength) interval the refractive index of the radiator gas changes as shown in figure 6. This produces a chromatic dispersion, which in turn produces a smearing of the ring image. We have studied this smearing using a Monte-Carlo simulation of cerenkov photons emitted from an 80 GeV/c pion. The effects are shown in the scatter of points about the ring image in figure 7. The RMS scatter is ± 1.8 mm. In fitting a circle to these points the error on the fitted radius is reduced by the square root of the number of constraints, hence having a large number of photoelectrons on the ring not only helps pattern recognition problems (section 3), but improves the determination of ring radius which is important at high momenta.

Figure 8 shows a histogram of fitted radii of ring images for pions, kaons, and protons and indicates that pions and kaons are well separated at 80 GeV/c.

The dispersion limit is well matched by the spacial resolution available for photoelectron detection in wire chambers, and led us to the choice of a time projection chamber (TPC) for digitising the photon conversion points.

A schematic view of a TPC is shown in figure 9. The cerenkov photons pass through a UV transmitting window. This window separates the radiator gas, which has a long absorption length for UV photons, from the TPC drift gas containing TMAE. The mean free path for conversion in the drift gas is ~ 10 mm, which contributes an error of less than 1 mm to the ring radius, since the cerenkov angles are small.

The electrons produced around the cerenkov ring drift in a constant electric field of typically 0.5Kv/cm towards a MWPC. The arrival time at the MWPC of an electron determines the x coordinate of its conversion point, while the MWPC wire address determines its y coordinate. The TPC should therefore contain a gas with a suitable drift velocity, low electron diffusion, and give a good gas gain in the MWPC. A suitable gas mixture is Methane, Isobutane, and TMAE. A spacial resolution of 1 mm can be obtained with a 60 nsec time digitisation, and the equivalent resolution in y can be obtained with a 4 mm wire spacing in the MWPC.

2.4 Proposed detector

Particles originating at the centre of the Omega target with zero transverse momentum, emerge through the drift chambers downstream of the omega magnet provided they have momentum greater than 5 GeV/c. These particles when projected back into Omega have an apparent source point on the Omega axis, and 45 cms downstream from the centre of Omega. In designing a ring image detector for Omega we have placed the centre of curvature of the mirror system at this point, thus ensuring that this subset of particles traverse the radiator gas normal to the mirror. The optical aberrations introduced by the mirror system are thus minimised, and in section 3d we show that they are acceptably small for all interaction points in the target, and for the range of transverse momentum emerging downstream of Omega.

A perspective drawing of the detector is shown in figure 10, and a plan and side elevation is shown in figure 11. The entrance aperture of the detector is designed to match the aperture of the Omega drift chambers, being 3.2 metres wide by 1.6 metres high.

An assembly of time projection chambers is placed at the focal surface of this mirror system. This assembly contains sixteen TPCs each 80 cms high and 40 cms wide; eight TPCs are above the median plane, and eight are below. A plan and front elevation of a single TPC is shown in fig 12, together with an isomeric view in fig 13. The electric field is arranged to drift electrons from each side of the TPC towards the MWPC in the centre of the chamber. This MWPC will contain 192 sense wires. The readout system will consist of

- (1) Sensitive amplifiers ($\sim 0.1 \mu\text{A}$) which produce standard pulses from each of the 3072 MWPC sense wires.
- (2) A time slice encoder (TSE) to strobe in data from the amplifiers at a time period of ~ 60 nsec, encode wire address and time for each signal and store data in an output memory.
- (3) A CAMAC readout system to read data from the TSE for offline data analysis.
- (4) A microprocessor system to process data from the TSE memory for use in the second stage trigger of an experiment.

The transverse dimensions of the overall mirror system are 6.4 metres wide by 3.2 metres high, arranged on a spherical surface with radius of curvature 10 metres. This surface is covered by 81 hexagonal mirrors (70 cms point to point), each of which is coated to give good ($> 70\%$) reflectivity at $\lambda > 1600\text{\AA}$. To minimise the quantity of material within the acceptance of the Omega photon detector (figure 11), 3 mm thick glass mirrors will be used. We have limited the transverse dimensions of the individual mirrors to 70 cms, in order to make use of existing technology. Further discussion of the production and testing of mirrors is given in appendix 2.

3. DESIGN DETAILS

3a Simulation studies

3a.1 Introduction

In order to investigate the efficiency, and optimise the design of the Ring Image Cerenkov detector, we have developed a computer simulation based on the specification outlined in section (2). This simulation consists of the following steps:-

- a) Generation of final state 4-vectors corresponding to various high energy interactions, and tracking of the charged particles through the Ω field to the Ring Image Cerenkov detector. (3a.2)
- b) Generation of the corresponding ring images with the expected resolution. (3a.3)
- c) Generation of rate dependent background (3a.4)
- d) Analysis of the ring images to identify the particle types. (3a.5)

We deal with each of these points in turn.

3a.2 Generation of events

In order to ensure that the detector has an acceptable efficiency for the range of physics channels to be investigated in WA69 (P231), we have chosen to generate events of two types:-

- (A) High Multiplicity jet-like
- (B) Charm

For type (A), the Monte-Carlo program SAGE [4] was used to generate:-

$$\gamma p \rightarrow Xp \quad \begin{array}{l} \downarrow \\ \rightarrow 8\pi 4K \end{array}$$

where the multi-meson system X was produced by a diffractive mechanism from the incident 170 GeV photon, and the mesons had limited p_T with respect to the direction of X (p_T truncated phase space [5], $\langle p_T \rangle \sim 0.4$ GeV/c). These events gave an average of 8.5 tracks into the RIC (fig 14 and 15), and provide a good test of its ability to cope with high multiplicity.

For type (B), in the absence of a detailed knowledge of production mechanisms, and the excessive number of possible decay modes, we have taken a specific event observed in the LEBC (NA16) experiment at CERN [6]. This is an example of $D^0 \bar{D}^0$ production, and is shown in fig 16 and 17.

Tracking of the charged particles to the RIC was done by a Runge-Kutta method, using the full Ω field map.

3a.3 Generation of Ring Images

Knowing the slopes $Y' = \frac{\partial Y}{\partial X}$, $Z' = \frac{\partial Z}{\partial X}$ of the tracks on entry to the detector, perfect spherical optics were assumed to give the centre of the ring image at

$$Y_c = RY'/2 \quad Z_c = RZ'/2$$

where R is the radius of curvature of the Cerenkov Mirror (10 m). The radius of the ring and the mean number of points on the ring were calculated from the known momentum of the particle, and the actual number

of points chosen according to the corresponding Poisson distribution. These points were then smeared according to the expected resolution and the corresponding "ghost" points (Left-Right ambiguity in TPC) were generated.

3a.4 Generation of background

The detector has a sensitive time of about 3 μ sec, and the type and amount of background depends strongly on the type of beam, and on the beam rate.

For WA69, the major background is electromagnetic ($\sigma \sim 20$ mb compared to hadronic cross section of ~ 100 μ b), but at the expected beam rate ($\sim 10^7$ 200 GeV e^- /pulse) this gives a negligible background rate within the sensitive time of the RIC. ($\sim 10^{-2}$ interactions/3 μ sec).

The background situation for hadron beams (WA70 200 GeV π) is much more severe, in that about 6 background events per 3 μ sec are expected. In order to determine the effects of this on the detector efficiency we have used events of type (A) to represent the background. The particles from these events were tracked in the normal way to the detector, but the arrival time chosen at random within ± 3 μ sec of the event trigger time. The ring images were generated as in 3a.3, and digitisings arriving outside the 3 μ sec gate were rejected.

3a.5 Analysis of Ring Images

The main steps in the procedure for identification of the ring images are shown in fig (18), the major feature being the use of the reconstructed momentum vectors from the triggering event to predict where the rings should be, and the number of points expected.

The short sensitive time of the Q MWPCS ensures that the reconstructed tracks come only from the trigger event, thus allowing the corresponding rings to be isolated from the background.

The efficiency of this ring isolation depends upon the accuracy with which the ring centre and radius can be predicted from the reconstructed tracks. For the full Ω detector, with a detailed track reconstruction (TRIDENT⁽⁷⁾), the errors on these quantities will be small. For this study, we have chosen not to simulate the full Ω detector, and instead have assumed that the only information on track momentum vectors is provided by a point at the centre of the target and measurements of direction and position outside the magnetic field to $\sim \mp 0.4$ mRad, and $\sim \mp 0.5$ mm. This gives a momentum resolution (P in GeV/c),

$$\left(\frac{\sigma_D}{P}\right)^2 \sim 0.02^2 + \left(\frac{P}{1500}\right)^2,$$

where a helix model for the track is used, and would be an example of the type of analysis available for online monitoring.

The above errors have been used to compute the search band widths ΔR_α and ΔN_α (see flow chart) for ring identification. Where search bands overlap ($p \gtrsim 50$ GeV), so that, for example, many of the points on a π ring were within the k-band, fitting all points in the $\pi + k$ bands would determine the radius accurately ($\pm \sim 2/5$ mm), and allow π/k to be separated to a much higher momentum ($\gtrsim 80$ GeV). Although fitting of the points on the rings is indicated in the flow chart, this has not yet been implemented, and in the results described in 3a.6, no attempt is made to resolve ambiguities, the 1st choice identification being always taken.

In an offline analysis, the good momentum and angular resolution of Ω will allow narrower search bands (particularly important close to threshold) and time will be available to do a more detailed analysis of the rings. Background problems will be indicated by an excessive number of points in

the search bands, and might be eliminated by first removing all digitisings in the bands, identifying and fitting the background rings, and then eliminating all points associated with these rings within the original search bands.

3a.6 Results

The simulated digitisings for an event of type (A) are shown in fig 15, where the rings due to the trigger tracks can be clearly separated.

As an example of the identification power we show in figs 19 and 20 histograms of the distance between the predicted centre of the ring and all digitisings in the detector, for an event containing a 20 GeV π and a 20 GeV k (as well as other particles). Fig 19 shows the distance to all digitisings from the ring centre for the 20 GeV π , Fig 20 shows the same digitisings, but with the centre for the 20 GeV k as origin. Superimposed on both plots is the curve for the expected number of digitisings as a function of ring radius. Not only do the histograms show peaks in the expected radial bands, but the height of the peaks also clearly separates the signal from the background.

Simulation study of the NA16 charm event (fig 16) shows an efficiency of $\sim 80\%$ to correctly (1st choice) identify all the decay products of the $D^0\bar{D}^0$ system.

In order to show that even large amounts of hadronic background can be tolerated we show in Fig 21 the background due to six high multiplicity events within the sensitive time of the detector (3a.4). The efficiency for correctly identifying the tracks from an event of type A which enter the RIC (1st choice identification), is shown in Fig 22, as a function of this background rate. This efficiency is high even though no attempt has been made to eliminate the background, or fit the rings to determine the radius more accurately.

The basic RI calculations discussed above correspond to rather few computer instructions so if Omega is provided with fast on line track

finding (perhaps using some additional MWPC's) there would be no difficulty in computing the particle type over quite wide momentum ranges in a time $\sim 50 \mu\text{sec}$, so providing a second stage trigger.

We conclude that a Ring Image Cerenkov counter with the specification outlined in section 2 will give efficient particle identification for the range of physics channels to be investigated by WA69, and is also suitable for use with hadron beam experiments.

3b Details of Optics

3b.1 Introduction

In section 2 we described how the centre of curvature of the mirror system was arranged to be at the effective source of zero transverse momentum particles produced at the centre of the Omega target. This point is on the axis of the Omega magnet, and 45 cms downstream from the centre of Omega. For this subset of particles the mirror system is well optimised and the ring images produced suffer negligible aberrations. In section 3b.2 we evaluate the effects of optical aberrations for particles with a finite impact parameter, while in section 3b.3 we describe the proposed method of manufacturing and mounting the mirrors.

3b.2 Aberrations

Figure 23 shows the effective layout of the optical system. A particle travelling in the (xy) plane radiates between the detector surface ($R_D = R_m/2$), and the mirror surface (R_m). This light is reflected by the mirror to form a ring image at the detector surface. The ring image for fixed velocity is only a function of direction, thus a parallel particle displaced by distance b will be imaged to the same ring. We refer to b as the impact parameter.

Particles passing through the centre of curvature of the mirror, effectively pass along the optic axis of the mirror, and so minimise any aberrations. For a spherical mirror system both coma, and astigmatism are non-existent for rays passing through the centre of curvature, and only spherical aberrations have to be taken into account. With a gas radiator the cerenkov angle is small (~ 26 mrad for Argon) and the effects of spherical aberration are small. The error in ring radius for spherical aberrations is given up to third order by

$$\frac{\Delta r}{r} = \frac{1}{8} \left(\frac{d}{f} \right)^3$$

where d is the useful diameter of the mirror actually illuminated, and f is the focal length of the mirror. Although the mirror is large, only a small area is illuminated by the light from each radiating particle, the radius of the illuminated disc being $r = \frac{d}{2} = f \tan \theta = 13$ cms. Hence

$$\Delta r \approx 2 \times 10^{-3} \text{ mm.}$$

To evaluate the aberrations for particles with finite impact parameters we use the analysis of Ypsilantis³. Figure 24 shows $\Delta \theta_D / \theta_D$ (the effects of defocussing of the ring image) evaluated as a function of impact parameter b . This impact parameter will depend on the physics being studied. To first order the value of b for tracks produced at the centre of the target is $b = 180 \frac{P_T}{P}$ cms, varying from $b = 150 \frac{P_T}{P}$ cms, to $b = 210 \frac{P_T}{P}$ cms at each end of the target. The geometrical acceptance of the detector as a function of $\frac{P_T}{P}$ is shown in figure 25, for different values of P . It is clear that for tracks above 10 GeV/c the acceptance is 100% up to values of $\frac{P_T}{P}$ of $\sim 20\%$. For lower momentum tracks the acceptance is lower, but extends to higher values of $\frac{P_T}{P}$. For $\frac{P_T}{P} = 20\%$, $b/R_m = 0.036$ which gives $\Delta r = 5 \times 10^{-2}$ mm, and for $\frac{P_T}{P} = 50\%$, $b/R_m = 0.09$

which gives $\Delta r = 0.3$ mm. From this we conclude that for the highest values of transverse momentum accepted by the Cerenkov detector the distortion of the ring image due to the optical aberrations is small compared with chromatic dispersion.

At large values of impact parameters the ring image becomes elliptical.

We express this eccentricity as $e = \frac{r(\phi_c = 0) + r(\phi_c = \pi)}{r(\phi_c = \pi/2) + r(\phi_c = 3\pi/2)} - 1$ where ϕ_c

is the azimuthal angle around the ring image. Figure 24 shows the values of e as a function of the impact parameter b . We see that for $\frac{P_T}{P} = 20\%$ the eccentricity $e \sim 10^{-3}$ rising to $\sim 10^{-2}$ for the largest values of $\frac{P_T}{P}$, which will not provide a problem for the ring finding algorithms.

3b.3 Mirror Construction

Getting good reflectivity in the ultra-violet requires specialist coating techniques which are available at a small number of centres in the world. One such centre is the Culham Laboratory, where K Fletcher's reputation is worldwide.

The mirror size has been determined by the maximum size which can be coated using existing apparatus, and which can be reliably produced without extensive developments. For this reason we have also chosen to make the mirrors on a glass substrate rather than pursue some composite structure. The specification of the mirror surface requires that the aberrations should be small compared to 1 mm, which is better than that available for the best preformed (drooped) mirrors, but not as good as that required by optical telescope mirrors. The technique developed for making the mirrors (described in more detail in Appendix 2), preforms 3 mm thick glass sheets to the correct radius of curvature by drooping them into a former at 560°C. The mirror blank is then supported by a mould of the same radius of curvature, and ground and polished to the required specification by the same techniques as used for optical telescopes.

The circular glass plate is then cut to a Hexagon of the correct size, mounted on a stainless steel support ring, and coated with Aluminium and Magnesium Fluoride, the thickness of each coat being optimised to give the maximum reflectivity in the range 1600Å to 2400Å.

Any deflection of the mirror under its own weight must produce a deviation in the ring image of less than 1 mm. A finite element analysis of the mirrors has been performed for 3 mm, 4 mm and 6 mm glass. Figure 26 shows the deflection vectors as a function of position for the 3 mm mirror mounted at the top of the system. A plot of these deflections along the axis of the mirror is shown in fig 27.

The maximum change in slope of the mirror surface would deflect the rings by 0.2mm.

The stainless steel ring glued to the back of each mirror will be mounted on a three point suspension, which will allow easy alignment, and give good stability. We are developing techniques to check the alignment of the mirrors at any time during data taking.

3c The time projection chamber

3c.1 Introduction

The principles of the time projection chamber have been described in section 2. In this section we describe the details of the construction, the fused silica (quartz) windows, the drift gas, and the electrostatic field shaping. Finally in 3c.6 we summarise the tests of a prototype TPC.

3c.2 The construction of the TPC

A layout of the TPC is shown in fig 12. It consists of a MWPC running down the centre of the detector from top to bottom. This MWPC forms the "backbone" of the detector, and is constructed from 192 individual cells each 8 mm by 4 mm, having a 20 μ gold plated tungsten wire placed in the centre of each cell, as shown in fig 28.

Each sense wire is 5 cm long, (the depth of the TPC), and the wire spacing is 4 mm. All four sides of the cell are held at cathode potential, a plot of the equipotentials is shown in figure 29. The intercell spacers are constructed of 0.4 mm thick fibreglass, copper clad on both sides, while the sides through which the drifting electrons approach the sense wire are constructed from 100 μ beryllium copper wires spaced at 2 mm. Each of the sense wires is held at a tension of 30 gms, which is supported by the intercell divider. This arrangement provides a strong box structure which requires no further external structures to support the sense wire tension. This in turn reduces the mass of material shadowing the photon detector downstream of the ring image detector.

On either side of the MWPC are two 20 cm drift regions, each 80 cms high, (fig 12). The downstream side of the drift region is bounded by a 3 mm thick fused silica window, which has field shaping wires wound around it. The upstream side of the drift region is bounded by a thin dielectric, with field shaping wires wound on both sides. The far end of the drift region is a conducting surface held at a high negative potential. The field gradient across the drift region is held at ~ 0.5 Kv/cm, and the potentials of the shaping wires are adjusted to be consistent with this gradient.

3c.3 The fused silica (Quartz) windows

The fused silica windows are 80 cms long, 20 cms wide and 3 mm thick., A measurement of the transmission of two samples of window material is shown in figure 30. We have measured several samples of this material and have found the transmissions to be very reproducible. We have also been able to restore the original transmission after contaminating the surface of the material. We have measured the optical aberrations introduced by the surface finish of the windows, and find it makes a negligible contribution to the reconstruction errors.

The thickness of the material was chosen as a compromise between good transmission, mechanical strength, and an acceptable increase in the material shadowing the photon detector, to which the windows contribute

~ 2% of a radiation length. The windows are glued into the mechanical structure of the TPC making a rigid but low mass structure.

3c.4 The electrostatic field shaping

The TPC as described in section 3c.2 contains a drift volume, with MWPC at one end opposite a high potential plate. The sides of the drift volume are surrounded by field shaping wires at 2 mm spacing in an attempt to keep the equipotentials within the drift volume parallel to the MWPC cathode plane. This is most important for the region close to the entrance window. Early tests by Ypsilantis et al, later confirmed by our prototype tests (appendix 1) demonstrated that field shaping wires on one side of the dielectric do not produce the correct field shape in the drift volume. Placing field shaping wires on both sides of the dielectric overcomes this problem. We have confirmed this solution for an electrostatic model of the prototype using the PE2D⁽⁹⁾ computer program available in ICF at RAL.

3c.5 The drift gas.

Laboratory tests confirm that a field gradient of 0.5 kv/cm gives an acceptable drift velocity (6 cm/ μ sec) in gas mixtures containing methane (CH_4), iso-butane ($\text{C}_4 \text{H}_{10}$) and a photoionising agent (TMAE).

This drift velocity would give the detector a sensitive time of ~ 3 μ sec which, as we showed in section 3a, gives an acceptable performance up to the highest interaction rates available at Omega. Including isobutane in the gas mixture reduces the drift velocity, reduces the longitudinal and transverse diffusion of the drifting electrons, and helps to quench the gas amplification process in the MWPC. However Isobutane absorbs UV photons at a longer wavelength than the cutoff of the window, thus reducing N_0 (see fig 4 and 37). We have tested other gas mixtures, and have not decided which drift gas to use in the final detector, although it will perform very much like the methane/isobutane/TMAE mixture described but will maximise N_0 . Figures 31 and 32 give the drift velocities and diffusion characteristics for some common drift gases.⁽¹⁰⁾

It should be noted that a mixture of methane and TMAE gives a drift velocity of ~ 9 cms/ μ sec, and that diffusion in this gas contributes ~ 1 mm to the inaccuracy in finding the photon conversion point.

The vapour pressure of TMAE at 25°C is 1.0 torr which yields an absorption length for UV photons of ~ 10 mm in the TPC. The depth of the TPC was fixed at 5 cms to ensure complete absorption of the UV photons within the detector. It should be noted that with a 10 mm absorption length, and the largest angles encountered in the omega detector, the reconstruction errors are ~ 1 mm, which is well matched to the other errors.

To minimise the risk of TMAE condensing in the TPC, the TPC and drift gas transfer system must be operated at $\sim 30^\circ\text{C}$. So we will in practice run the whole detector at this temperature. The detector mounting system (fig 10) is a double skinned structure described in detail in section 3e.

3c.6 A summary of tests with a prototype TPC.

We have constructed a prototype TPC, 10 cms long, 10 cms wide and 4 cms deep, with a MWPC at one end as shown in figures 33 and 34. The MWPC has 48 gold plated tungsten sense wires, each 20 μ in diameter, and spaced at 2 mm intervals. A drift field of 0.5 kv/cm was shaped by 200 μ wires at 2 mm intervals surrounding the drift volume.

In the first series of tests a β source was used to ionise the drift gas ~ 6 cms from the MWPC. The ionisation from a single electron passing through the gas is drifted onto the MWPC. Each of the 48 wires stops a TDC and the data is read into CAMAC and written to magnetic tape for offline analysis. We are able to plateau the MWPC (amplifier sensitivity ~ 0.2 μA) and can reconstruct each track using the drift time and wire spacing information. A straight line fit to this data gives an RMS error of ± 0.7 mm. We could not detect any attenuation when the drift distance was changed from 4.5 cms to 7.5 cms.

For the second series of tests we added a photoionising vapour to the drift gas and have detected UV photons. A deuterium discharge source

and monochromator were used to provide UV photons of known wavelength. (For practical reasons we have used TEA (TRIETHYLAMINE) as the photoionising agent and CaF windows for these tests. This difference is immaterial as far as the results are concerned.) The counting rate on the MWPC wires was measured as a function of wavelength. The observed spectra followed the convolution of the deuterium spectrum and the response curve for the photoionising medium. The electrons from photon conversions were drifted over a distance of 6 cms, and the observed sensitivity of the TPC was twice that of a phototube coated with wavelength shifter.

3d Electronic Readout

3d.1 Introduction

The design of the electronic readout is based on sixteen TPC modules, each with 192 wires, giving 3072 wires in all. Each wire will be provided with a sensitive amplifier ($\sim 0.1 \mu\text{A}$) which will drive ECL balanced signals up twisted pair cable to a time slice encoder module (TSE). Data from the TPC will then be strobed into the TSE at a clock frequency equivalent to a 4 mm drift in the TPC. This clock frequency will be variable to compensate for changes in the drift velocity, but a typical period will be ~ 60 nsec.

The first system to be commissioned will provide a CAMAC readout of data encoded in the TSE. However in designing the system we have taken into account the option of using the detector in the longer term, as a second stage trigger of an experiment. This option will be installed after the detector has been used successfully for offline analysis.

3d.2 The Amplifiers

Many designs of amplifier are available for MWPC and drift chamber applications. The TPC requires an amplifier with a low input threshold to keep the MWPC gas gain to a minimum in order to maintain stable long term running conditions. Ypsilantis et al⁽³⁾ have used an amplifier with a sensitivity of $0.1 \mu\text{A}$ in successful tests of a TPC, while we have used

a modified Bristol University design with a sensitivity of $0.2 \mu\text{A}$. The amplifiers used in our tests amplified the signals from 48 MWPC sense wires, spaced at 2 mm intervals. Care was taken to avoid earth loops, and no problems with oscillations were encountered. The cross talk between adjacent channels was only apparent for signals 40 db above threshold. In reconstructing tracks in the TPC the RMS to the fitted track was $\sim 0.7 \text{ mm}$ which included any time slewing effects in the amplifiers.

3d.3 The time slice encoder

The major functions of the time slice encoder are shown in figure 35. Signals from the 192 amplifiers arrive on twisted pair cables, and are strobed into a 192×64 memory. Data from the amplifiers is continuously strobed into the input memory every clock cycle. About 500 nsec after an interaction has taken place, the first stage trigger logic sends a pulse to the TSE to flag an event of interest. After a further 42 clock cycles ($2.5 \mu\text{sec}$), all data from the event of interest has been strobed into the input buffer, and encoding starts. If at any time up to this point the event is abandoned, the encoding process can be inhibited, and no dead time is introduced.

The contents of each time slice are then encoded. A wire OR of the data in the first clock strobe is tested for the presence of data. If data is present, a number of priority encoders, each encode a section of the 192 bit memory in parallel. The encoded data is stored in 18 bits in an output memory, 6 bits are used for time information and 12 bits for the wire address.

Each TSE takes all the data from one TPC module. Eight TPCs are mounted above the median plane, and eight below. The electronics considers the chambers above and below the median plane to be one logical chamber which is read out in two halves.

The data for each TSE can be read into CAMAC for off line analysis, the readout time being a function of the quantity of data stored.

3d.4 Second stage trigger logic

In our design we are keeping open the possibility of using the data stored in the output memory of the TSE in ring finding logic which will enable the ring image detector to be used in a second stage trigger of an experiment. There are various ways in which the track vectors for particles emerging from Omega could be measured. Given these vectors a look up table could be used to determine P_i , P_{Ti} and C_i the momentum, transverse momentum, and ring centre for the i th track. A second look up table is then used with each value of P_i , to predict the ring radius and expected number of photoelectrons $N_{\alpha i}$ in each ring, where α is either an electron, pion, kaon, or proton.

Figure 36 shows the ring finding logic taking data from four TSE modules. A ring can overlap up to four modules, but knowledge of the ring centre selects a ring finding logic unit which will contain all digitisings for a particular ring. Ring finding logic units could work on the data in parallel, using the algorithms discussed in section 3a.

Plans for commissioning this readout system, and an estimate of the cost are given in section 4.

3e Radiator gases and mounting system.

The design as discussed in section 2 assumed that the radiator gas was Argon, and showed that chromatic dispersion when TMAE is used as a photoionising agent is the major contribution to the ring reconstruction error. In principle other radiator gases can be used provided they transmit in the wavelength region at which TMAE is sensitive. Figure 6 shows the refractive index of Argon, N_2 and Co_2 as a function of wavelength, and figure 37 shows the transmission of Co_2 together with other gases to be considered for the drift gas. Using Co_2 as an example of an alternative radiator gas, we would limit the TMAE bandwidth to 0.83 eV, as a result N_0 would fall to 61% of previous value. However the cerenkov angle would increase from 27 mrad to 33 mrad, and the expected number of photoelectrons remains the same. In reducing the bandwidth we

decrease the dispersion error to 1.2mm, and lower the threshold because the refractive index is higher. We detect pions at 4.5 GeV/c and should be able to separate pions from kaons up to 70 GeV/c. The decreased dispersion error will extend the range, but in practice at the highest momenta the resolution is likely to be determined by systematic effects; for example mirror alignment.

If the TPC is to use TMAE at 25°C, then the TPC and the rest of the detector should be maintained at ~ 30°C to prevent condensation of the TMAE, to keep the refractive index of the radiator constant, and to prevent thermal effects in the mirror system. The radiator gas should be kept free from oxygen to the level of 5 parts per million, and this led to the double skin design for the detector shown in fig 10. All of the massive structural members of the detector will be kept out of the acceptance of the photon detector. The design has two main structural members, one to support the TPC array, the other to support the mirror array. These two structures are kept a fixed distance apart. The inner skin contains the radiator gas, the TPCs are at one end and the mirrors at the other. The outer skin is both gas tight and a good heat insulator. Between the two skins a heated gas is circulated to keep the main detector at constant temperature. This gas will be the same as the radiator gas, thus providing an added buffer against gas leaks. The refractive index of the radiator will be measured by a refractometer and monitored by a number of gas dielectric capacitors distributed throughout the gas volume. The temperature of the whole enclosure will be monitored and kept constant to $\pm 1^\circ\text{C}$. The design of this part of the detector has been completed for costing purposes. Detailed design will proceed on approval of the project.

4. TIMESCALES AND COST

4a Construction and Commissioning timescales

The development work on Ring image cerenkov detectors started in 1978 in collaboration with Bristol University⁽¹¹⁾, and continued at a low level until September 1981 when more members of the Omega photon group became involved. Since that time the group has commissioned and tested a TPC using both particles, and UV photons, and made a systematic study of the properties of window materials and gases in the far UV. We have measured mirror reflectivities at the National Physical Laboratory (NPL) and have developed techniques for mirror manufacture. If this proposal is approved this work will be continued by testing the TPC prototype in test beams at CERN, and in continuing the development of a full size prototype to be tested at RAL in May. The first production model will be tested with a beam in the summer, and production of the full set of TPC modules is planned to start in September. A prototype radiator vessel will be constructed at RAL in May and tested in the beam at CERN in late summer. This vessel will be used with the first of the production mirrors which we expect to be available by then. We plan to test each TPC in the test beam before it is assembled in the final detector in the West area.

The final detector vessel will be assembled in a West area test beam line as soon as the upgrade allows. Mirrors will be set up in this vessel during the spring of 1983, and TPC modules mounted in position after test at the PS. Tests of the complete detector will start as soon as test beams are available in the West area, after May 1983.

The first prototype modules of the electronic readout will be available in September to be tested with the full size TPC prototype. The stage I readout system will be completed by March 1983, Stage II following close behind.

A bar chart summarising the mechanical construction programme is given in fig 36. Three items appear on the critical path. The first is the manufacture of quartz windows which has a wait time of three months. A "tender action" has been started to reduce any delay to the programme.

The mirror mould used to preform the mirrors may take some time to manufacture and work to reduce this delay is in hand. The third item on the critical path is the ordering of components for the electronic readout. This is awaiting approval.

If the project is approved in April 1982, a large fraction of the detector will be ready for testing in the West area at CERN as soon as beams are available after the upgrade. The outstanding items will be the last of the TPC modules, and the second stage of the electronic readout. Both of these items are not required immediately and the detector commissioning can continue without them. We plan to install the detector behind Omega late in 1983 having first thoroughly commissioned it in a test beam. This is consistent with the present plans for utilising Omega after the shutdown.

4b Cost and Manpower Estimates

The development programme has evaluated many of the problems associated with the construction of a ring image detector for Omega. We have used this information in arriving at the estimated cost of the project.

Mechanical Items

(1) Mirror System	£25K	
(2) 18 TPC Modules without quartz windows	£25K	
(3) 36 Quartz windows	£65K	
(4) Mounting structure, window support, radiator vessel and monitoring system	<u>£60K</u>	
	£175K	£175K

Electronic readout (3200 wires)

Stage I (Camac readout)

Amplifiers	£64K
Time Slice Encoders	£32K
Cables	£15K
Racks	<u>£6K</u>
	£117K

Stage II (Second stage trigger)

Ring finding logic	£17K	
Centre finding logic	<u>£16K</u>	
	£33K	<u>£150K</u>
		£325K

We have been advised by the Physics apparatus group (PAG) and the electronics group in arriving at the manpower requirements summarised below in Man years.

	1982/83	1983/84
<u>PAG</u>		
Design and Development	2	-
Manufacture and Testing	4	0.5
Installation	1	1
<u>Electronics Group</u>		
Design and Development	4	2
Manufacture and testing	5	5
Installation	-	3

5 SUMMARY OF PROPOSAL

A ring image detector has been designed for use with Omega in the upgraded West area at the CERN SPS. This detector is placed downstream of Omega, and is designed to accept all particles emerging from the Omega magnet. The position of the detector has been optimised to match the optics of the mirror system to the particle trajectories in the Omega magnetic field, thus reducing optical errors to negligible level. A 5 metre Argon gas radiator is used in conjunction with a good quality mirror system, of focal length 5 metres, to focus cerenkov light from a particle (with $\beta = 1$) to a 13 cm radius ring image. A two dimensional readout of this ring image will be obtained by using a TPC, making use of the photoionising agent TMAE in the drift gas. Using Argon as a radiator gas, pions can be identified above 5 GeV/c, and can be resolved from kaons up to 80 GeV/c. The detector has good spacial resolution and can efficiently identify two tracks separated by only a few millimetres in space.

The electronic readout will encode the data which will be read-out into CAMAC for subsequent off line analysis. As a second stage of development the detector could be used in the second stage trigger of an experiment, providing particle identification in $< 100 \mu\text{sec}$.

Monte Carlo studies show that the detector has a high efficiency for identifying tracks in high multiplicity events, even when the background from unwanted events is high. We are now convinced that the ring image detector is a viable proposition for use with Omega on a timescale compatible with that for the West area upgrade. The proposed detector will produce ring images containing up to 30 photoelectrons, and hence will be capable of being used for physics processes producing high charged particle multiplicities. In addition it will be capable of identifying individual particles in an interaction with much finer granularity than has been possible with conventional threshold cerenkov detectors.

The development work carried out at RAL over the past 6 months has convinced this collaboration that such a detector can be built using the resources of RAL.

Development work at RAL

Appendices 1, 2 and 3 summarise the development work carried out at RAL during the past six months. This work has involved the following members of HEP, Instrumentation and Technology divisions, together with Sheffield University.

M Atkinson
M Cawthraw
S Danaher
M Davenport
R Deol
P Flower
D Giddings
G Hallewell
A Ikades
R McClatchey
G McPherson
J A G Morris
J V Morris
P Sharp
B Thompson
C Uden

Appendix 1

TPC development work at RAL.

A1.1 Introduction

In this section we report on the work carried out at RAL in developing a TPC for use with the Omega ring image cerenkov detector. We have used a prototype TPC (figures 32 and 33) to detect and digitise the ionisation produced by an electron from a β source passing through the drift volume. When a particle traverses the drift volume parallel to the MWPC plane but perpendicular to the direction of the MWPC sense wires, the ionisation from each 2 mm element of the track length drifts on to a separate sense wire. The arrival time of the ionisation is recorded on a TDC for each of the sense wires in the MWPC. We are able to efficiently detect the ionisation and obtain good straight line fits to the arrival time for the central 31 wires. We do not detect any attenuation in changing the drift distance from 4.5 cms to 7.5 cms. When particles traverse the drift volume parallel to the MWPC plane and parallel to the MWPC sense wires we obtain two equivalent (wire map, and time distribution) projections of the ionisation left in the chamber. When the source is moved parallel to the MWPC plane, we detect a corresponding change in the MWPC wire address. We conclude that an accurate two dimensional reconstruction can be made of ionisation produced within the drift volume of the TPC.

We have used the TPC to detect UV photons. These pass into the TPC through two calcium fluoride windows and photoionise a small quantity of triethylamine (TEA) added to the drift gas. We measure the response of the TPC as a function of wave length and compare this to the response of a photomultiplier coated with wavelength shifter. The shape of the function required to transform the TPC data to the photomultiplier data is that of the measured quantum efficiency of TEA, and we observe that the sensitivity of the TPC is approximately twice that of the photomultiplier. When a narrow collimator is scanned across the UV photon beam, a corresponding displacement is observed in the TPC.


We conclude that we can detect electrons from single photoionisation events within the TPC drift volume, and can accurately reconstruct these events in two dimensions. In the absence of a high energy charged particle beam we cannot efficiently demonstrate cerenkov ring images at RAL. Plans are in hand for the use of a test beam at CERN.

A1.2 Description of TPC

A side elevation of the TPC is shown in figure 33 and a plan view in figure 34. The dimensions of the drift volume are 10 cm long, by 10 cm wide by 4 cm deep. At one end of the drift volume is a 48 wire MWPC with 2 mm wire spacing, and 5 mm anode-cathode spacing. The MWPC cathode is at earth potential, while at the opposite end of the drift volume is a conducting plate at high negative potential. The electric drift field can be varied, a typical value being 0.5 KV/cm. The volume between the MWPC and the high potential plate is surrounded by two layers of field shaping wires, at 2 mm intervals, on either side of a dielectric box. The two large area sides of the dielectric box are fitted with UV transmitting windows, one being a 7.5 cm diameter, 3 mm thick CaF₂ window (to allow tests with TEA as the photoionising gas) the other being a 6.5 cm diameter, 3 mm fused silica window. The transmission of these windows is discussed in Appendix 3. The voltage on each of the field shaping wires is determined by a linear resistor chain. A large value resistor is inserted between the last field shaping wire and earth, so that the drift voltage and the MWPC voltage can be independently adjusted. The value of this resistor is changed for each value of drift field.

This layout of field shaping wires is the result of a number of developments in field shaping geometry and is identical to the layout proposed for the TPC to be used in the Omega detector. The sides of the dielectric box have slots cut in the fibre glass walls which allow electrons from a β source to traverse the drift volume.

The drift volume is itself enclosed in a fibreglass housing which contains the drift gas, and through which all electrical connections pass. The

chamber is constructed on a stainless steel flange which can be mounted either onto the monochromator, or a cerenkov radiator vessel. A 7 cm diameter hole in this flange allows photons to enter the TPC through a re-entrant CaF_2 window close to the drift volume (fig 33). Great care was taken to minimise the thickness of gas between the inside edge of the first CaF_2 window, and the inside edge of the second CaF_2 window, as photons converted in this region cannot be collected by the MWPC. The first CaF_2 window isolates the radiator gas from the photoionising drift gas, while the second CaF_2 window has field shaping wires on both sides to produce an electric field in the drift volume perpendicular to its surface. We have constructed an electrostatic model of this geometry using the PE2D program available on the ICF at RAL. This program calculates the equipotential contours for a two dimensional model of the chamber. A diagram of these equipotentials is shown in figure 39. Deviation of the equipotentials from the normal to the window surface is due to the stainless steel window support (the  structure in figure 34, which allows us to evacuate the volume outside the detector). This support is at earth potential, and distorts the field in the drift region. The two dimensional nature of the model makes a pessimistic prediction for the electric field shape. The Omega detector will not have any conductors at earth potential close to the window surface.

Each sense wire of the MWPC is connected by a 30 cm coaxial cable to a sensitive amplifier, which in turn is connected to a TDC by twisted pair cable, and an ECL to NIM convertor. The amplifiers were designed at Bristol University, but have been recently modified to improve the threshold sensitivity by a factor of ten. The present threshold is $< 0.2 \mu\text{A}$, and no crosstalk is experienced provided the signal on an adjacent channel is less 40 db above threshold. Great care was taken to ensure good earthing of the system, and no problems with oscillations have been experienced. This is an important test for the Omega detector as it represents a quarter of the wires required for one TPC, at twice the packing density.

Before mounting the MWPC on the drift volume the chamber and the electronics were thoroughly tested with a source. EHT plateaus were established for a number of gas mixtures, and transit time variations in the chamber and readout system were evaluated.

A1.3 Tests with a β source

Electrons from a β source traverse the drift volume parallel to the MWPC plane, but perpendicular to the MWPC sense wires (left to right in fig 34). The TPC is placed between the β source (Ru^{106}) and a one centimetre diameter scintillator viewed by two photomultipliers, and the coincidence output from these is used to start the TDCs. A laser is used to align the assembly so that the average drift distance of ionisation produced by the electrons is 6 cms and constant across the chamber. On passing through the drift volume the electron ionises the gas, and electrons from this process drift in an electric field of ~ 0.5 KV/cm towards the MWPC sense plane. A gas amplification of $\sim 10^4$ at each sense wire produces a signal which is further amplified and used to stop a TDC. The contents of the 48 TDCs are readout into a PDP 11/24 after each event. The data is analysed online, and also written to magnetic tape for offline analysis. We present here a summary of data taken during the past three months. In all ~ 50 tapes of data have been analysed by offline programs which have been used, together with the data available from the online analysis, to understand the behaviour of the TPC.

A typical (not selected) track is shown in figure 40. The TDC outputs are plotted for wires 10 to 40. The outer wires are close to the dielectric box and are not used in the offline analysis. Of the 30 wires, 24 have drift times which correspond to a straight line, while 6 have times which occur later than that expected for a straight line. In the offline analysis we first fit a straight line through all the observed points, and calculate the RMS deviation of the points about the line. If this RMS is greater than 25 nsec, in subsequent iterations the point with the maximum deviation is omitted. When the RMS is less than 25 ns any point with a residual more than 3 times the RMS is rejected. This process removed the 6 points which lay off the track shown in fig 40. The first five points were removed because $\text{RMS} > 25$ ns, and the sixth point because its residual was > 3 times the RMS. The resulting RMS to the fitted track is 0.7 mm. On average this process removes 4 points for each event when the MWPC EHT is well onto the plateau. This event was taken with $\text{CH}_4(70\%)\text{C}_4\text{H}_{10}(30\%)$ drift gas which produced a 500 volt plateau for most wires from 4.5 Kv to 5.0 Kv.

Figure 41 shows a plot of residuals for both accepted and rejected points. It is clear that very few rejected points should have been included in the fit, and also that most rejected points occur in a peak 140 nsec after we would have expected a signal from the ionisation. We believe that we are not observing any prompt ionisation arriving at these sense wires, but only a late signal produced by the interaction of a photon emitted by the gas amplification process at an adjacent wire. About 3% of triggers have no data in the TDC's. The remaining triggers have > 20 wires with data, and the probability of any wire not having data is the same for all wires. We have repeated this analysis with similar results for a number of potential drift chamber gases, being mixtures of Argon, Methane, Isobutane and TEA. Isobutane can be used, with TMAE as a photoionising agent, but it absorbs UV at $\sim 1700\text{\AA}$ (see fig 37) so cannot be used with TEA. Most of our tests have been made with CH_4 , and mixtures of CH_4 and TEA.

Using Poisson statistics the probability of not observing a signal, when the mean number of detectable electrons is N , is $P(0) = e^{-N}$, from which the efficiency of a wire is $\eta = 1 - P(0) = 1 - e^{-N}$. By measuring the individual wire efficiencies we can estimate the mean number of ionising events in a 2 mm element of the ionising track. A plot of the mean number N , calculated in this way, is shown in fig 42 for CH_4 and fig 43 for CH_4 (99%) TEA (1%). The offline analysis removes hits which lie off the track, and in the case of CH_4 the mean number drops to 1.66, which is in good agreement with the observation of Ypsilantis et al⁽³⁾ of 1.73/2 mm of track. Introducing TEA into the gas converts photons from the gas amplification process close to the sense wires, as a result of which it is more difficult to separate point ionisation from effects induced by photons. The drift velocity observed for each of the gases was in good agreement with those observed by Ypsilantis et al⁽³⁾.

In changing the drift distance from 4.5 cms to 7.5 cms we observe no attenuation in the number of electrons per sense wire.

Before the UV transmitting windows were installed a number of tests were performed with electrons from the β source traversing the drift volume parallel to the MWPC plane and parallel to the MWPC sense wires. (Left to right in fig 33). In this configuration an electron traverses 4 cms of drift chamber gas and all the ionisation is collected by one MWPC wire. However we can compare the beam profiles of the source in two dimensions, one from the MWPC wire map, the other from the time distribution for the struck wires, and the two distributions are the same. Also moving the source in other directions produced equivalent changes in either the wire map (fig 44) or time distribution.

From our work with the β source we believe that the TPC gives an accurate two dimensional reconstruction of ionisation left in the drift volume. We have been able to make straight line fits to tracks, which give RMS errors from the fitted line = 0.7 mm, compared to an accuracy of ~ 1 mm required for the Omega detector.

A1.3 Tests with a UV Source

The TPC was mounted on a monochromator, in place of the photomultiplier, as shown in figure 45. A deuterium source was used to provide a continuous (no time structure) source of UV photons which were wavelength selected by the monochromator. The same arrangement, using a photomultiplier coated with wavelength shifter, was used to measure the transmission of window materials and gases as described in Appendix 3. The UV photons enter the TPC through two CaF_2 windows and photoionise Triethylamine (TEA) in the drift gas. The electrons produced by the photoionisation drift ~ 6 cms to the MWPC sense plans. The UV beam is ~ 1 cm wide, and signals are detected on five of the MWPC sense plane wires. These signals are scaled as a function of monochromator wavelength, and are shown in figure 46.

The corresponding response curve, taken with the photomultiplier coated with wavelength shifter, is shown in figure 47. In figure 48 we compare the shape of the function require to transform figure 46 to figure 47. We note that it is exactly the same shape as the wavelength response of TEA

measured by Ypsilantis et al. We repeat the same wavelength scan using CH_4 without TEA, shown in fig 46, and conclude that we observe photoionisation for TEA and that we detect single electrons from the photoionisation process. We place a 1 mm wide collimator in the UV photon beam and observe that a movement of the collimator produces a linear displacement of the detected signal at the MWPC plane, as shown in fig 49. The peaked intensity distribution of the UV beam reduces the slope of the straight line from the expected value of 1.0. Because the deuterium source produces photons continuously we are unable to investigate the spacial resolution in the time direction. However, we have already measured this well with tracks from the β source.

A comparison of the sensitivity of the TPC with that of the photomultiplier is difficult because of the different geometries. The raw counting rates indicate a factor of 8 in favour of the TPC, but after correcting for losses in windows and trapped volumes of gas in the case of the photomultiplier, we conclude that the TPC is at least twice as sensitive as the photomultiplier.

Al.5 Conclusions

We have tested a prototype TPC with ionisation produced by electrons from a β source, and with UV photons. We are able to detect single electrons from the photoionisation of TEA, after drifting the electrons a distance of 6 cms. We traverse a collimator across the UV photon beam and see the signal on a corresponding wire in the MWPC. It is difficult to compare the sensitivity of the TPC with that of a photomultiplier coated with wavelength shifter, but we believe the TPC to be as twice as sensitive. We have used the ionisation produced by a low energy electron traversing the drift volume to measure the time resolution of the detector. When the MWPC is plateaued more than 80% of the wires have good data in each event. The remaining ($\sim 20\%$) wires have late signals, which correspond to a secondary process, implying that no ionising events occurred in that 2 mm element of the track. A fit to tracks gives an RMS error = 0.7 mm, and the mean number of electrons observed agrees with that observed by Ypsilantis⁽³⁾ in a TPC in which has been used to obtain cerenkov ring images. The performance of this prototype TPC is better than that required for the Omega detector.

Appendix 2. The mirror development programme

In section 2 and section 3 of the proposal we discussed the design of the mirror system for the Omega detector. We specify 81 hexagonal mirrors each 70 cms point to point. Each mirror should have good reflectivity in the far UV, ie $>70\%$ at 1600\AA , and the deviations produced from such a mirror should be less than 1 mm on the focal surface. To evaluate the problems in obtaining 81 such mirrors we decided to make a number of prototypes, and to use them to test each of the processes involved in the manufacture of the final mirror system. The radius of curvature of the final mirror is 10 meters, but we were unable to obtain a mould to preform mirrors of this radius of curvature. However, in collaboration with members of the Muratori group at CERN we obtained 15 preformed mirror blanks, each of 3.4 m radius of curvature. A technician from the physics apparatus group worked with CERN personnel in making the mirrors in order to evaluate any problems, and the first sample blanks received at RAL were used to evaluate both the mirror grinding and coating processes. One blank was taken to AE Optical Company in Luton where it has been ground to an acceptable finish. A second blank was cut to a hexagonal shape, of the correct size, and coated by K Fletcher at Culham Laboratory. We expand on our experience with both of these processes in later sections. We have used reflectometers at the National Physical Laboratory (NPL) to measure the reflectivity of mirrors produced at Culham. Although the reflectivities are acceptable, the possibilities for improvement are being investigated.

A2.2 Preforming mirror blanks

Float or plate glass is preformed by pulling the glass onto a former of the required radius of curvature at 560°C . The former is a cast stainless steel mould (~ 1 m diameter) which is machined and ground to the correct radius of curvature. This mould is then placed in a large oven, and connected to a vacuum supply. The glass plate, 3 or 4 mm thick is placed over the mould and heated. It is then pulled down into the mould with

the vacuum system. The oven is allowed to cool down over the next 12 hours, leaving the glass in a well annealed state.

Optical tests on a typical blank produced by this process indicate that the mirror is not yet of the required standard. The image of a point source placed to one side of the centre of curvature produces an image ~ 20 mm diameter. This image can be reduced to ~ 1 mm by grinding the mirror surface.

A2.3 Mirror grinding

A mirror made of 3 mm thick glass is too flexible to grind unsupported. A 5 cm thick duralumin disc 80 cms in diameter was machined to produce a concave surface of 3.4 metres radius of curvature. The preformed mirror blank rests on an elastic medium on the duralumin disc, and the mirror is then ground until the image of a point source is less than 1 mm.

The first mirror to be ground was a very bad example of the preformed type, and has been used to optimise the techniques involved. The experts at AE Optics estimate that production mirrors will take one day to grind and up to three days to polish. They recommend that four grinding machines are in use at any time, producing one completed mirror a day. This time scale is well matched to the preforming timescale of one mirror a day, and the coating timescale of two mirrors per day. The first mirror has been ground and polished and the image of a point source is < 1 mm. Measurements of mirror distortion beyond this level depend strongly on the mounting system involved.

A2.4 Mirror Coating

Glass blanks up to 70 cms diameter can be coated in a plant at Culham Laboratory, to produce mirrors with good reflectivity into the far UV. The circular ground and polished glass blank is cut to a hexagonal shape, and a 50 cm diameter stainless steel ring is glued to the back surface. This ring is used to support the mirror during coating and to mount the mirror in the Omega detector.

For coating, the mirror is rotated at 60 rpm in the horizontal plane ~50cm above two electrically powered evaporator boats. The whole system is evacuated to 10^{-6} torr before coating begins. An aluminium coat is rapidly evaporated onto the surface of the glass. The thickness of the coat is monitored during evaporation. When the reflectivity reaches a maximum the aluminium evaporation is stopped, and MgF_2 is evaporated onto the surface before any deterioration takes place. The thickness of MgF_2 is controlled to optimise reflectivity.

A2.5 Reflectivity Measurements

We have used a vacuum reflectometer at NPL to measure the reflectivity of the mirrors produced at Culham, and we are working closely with K Fletcher to optimise reflectivity while minimising variation across the mirror. Thus far we have measured reflectivities of > 70% at wavelengths above 1600Å. We believe it is possible to obtain values of ~ 80%, and will continue to improve the techniques. The measured reflectivity for one sample is shown in fig. 50, and the variation in reflectivity across the surface of the mirror is ~ 5%.

A2.6 Conclusions

We are processing a number of mirror blanks through all steps of the manufacturing process. We have obtained preformed blanks of 3.4 m radius of curvature, which have been successfully ground and polished. We have coated a mirror blank, and measurements of reflectivity suggest that the coating process is better than the required specification, but that small improvements may be possible. The estimates of costs included in section 4 have been made in the light of the experience gained in this development programme, and we are confident that many of the problems involved in making the mirror system are understood.

Appendix 3 UV Measurements

A3.1 UV measurement system

The system developed for UV transmission measurements is shown in figure 45. The UV light source was a deuterium arc-lamp with a plane MgF_2 window^{12,13}. Photons of a particular wavelength were selected by a 1 m normal incidence vacuum monochromator¹⁴, operating at 2×10^{-5} Torr, which contained a 1200 groove/mm concave grating. The diverging beam emerging from the monochromator exit slit was passed through a bi-convex MgF_2 lens ($f = 10$ cm at 2000\AA) in order to reduce the beam size at the photon detector.

In between the monochromator and photon detector was an independent vacuum system, consisting of a 2 m long cylindrical vessel (VI) coupled to a Sample Test Vessel (STV). This composite vessel was connected to a vacuum pump and the beam entrance and exit flanges were sealed by MgF_2 windows (3 mm thick, 50 mm diameter). The vessel could be filled with gas using admittance valves on both end flanges.

The Sample Test Vessel was instrumented with three manipulator rods, each connected to a sample holder. Each rod could be moved laterally across the beam or rotated about its axis in order to swing the sample in and out of the beam. For normal running conditions, one sample holder was fitted with a 19 mm diameter beam collimator, leaving the other two holders available for samples. The UV photons emerging from the vacuum vessel were detected by a photomultiplier tube (EMI 9183 KB) coated with a wavelength shifter (p-terphenol¹⁵). The tube was operated at positive HT (2.4 kV) in order to prevent corona discharge developing between photocathode and vacuum flange.

Originally it was intended that the rim of the photomultiplier window would act as the vacuum seal at the exit flange, however it was reported¹⁶ that window coatings tended to evaporate away after prolonged exposure to vacuum. As a precaution the tube was positioned immediately behind a

MgF₂ window, on a 0.14 mm thick PTFE spacer-ring, which prevented any pressure loading on the centre of the window. Note that the 0.14 mm air gap transmitted ~ 33% of beam photons at 1450Å (the peak of the O₂ absorption band).

The electronic logic for the photomultiplier tube is shown in figure 51. The signal was amplified by a factor of 10 and then discriminated (threshold 150 mV). The discriminator outputs fed a frequency meter and a scaler/ratemeter/pen recorder unit. Photomultiplier tube pulse height spectra are shown in figure 52 for the following cases:

- (i) tube spectrum lamp on.
- (ii) tube spectrum above discriminator threshold.

Typical noise rates were 60 Hz whilst typical signal rates varied between 10 kHz and 1 MHz.

A scan across the emission spectrum of the lamps, recorded by the pen recorder, is shown in figure 47. The monochromator was initially calibrated using spectral lines from a low pressure Hg discharge lamp, the deuterium resonance line at 1215Å provided a check of the calibration, and a scan across this line is shown in figure 47. The wavelength calibration was found to be correct to within 1Å.

A3.2 UV transmission of window materials

The work to date has concentrated on the following areas:

- (i) Measurements on samples of quartz in order to evaluate their suitability for use in the omega detector.
- (ii) Measurements of CaF₂ windows used in the prototype TPC.
- (iii) Investigations of the effects of surface treatments on the transmission of CaF₂, and of surface contamination on the transmission of quartz.

The technique used in all transmission measurements was to mount the sample in a holder and ensure that the sample was vertical when the holder was locked into the 'IN' position. The measurements were taken when the pressure was below 10^{-4} torr in the vacuum vessel. [Note that at higher pressures, photons from the glow discharge in the Penning gauge were detected by the photomultiplier tube.] The transmission was defined as the ratio of the photomultiplier tube rate for sample IN/OUT. A background subtraction was made to both IN and OUT rates in order to remove PM tube noise and background light escaping from monochromator. This correction was ~ 200 Hz. It was found that measurements were reproducible to the level of 1%.

The results for samples of Quartz manufactured by HERAEUS⁽¹⁷⁾ are shown in figure 30.

The CaF_2 window used in the prototype TPC was measured in isolation and after wrapping with drift field wires (200 μm diameter, 2 mm pitch). The transmission curves are shown in figure 53. Note that a uniform 20% decrease in transmission resulted from the area obscured by the addition of the field wires.

Surface contaminations of the quartz window samples and their effect on transmission are being investigated. Firstly with the long term view of specifying the degree of cleanliness required during the handling of the large windows used in a full scale detector. As an example of the effect of finger prints on the surface of quartz, figure 54 shows a comparison of the transmission curve of a quartz sample before and after being liberally finger marked.

Secondly, the transmission of CaF_2 has been studied as a function of the surface treatment. A cleaning method recommended for MgF_2 windows¹³ was found to improve transmission significantly in the region around 1500\AA . A comparison of the transmission of a sample of CaF_2 before and after a single then a double treatment is shown in figure 53. Further work will

be needed to study if any deterioration of transmission with time is observed in cleaned samples.

A3.3 Gas transmission measurements

This section of work is ready to start now that equipment has been assembled. This consists of a rare-gas purifier, in order to remove O_2 contamination in Argon, an O_2 impurity meter and a water vapour meter. The intention is to evacuate the vacuum vessel, and fill with gases at various pressures. Accurate measurements with this system require a stable UV source or a monitor of the intensity. Work is in progress to find the most stable condition at which to operate the lamp and to measure any remaining time dependence. At present it is believed that lamp intensity can be estimated to within $\pm 2\%$ in the first 3 hrs of operation after an initial 30 min warm-up period. This 3 hr period is long enough to complete measurements on a given gas sample.

Argon is known to be free from absorption bands over the wavelength interval appropriate to quartz windows, and TMAE as photoionising gas. When measurements on other gases have been completed it may be possible to consider the use of other radiator gases, for example, CO_2 .

A3.4 Conclusions

We have developed a reliable system for measuring transmissions into the Vacuum UV. We have obtained reproducible measurements of window transmission which we have used to select window material for the Omega detector TPC modules. A method of measuring the transmission of gases is being developed, and will be used to evaluate the possible radiator gases, and in defining the specification for the radiator containment vessel.

References

1. Proposal 231 Papers

- (a) meeting 28 PPESP/80/14 Memorandum
- (b) meeting 32 PPESP/80/42 Proposal 231 and addendum 1
- (c) meeting 33 PPESP/81/3 Addendum 2 (QCD processes)
- (d) meeting 35 PPESP/81/20 Addendum 3 (showing comparison of various stages of particle identification)

2. J Seguinot and T Ypsilantis, Nucl. Instrum. Methods 142 (1977) 377.

3. E Barrelet, T Ekelof, B Lund-Jensen, J Seguinot, J Tocqueville, M Urban and T Ypsilantis CERN EP/82-09

Other useful papers on ring imaging are:

(a) T Ekelof, J Seguinot, J Tocqueville and T Ypsilantis, Physica Scripta 23 (1981) 718.

(b) G Charpak and F Sauli, Phys. Lett. 78B (1978) 523.

(c) J Seguinot, J Tocqueville and T Ypsilantis, Nucl. Instrum. Methods 173 (1980) 283.

4. J Friedman SLAC CGTM/145 1972.

5. D Aston et al NP B166 (1980) 1-24.

6. B Adeva et al PL 102B (1981) 235.

7. J C Lasalle, F Carena, S Pensotti NIM 176 (1980).

8. T Ypsilantis, Physica Scripta 23 (1981) 370.

9. PE2D User Guide, Biddlecombe et al RAL/81/089

10. V Palladino and B Sadoulet, Nucl. Instrum. Methods 128 (1975) 323.

11. R Gilmore et al NIM 157 (1978) 507

12. Cathodeon Ltd., Cambridge

13. P J Key and R C Preston, J. Phys.E: Sci Instrum; Vol 13, 1980.

14. Model 310 NIV Vacuum Monochromator, Minuteman Laboratories Inc.

15. Baillon et al NIM 126 (1975) 13-23.

16. J Malos private communication

17. Heraeus Fused Quartz Products Ltd., Surrey

Figure Captions

- Fig 1 WA69 experimental layout: (a) as proposed (P231)
(b) with Ring Image Cerenkov
- Fig 2 Ring Image formation by a lens
- Fig 3 Schematic ring image Cerenkov detector
- Fig 4 Transmission, reflectivity and quantum efficiency of detector components
- Fig 5 Radius and number of detected photoelectrons as a function of particle momentum
- Fig 6 Refractive index of radiator gasses as a function of wavelength
- Fig 7 (a) Monte-Carlo ring image showing chromatic dispersion
(b) Distribution of radial distance from centre of ring
- Fig 8 Fitted radii for 80 GeV/c particles with chromatic dispersion
- Fig 9 Schematic view of a simple Time Projection Chamber
- Fig 10 Perspective view of the complete Ring Image detector, showing hexagonal mirror system and TPC modules
- Fig 11 Plan and side elevation of proposed experiment layout
- Fig 12 Plan and front elevation of one TPC module
- Fig 13 Schematic view of full size TPC module
- Fig 14 Charged particles from a high multiplicity Monte-Carlo event
- Fig 15 Monte-Carlo ring images for a high multiplicity event (see Fig 14)
- Fig 16 Charged particles from a charm event ($D^0\bar{D}^0$ + others)
- Fig 17 Monte-Carlo ring images for a charm event (see Fig 16)
- Fig 18 Ring Image identification flow chart
- Fig 19 Radial distance to all hits from predicted ring centre of a 20 GeV/c π in a Monte-Carlo high multiplicity event. Solid line is expected mean hits as a function of radius
- Fig 20 Radial distance to all hits from predicted ring centre of a 20 GeV/c K in a Monte-Carlo high multiplicity event (the same event as Fig 19)
- Fig 21 An example of the level of background in the Ring Image Detector for a high intensity hadron beam experiment (Monte-Carlo)

- Fig 22 Identification efficiency for pions and kaons from high multiplicity Monte-Carlo events as a function of background rate, using a simple ring-finding algorithm
- Fig 23 Ray diagram for mirror system with axial and off axis (non-zero impact parameter) tracks
- Fig 24 Eccentricity (e) and defocussing ($\Delta \theta/\theta$) of ring image as a function of impact parameter (b). Note that b/R_m is the angle between the normal to the mirror surface and the track direction
- Fig 25 Geometric acceptance of the Ring Image detector as a function of P_T/P
- Fig 26 Displacement vectors on the surface of an hexagonal mirror when mounted. (Finite element calculation)
- Fig 27 Deflection of mirror surface, for different mirror thicknesses, as a function of position on the surface (finite element calculation)
- Fig 28 Schematic view of an MWPC module
- Fig 29 Equipotentials surrounding one MWPC sense wire (computer calculation)
- Fig 30 Measured transmission of TPC window material, as a function of wavelength
- Fig 31 Drift velocity as a function of field strength for various possible drift gases
- Fig 32 Diffusion as a function of field strength for various possible drift gases
- Fig 33 Front elevation of prototype TPC
- Fig 34 Side elevation of prototype TPC
- Fig 35 Electronic read-out and ring finding logic
- Fig 36 Time slice encoder layout including ring finding logic for second stage trigger
- Fig 37 Transmission of some possible drift gases compared to quartz
- Fig 38 (a) Programme for Ring Image Cerenkov counter construction (summary)
 (b) Programme for RIC construction (details)
 (c) " "
 (d) " "
- Fig 39 Predicted equipotential distribution for the window half of prototype TPC obtained from a computer simulation
- Fig 40 Arrival time distribution for ionisation caused by the passage of electrons from β source through drift gas, approximate drift distance is 6cms, residual to straight line fit is $\pm 0.6\text{mm}$

- Fig 41 Residual distribution after straight line fit to arrival time distribution. Points above track in fig 40 contribute to peak at ~ 140
- Fig 42 Mean number of electrons detected wire by wire for CH_4 drift gas
- Fig 43 Mean number of detected electrons for $\text{CH}_4 + 1\%$ TEA drift gas
- Fig 44 Wire # as function of source displacement parallel to MWPC plane
- Fig 45 Layout of the UV transmission measurement system
- Fig 46 Count rate observed on MWPC Sense wires in UV photon beam as function of photon wavelength
- Fig 47 Deuterium lamp spectrum observed with photomultiplier coated with wavelength shifter. The 1215 \AA Deuterium line is used to check wavelength calibration
- Fig 48 Ratio of TPC spectrum to Photomultiplier spectrum compared to relative quantum efficiency measured by Ypsilantis et al
- Fig 49 Change in wire address as a function of collimator position in photon beam
- Fig 50 Measured reflectivity of large sample mirror compared to reflectivity of a small sample mirror
- Fig 51 Layout of logic used with photomultiplier to observe UV photons
- Fig 52 Pulse height spectrum for photomultiplier before and after discriminator
- Fig 53 Transmission for CaF_2 as a function of wavelength for different surface preparations
- Fig 54 Transmission of quartz with surface contamination and after cleaning

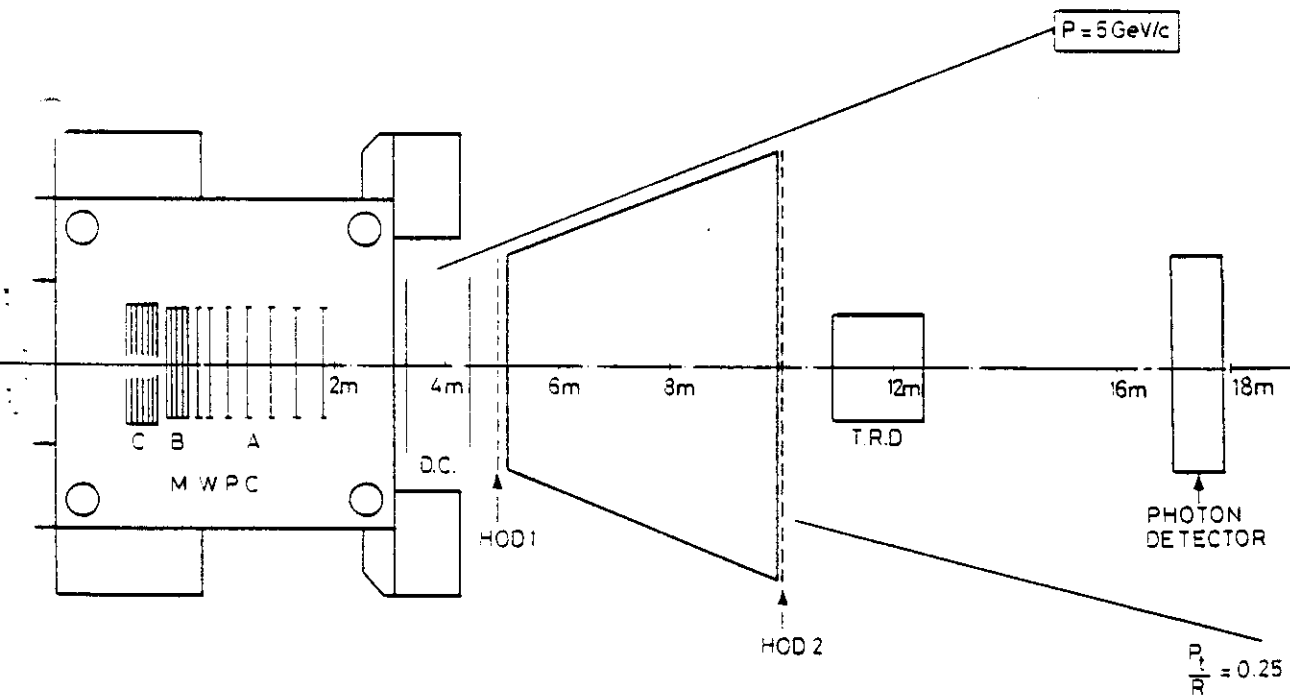
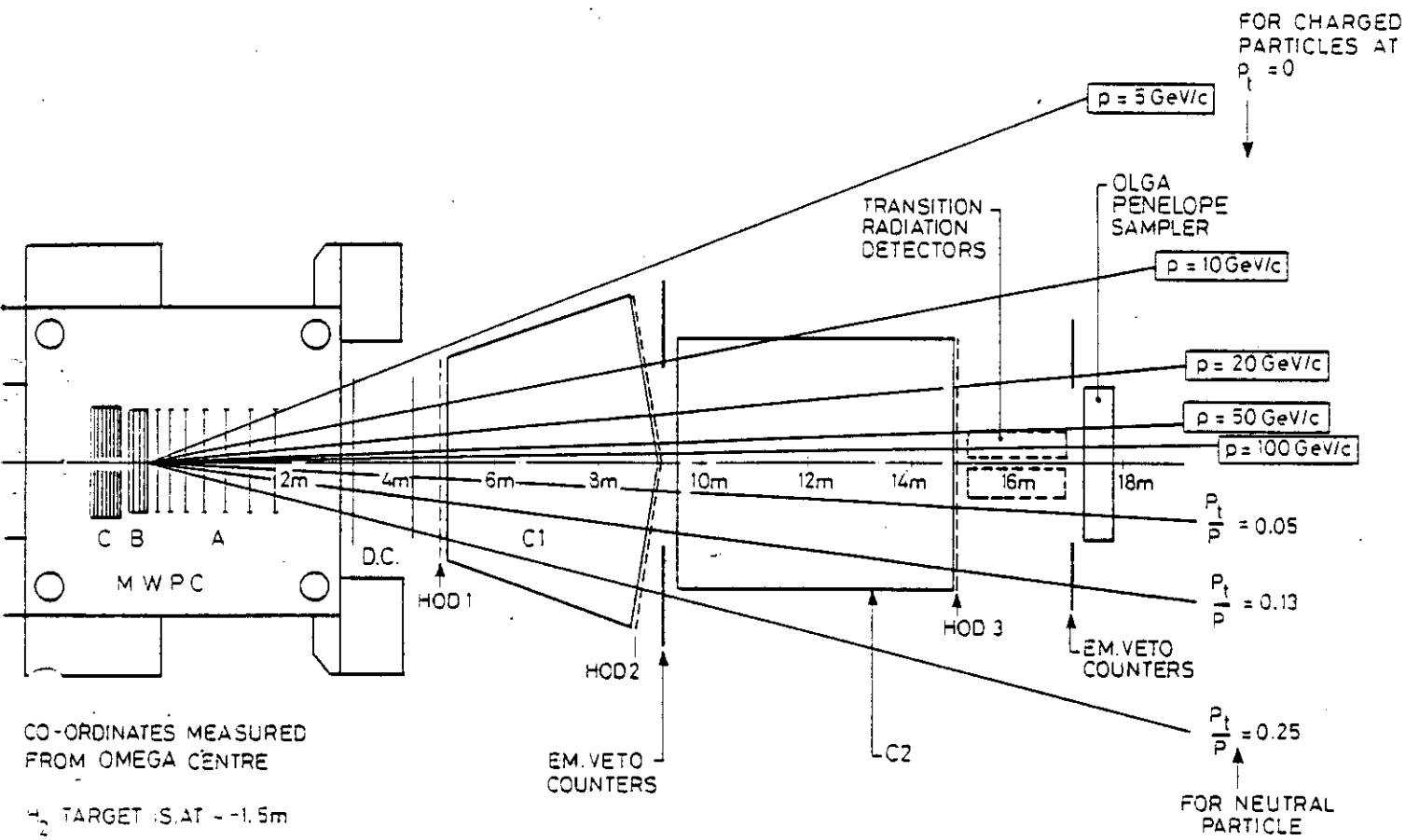
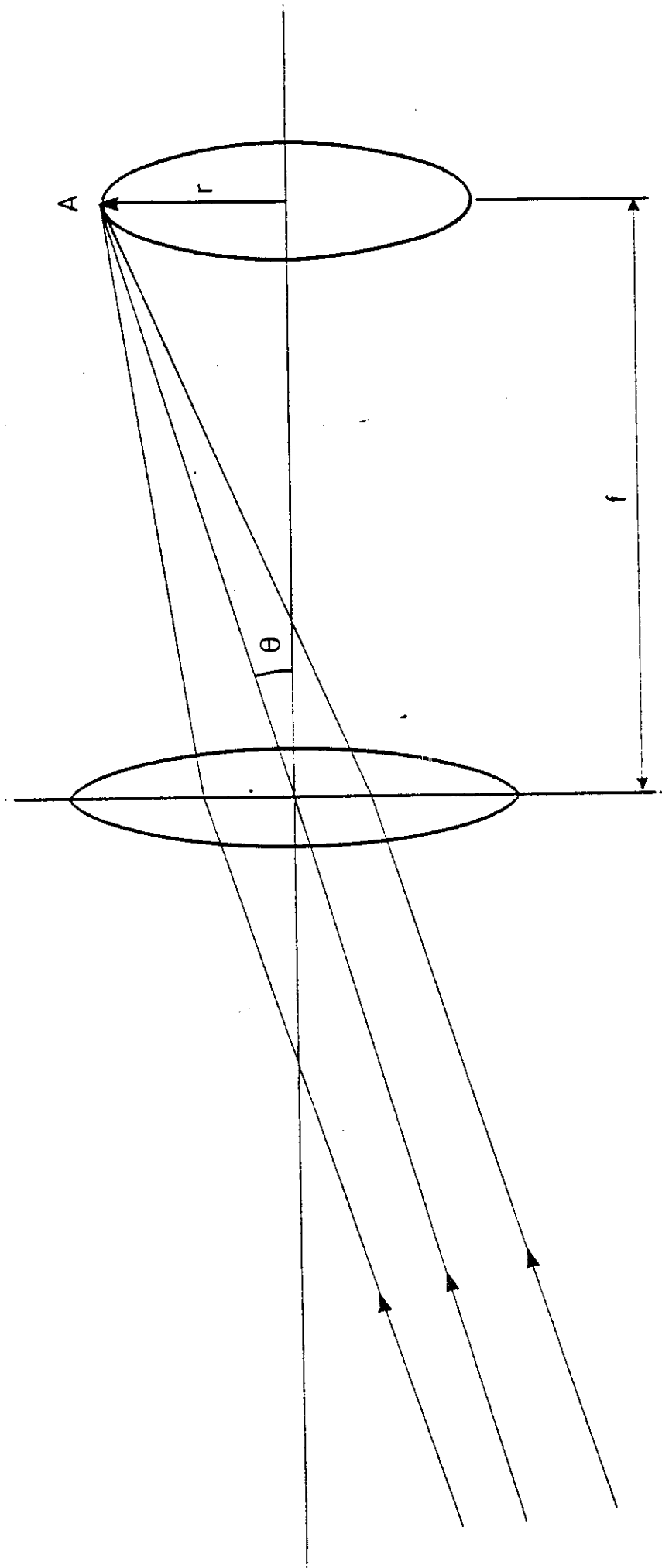


Fig 1



$$r = f \tan \theta$$

Fig 2

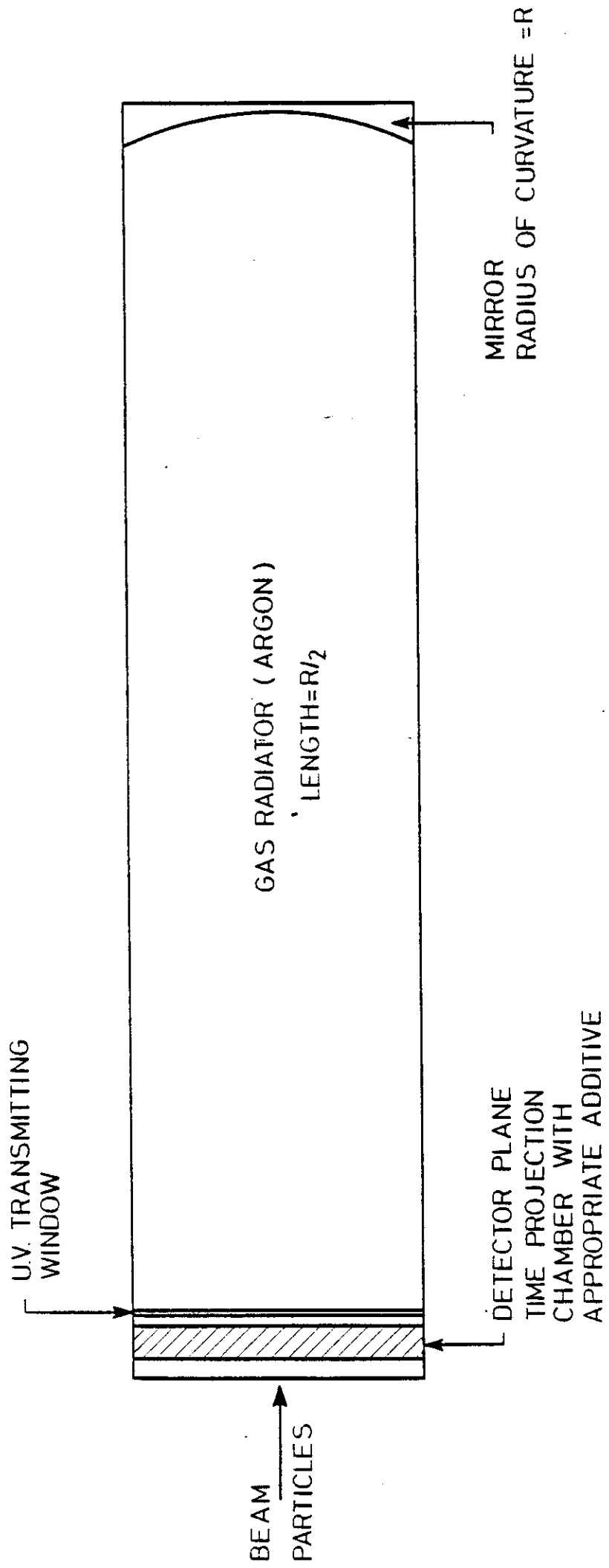


FIG 3

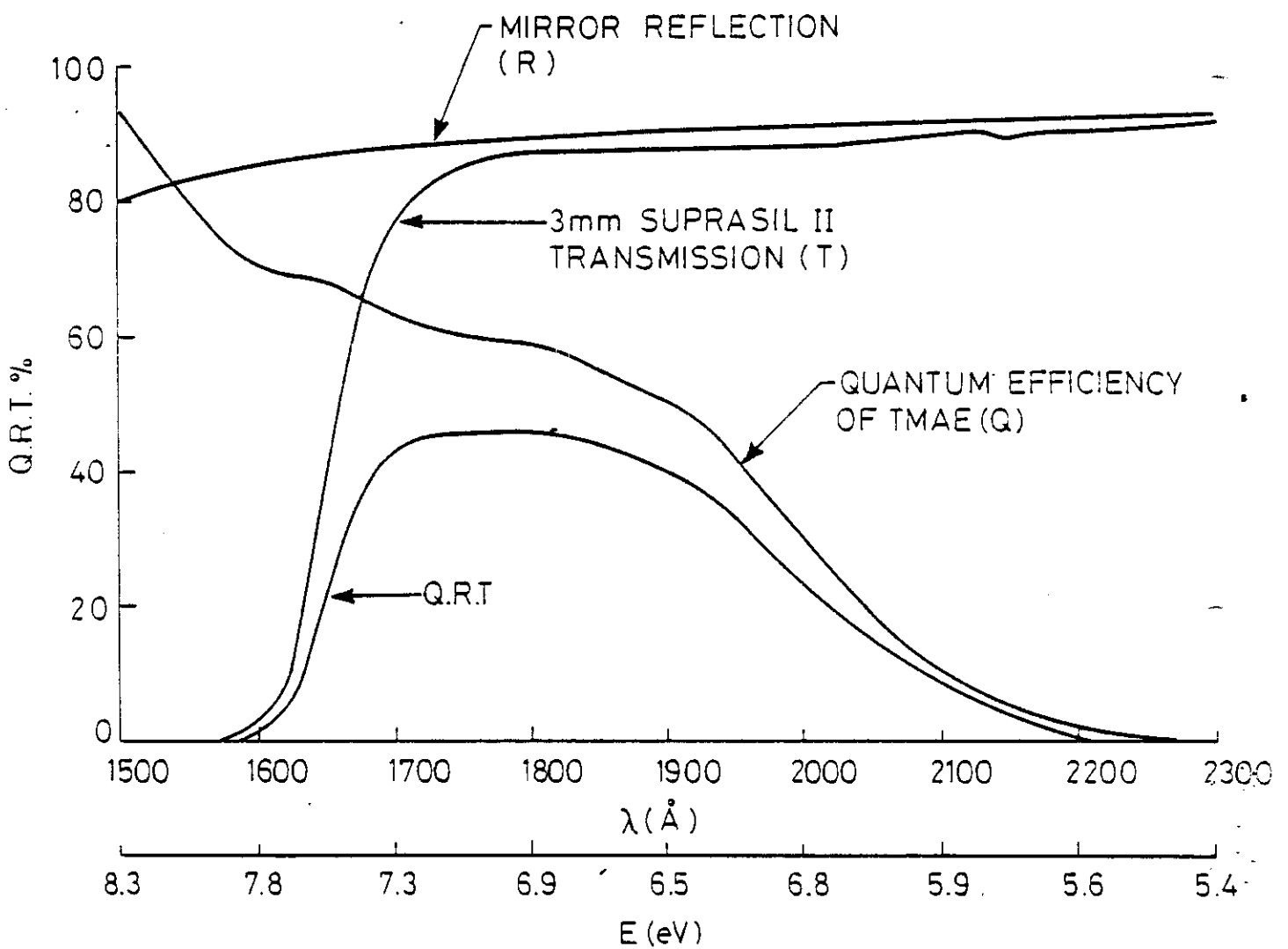


Fig 4

FOR AR β N AT N.I.P.

$n = 1.00034$

5m γ ADIATOR

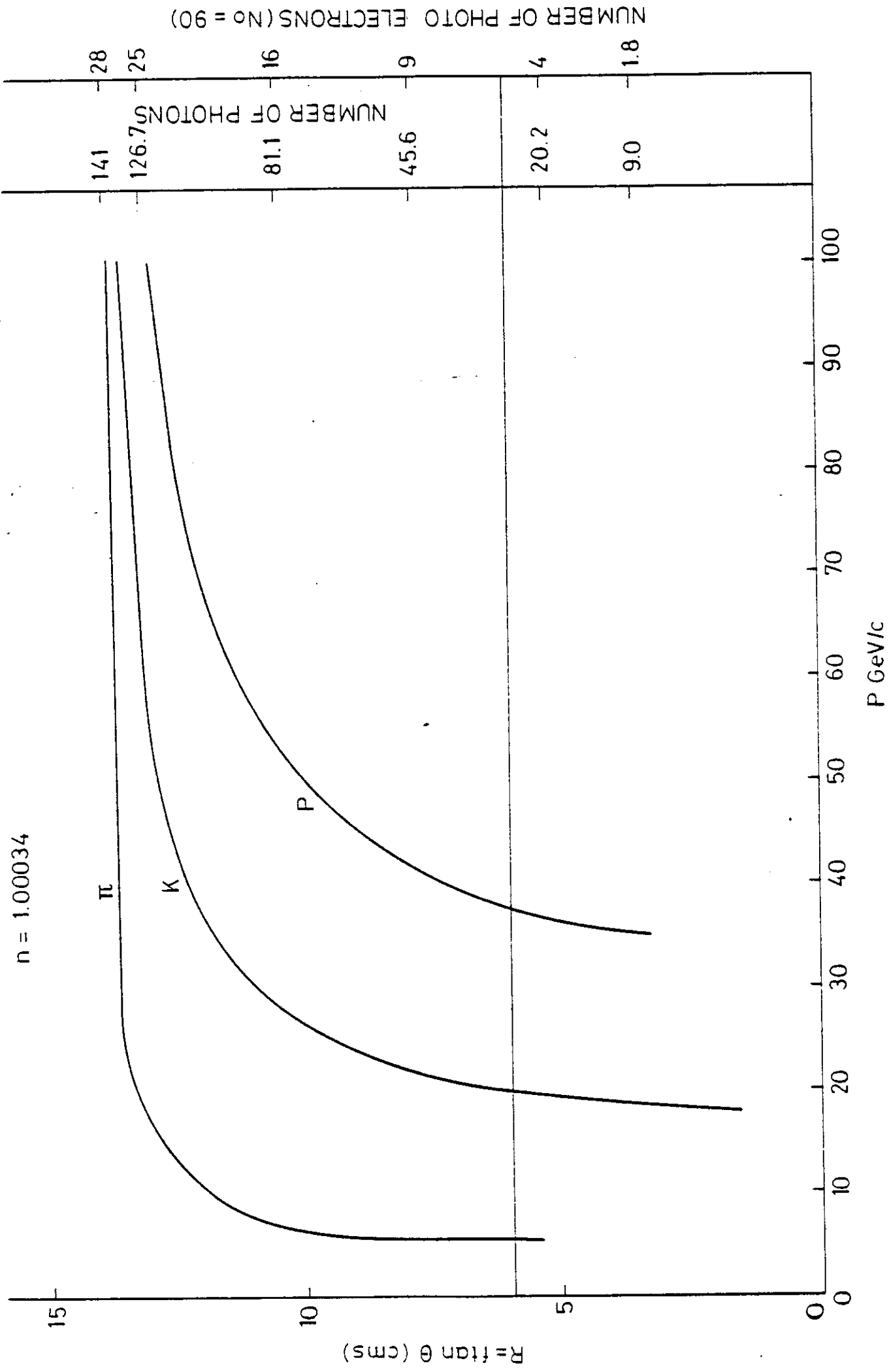


Fig 5

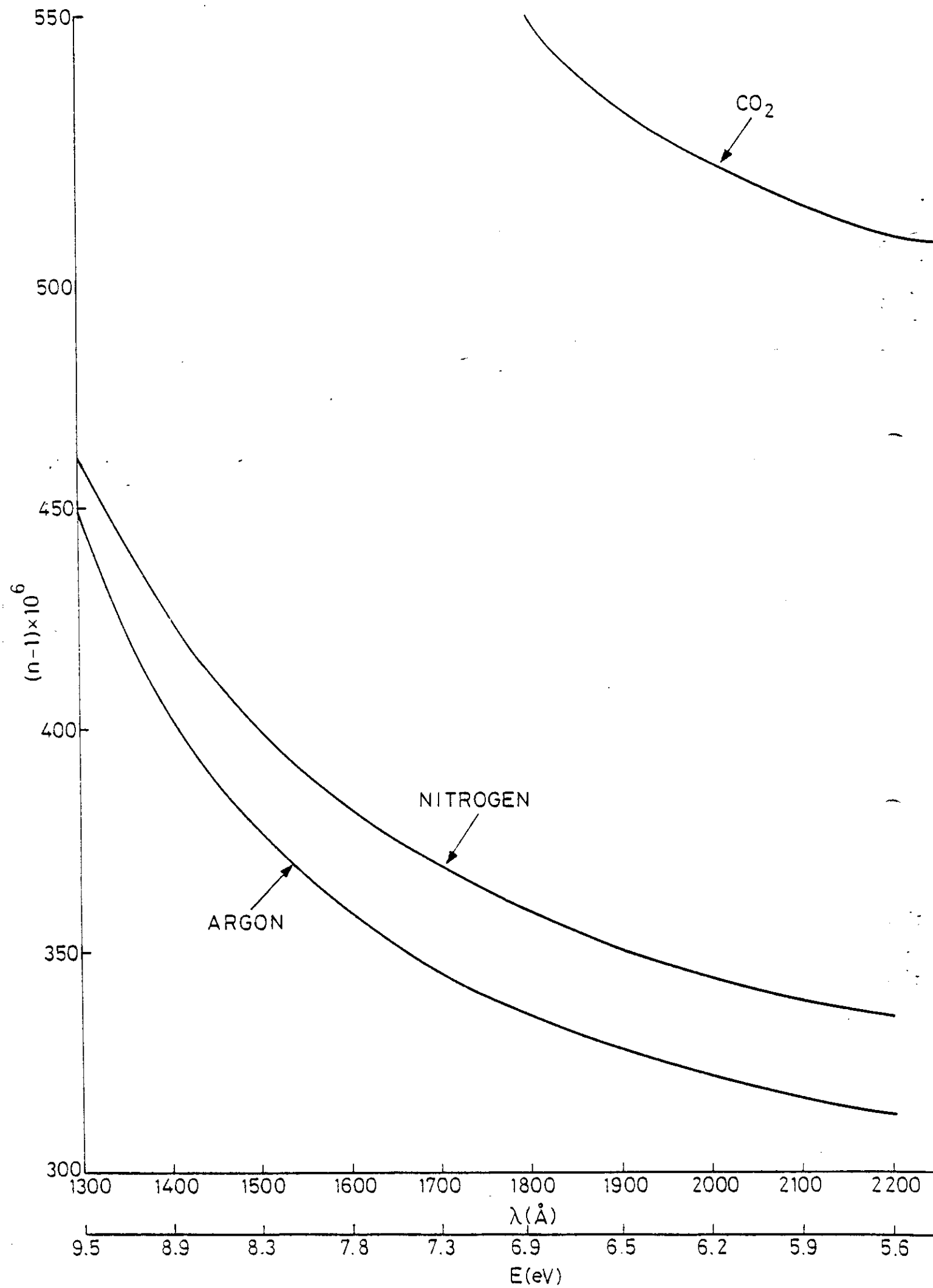


Fig. 6

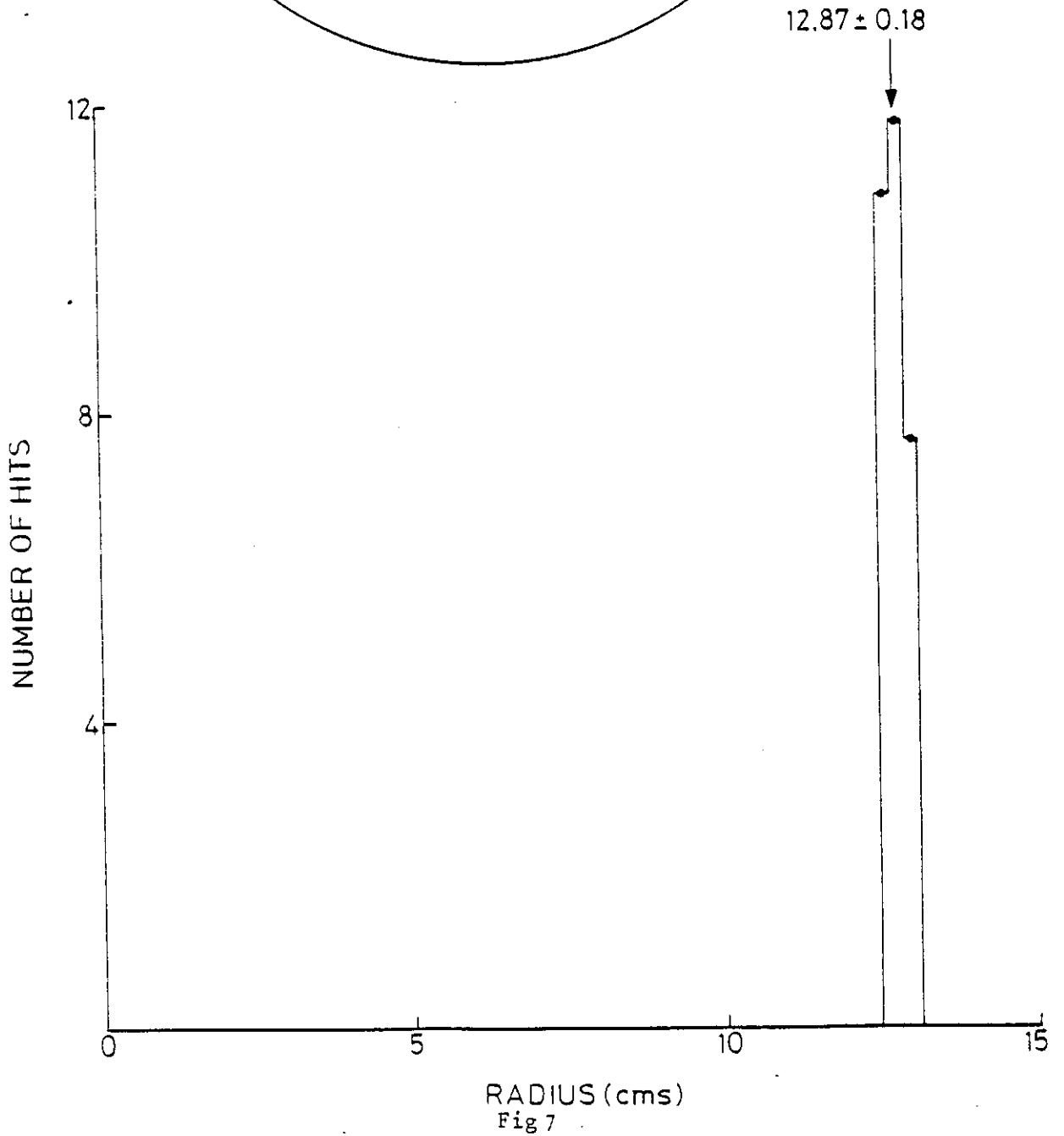
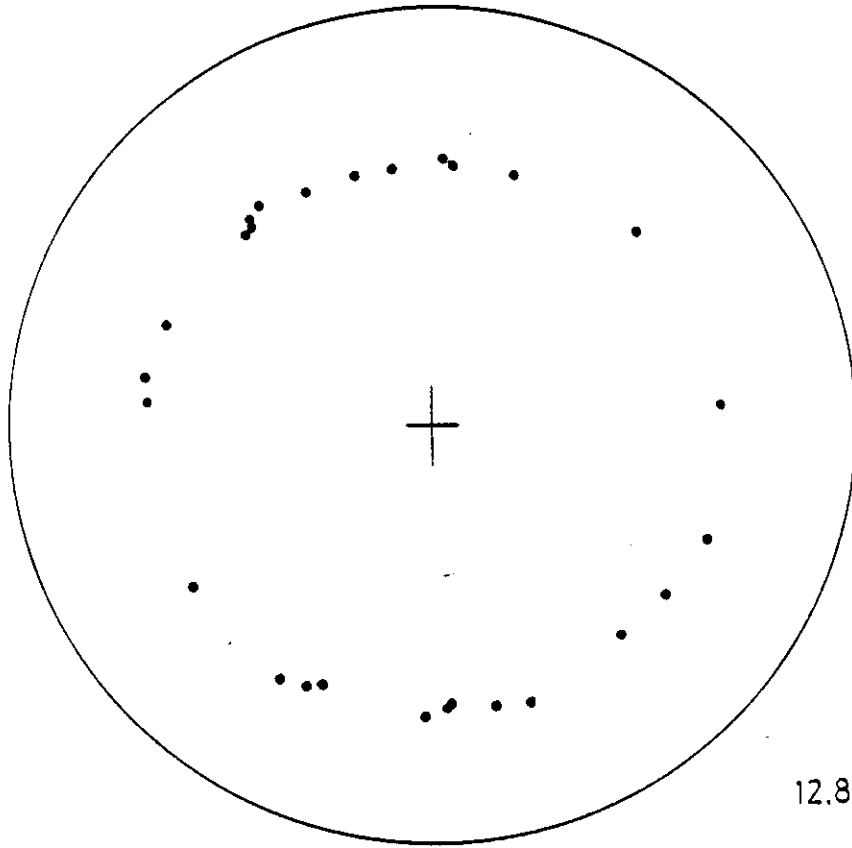


Fig 7

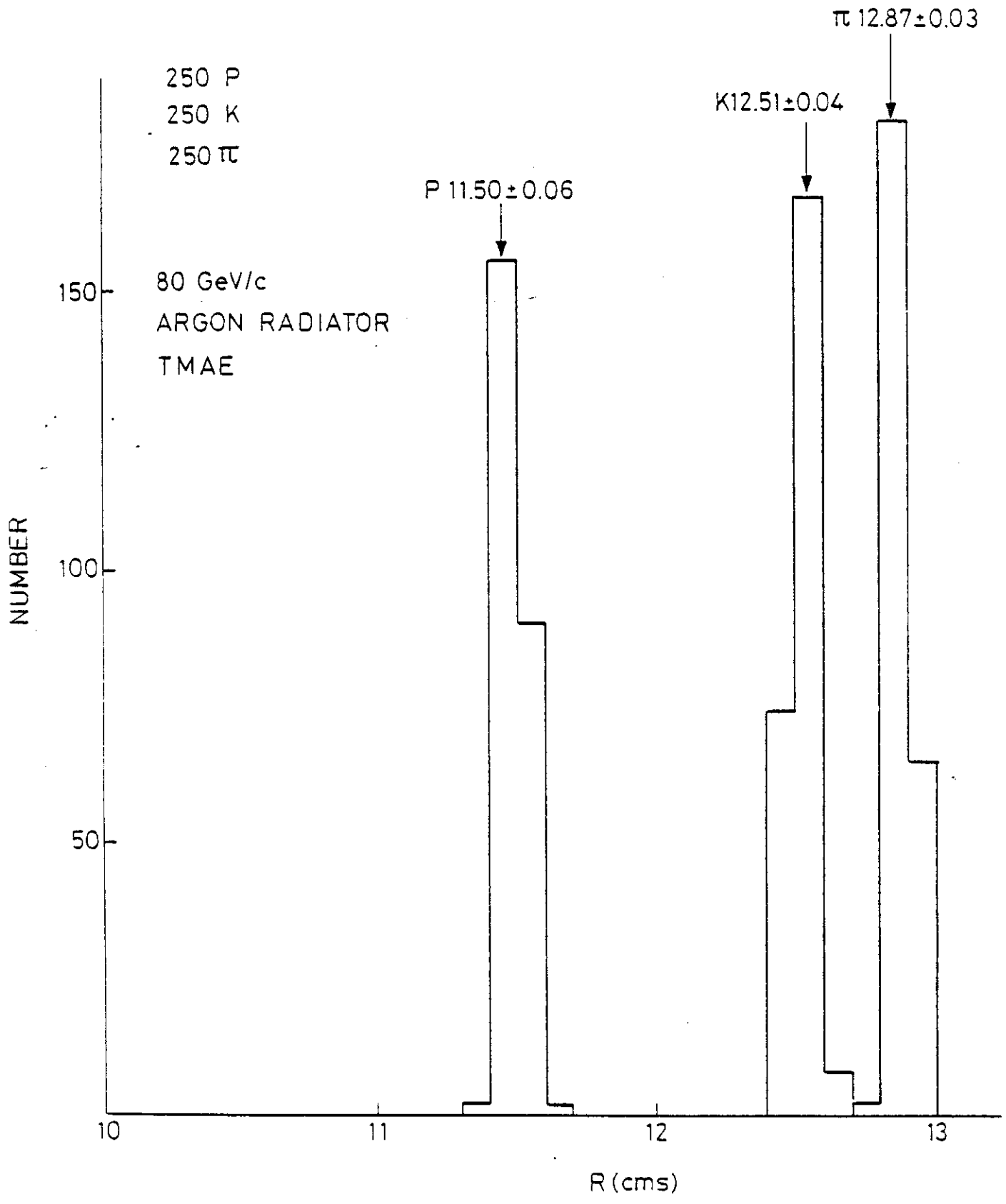


Fig 8

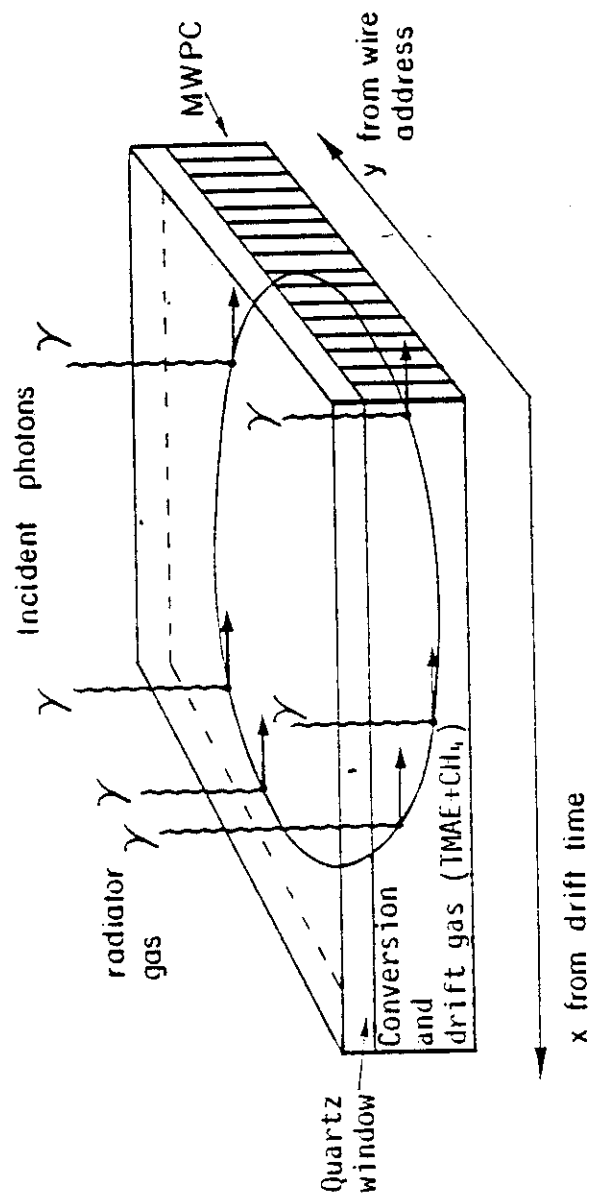


Fig 9

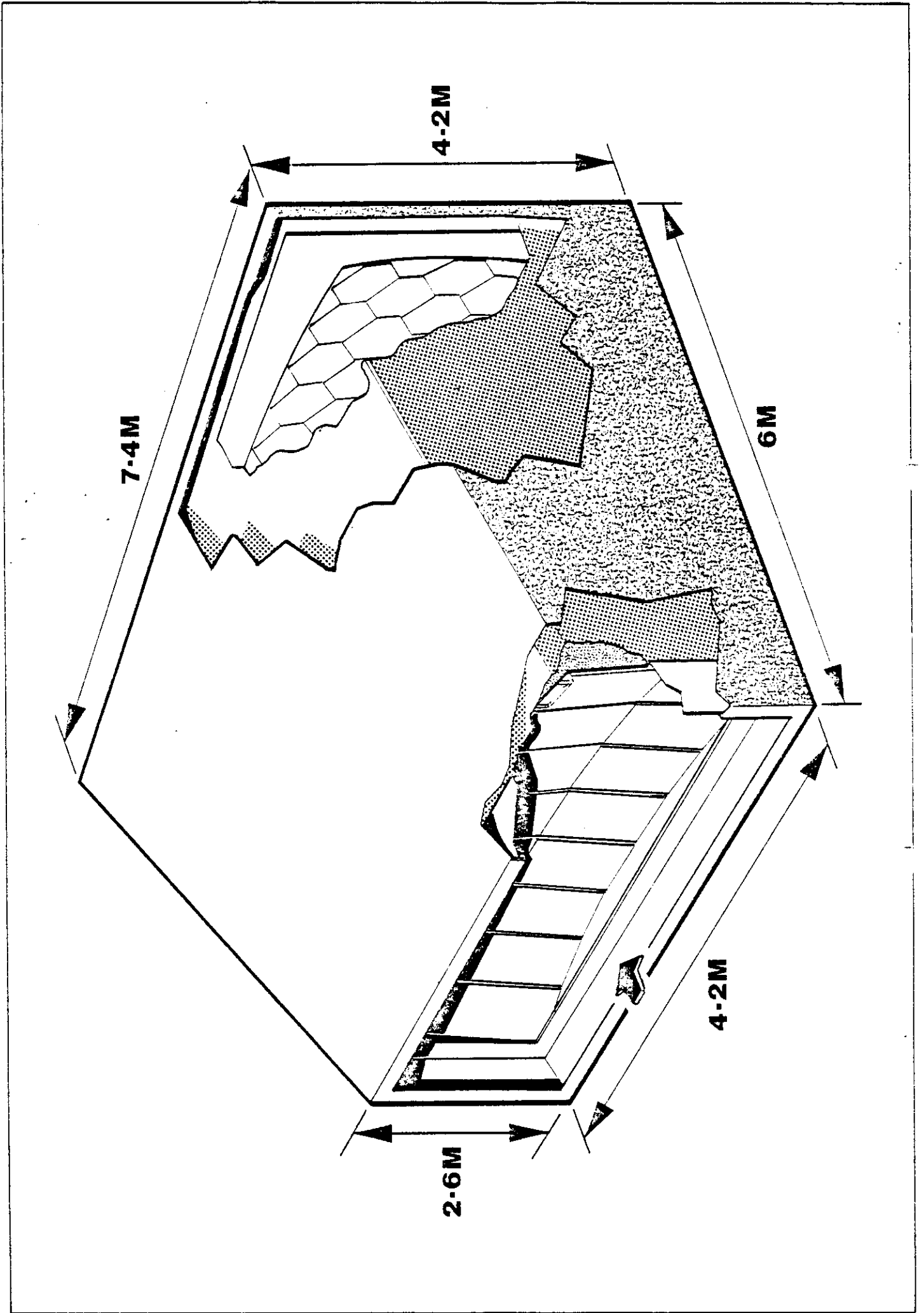


Fig. 10

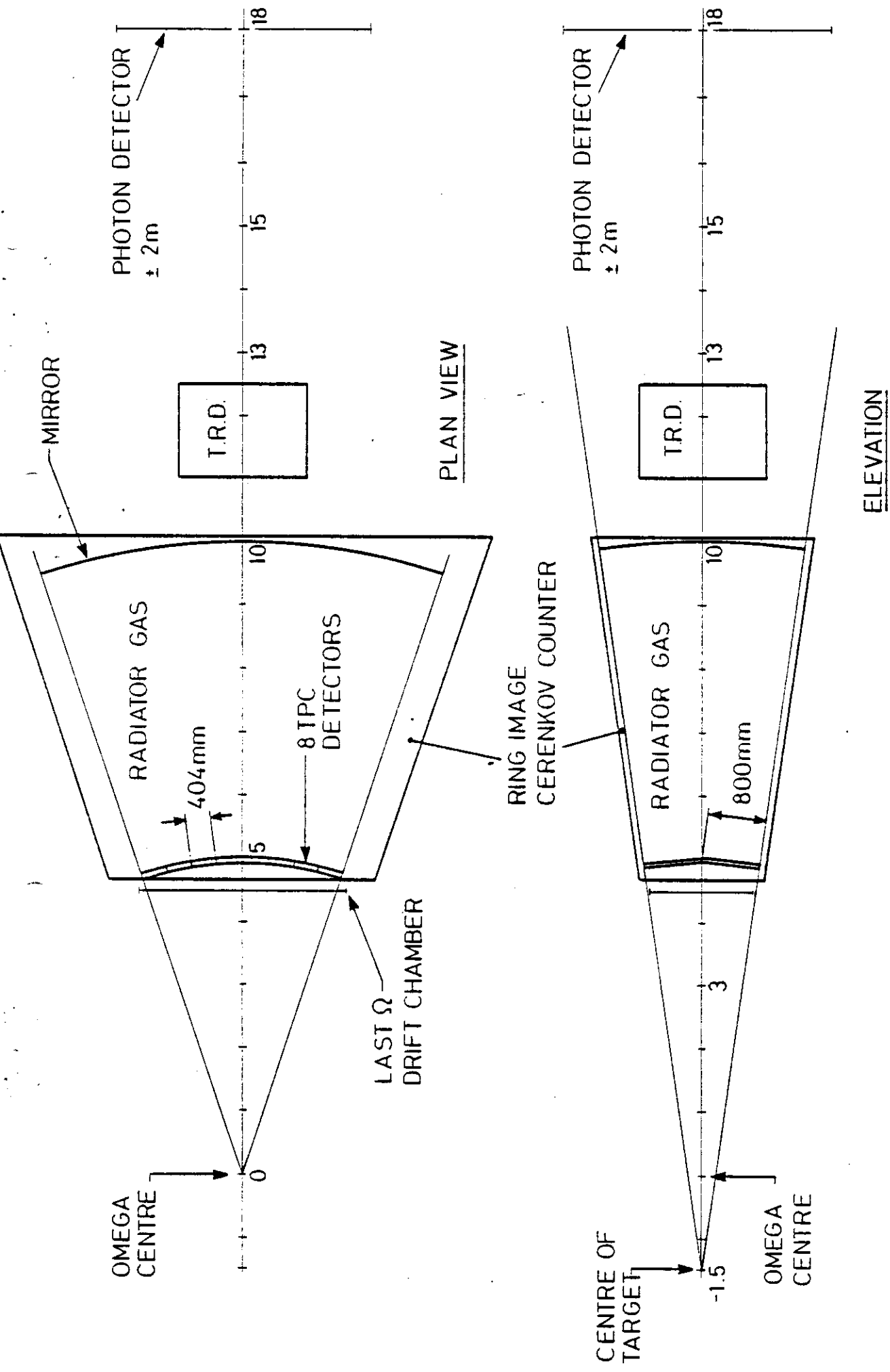


Fig 11

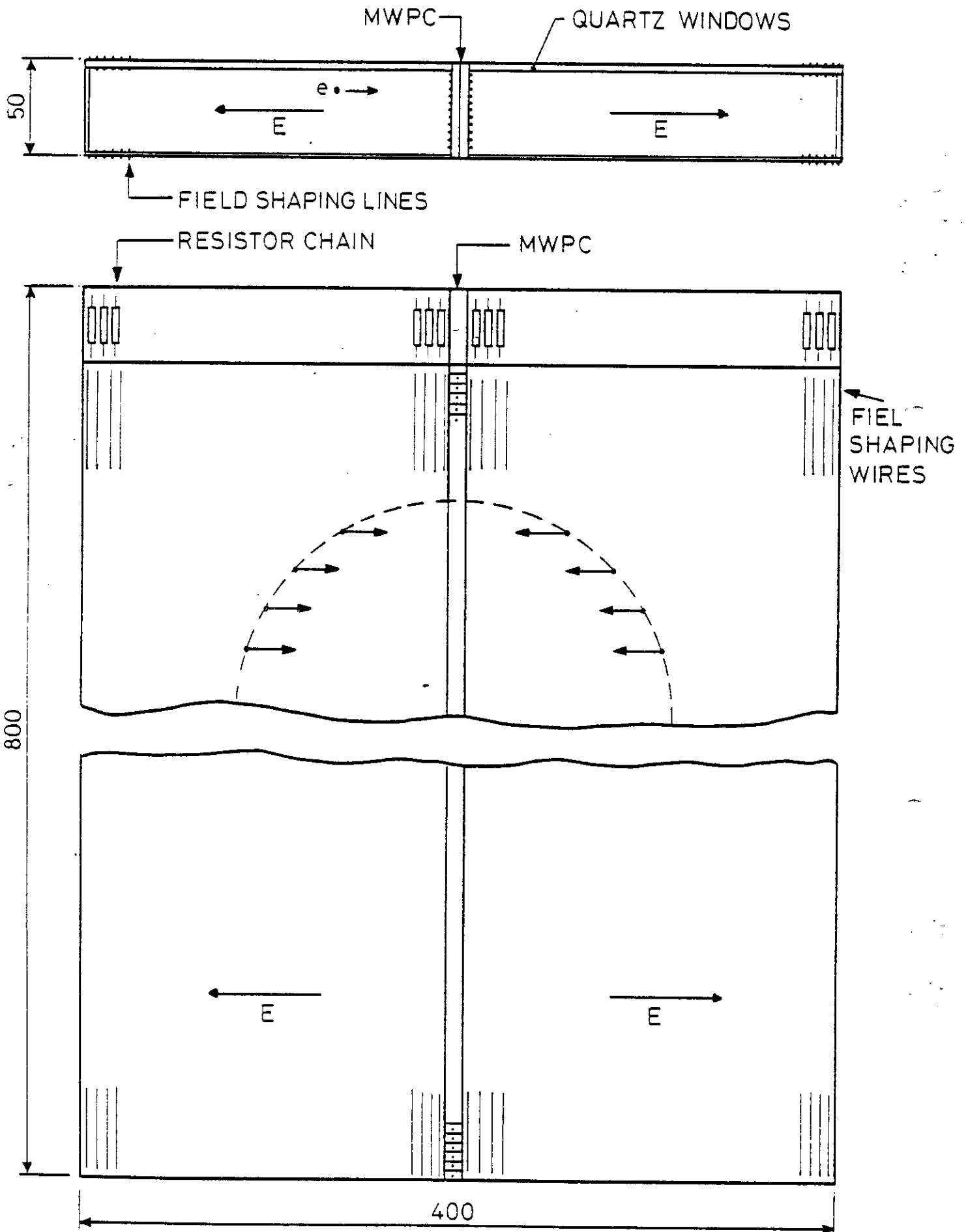


Fig 12

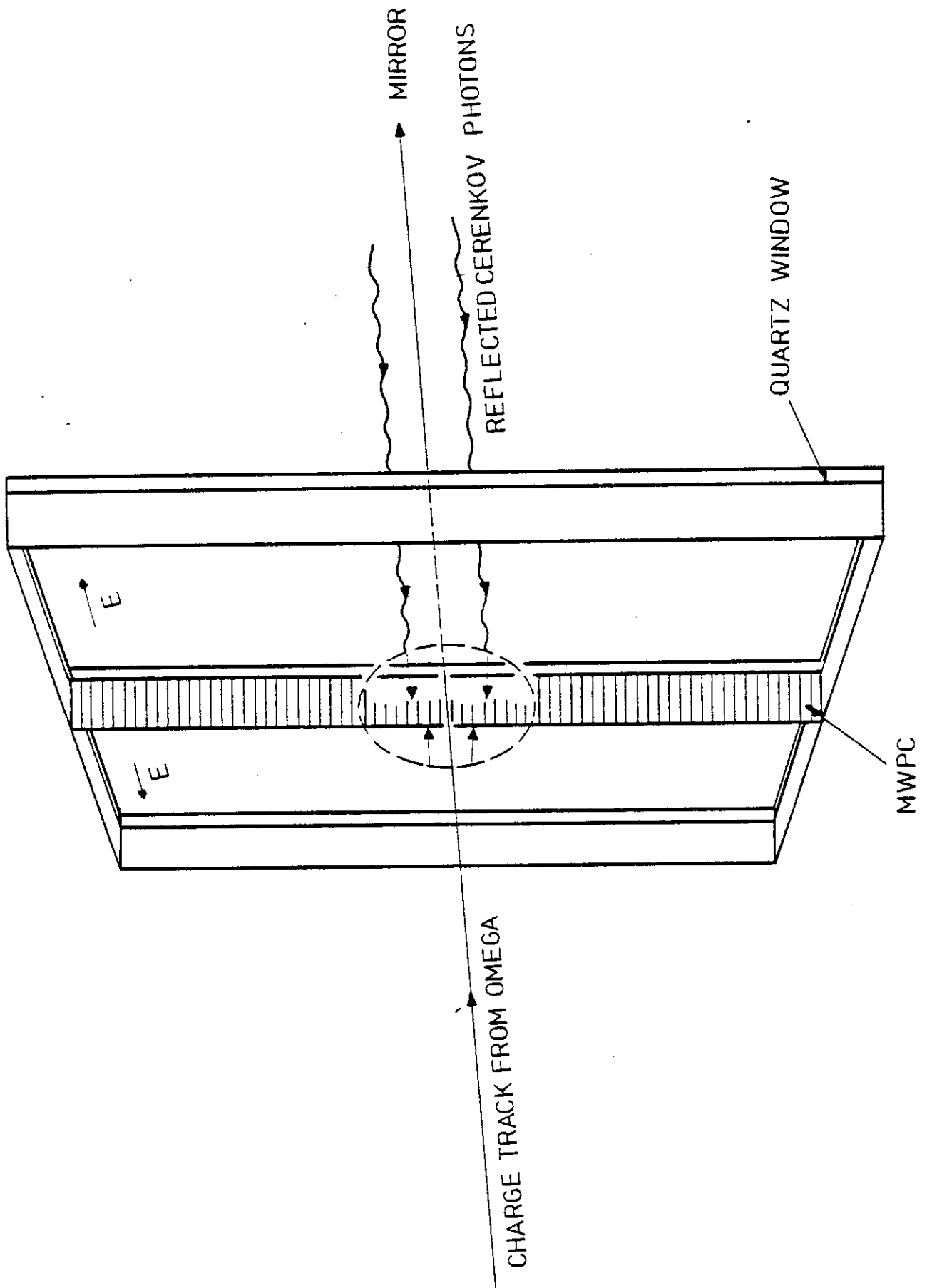


Fig 13

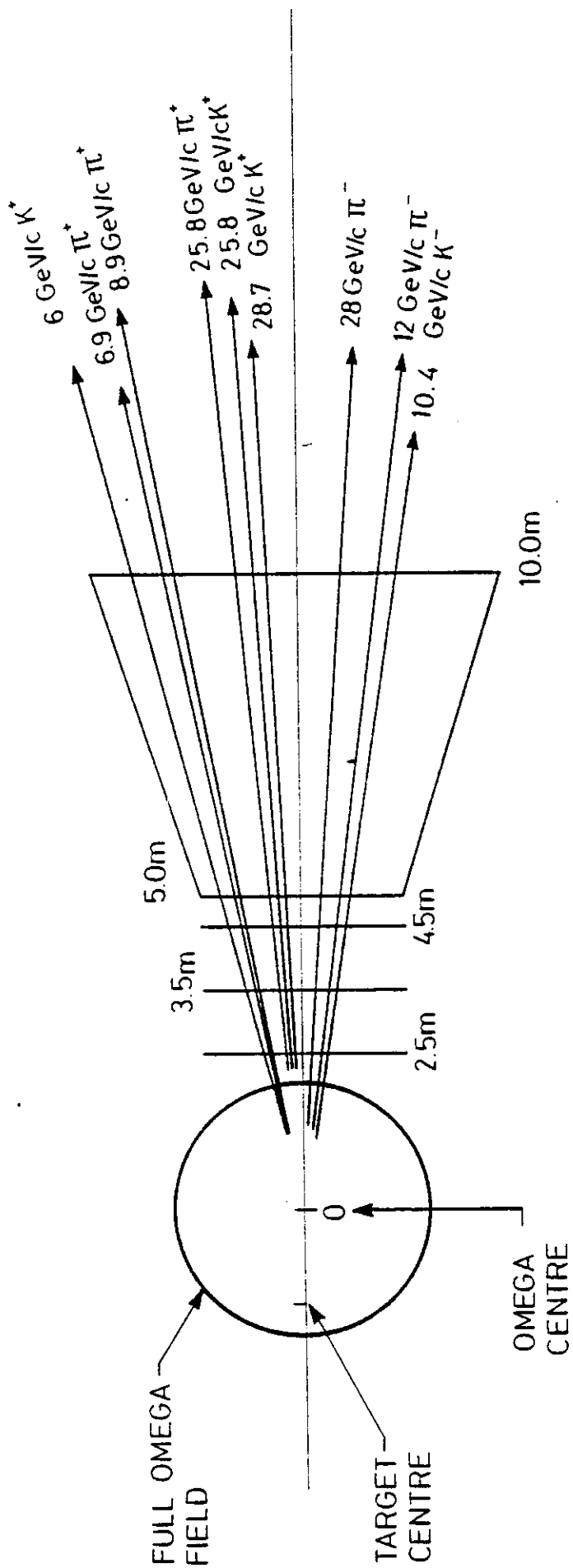


Fig 14

x PION CENTRE
i KAON CENTRE
o PROTON CENTRE
• RING POINT

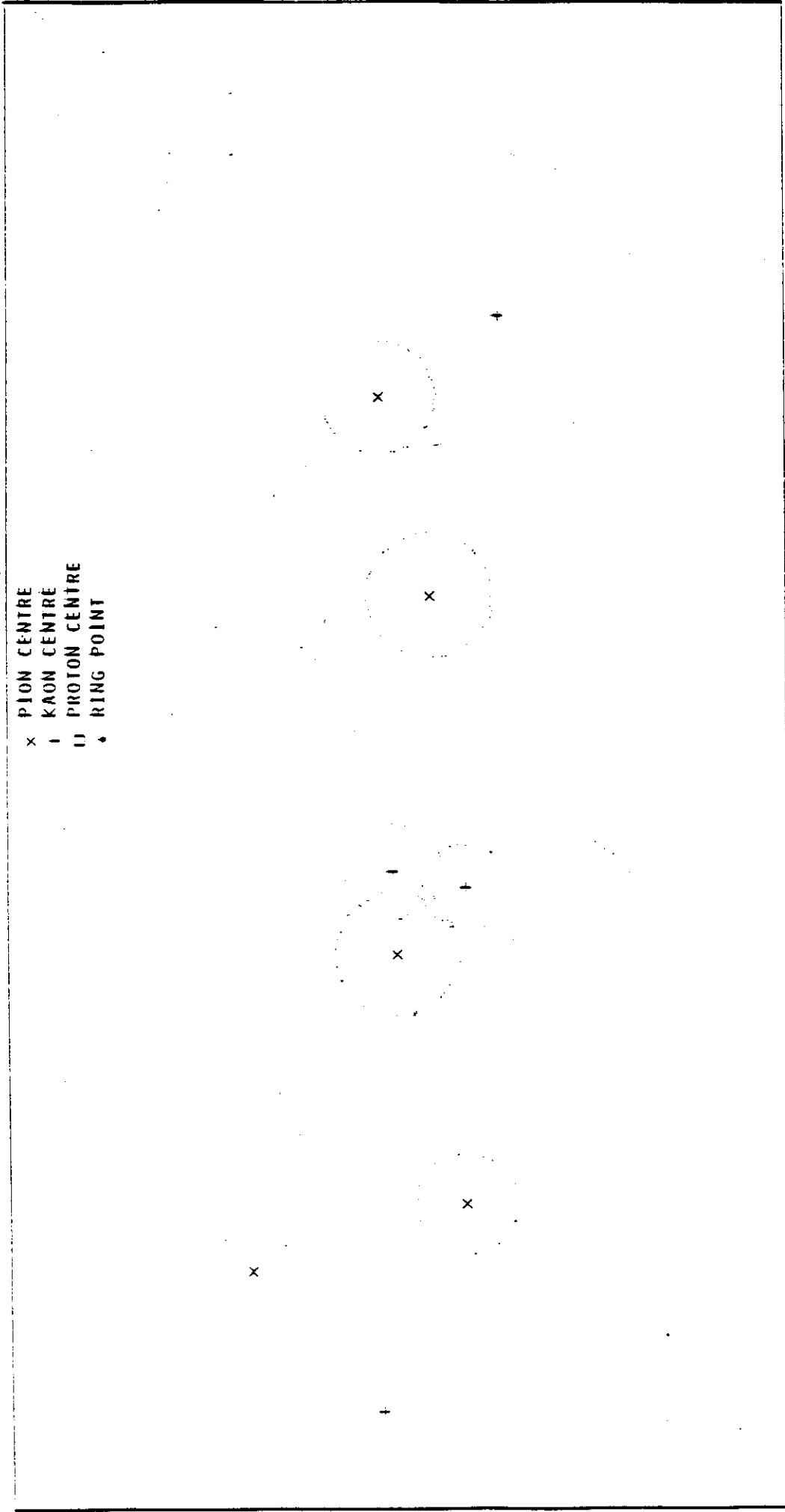


FIG 15

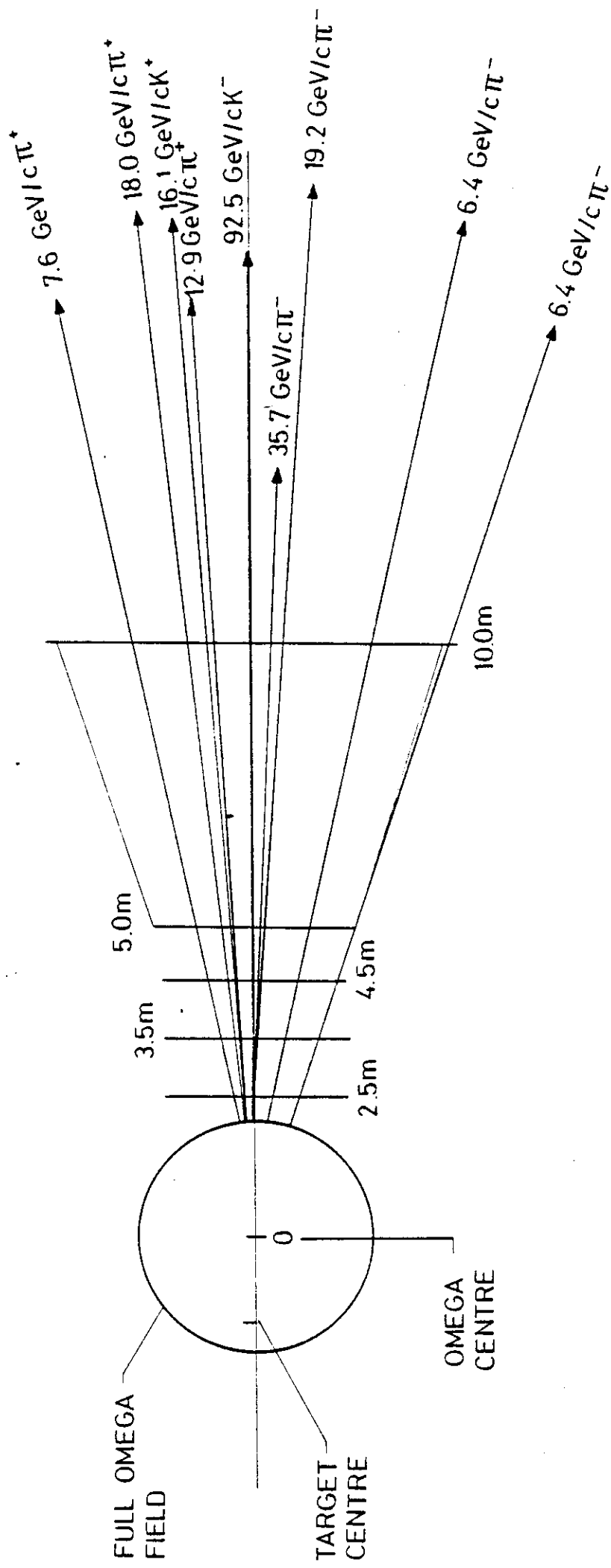


Fig 16

X PION CENTRE
I KAON CENTRE
O PROTON CENTRE
A RING POINT

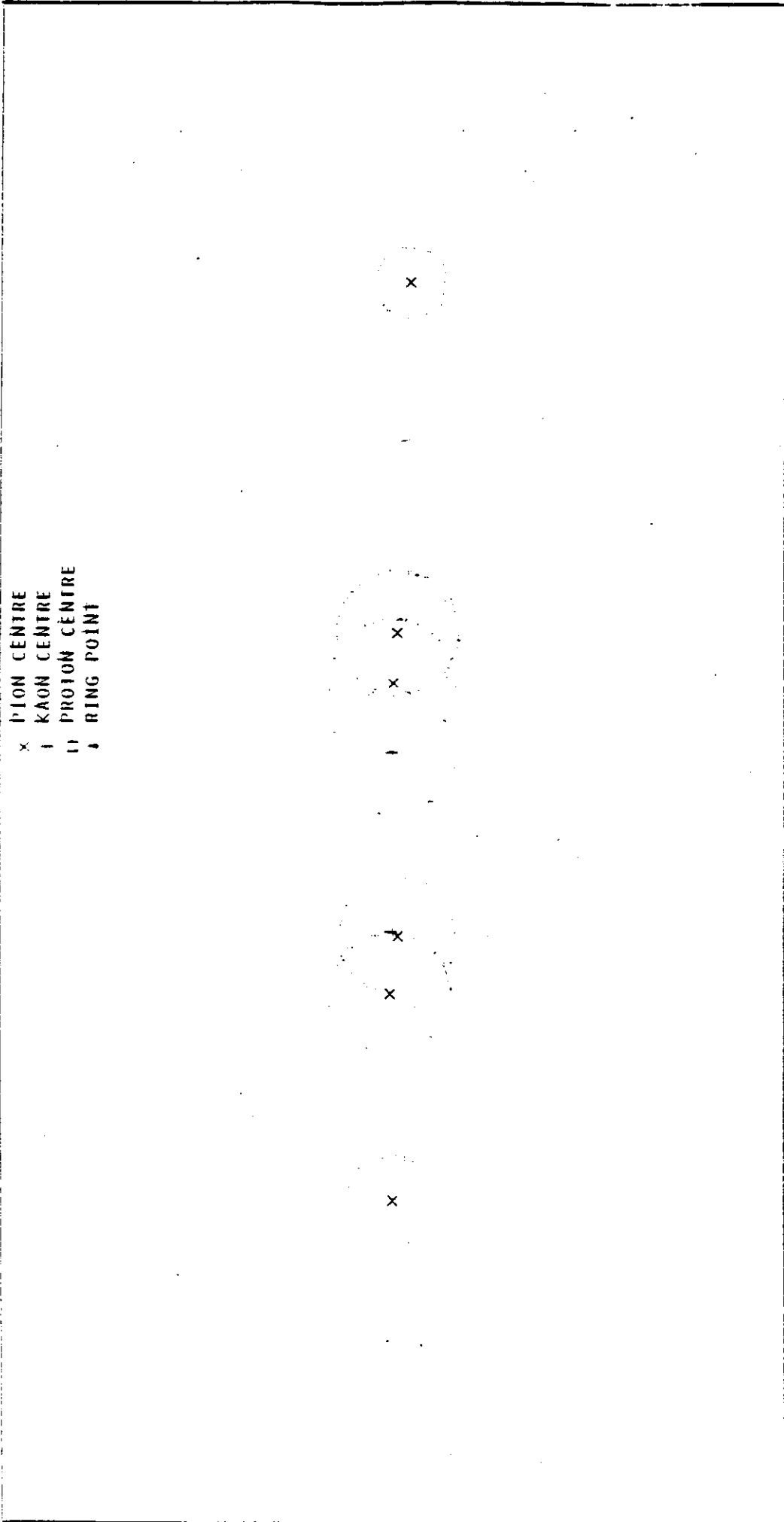
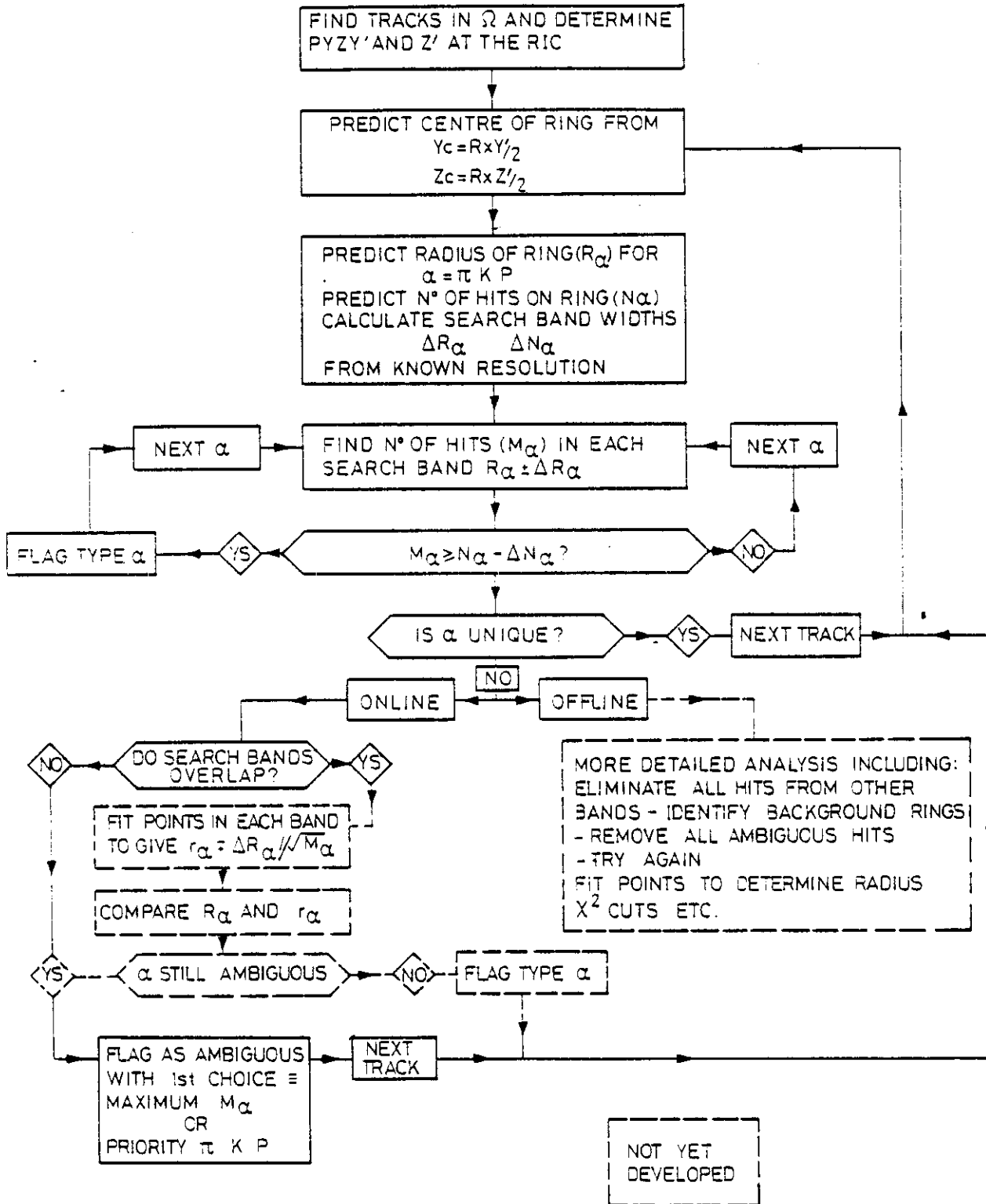


Fig 17



RING IMAGE IDENTIFICATION FLOW CHART

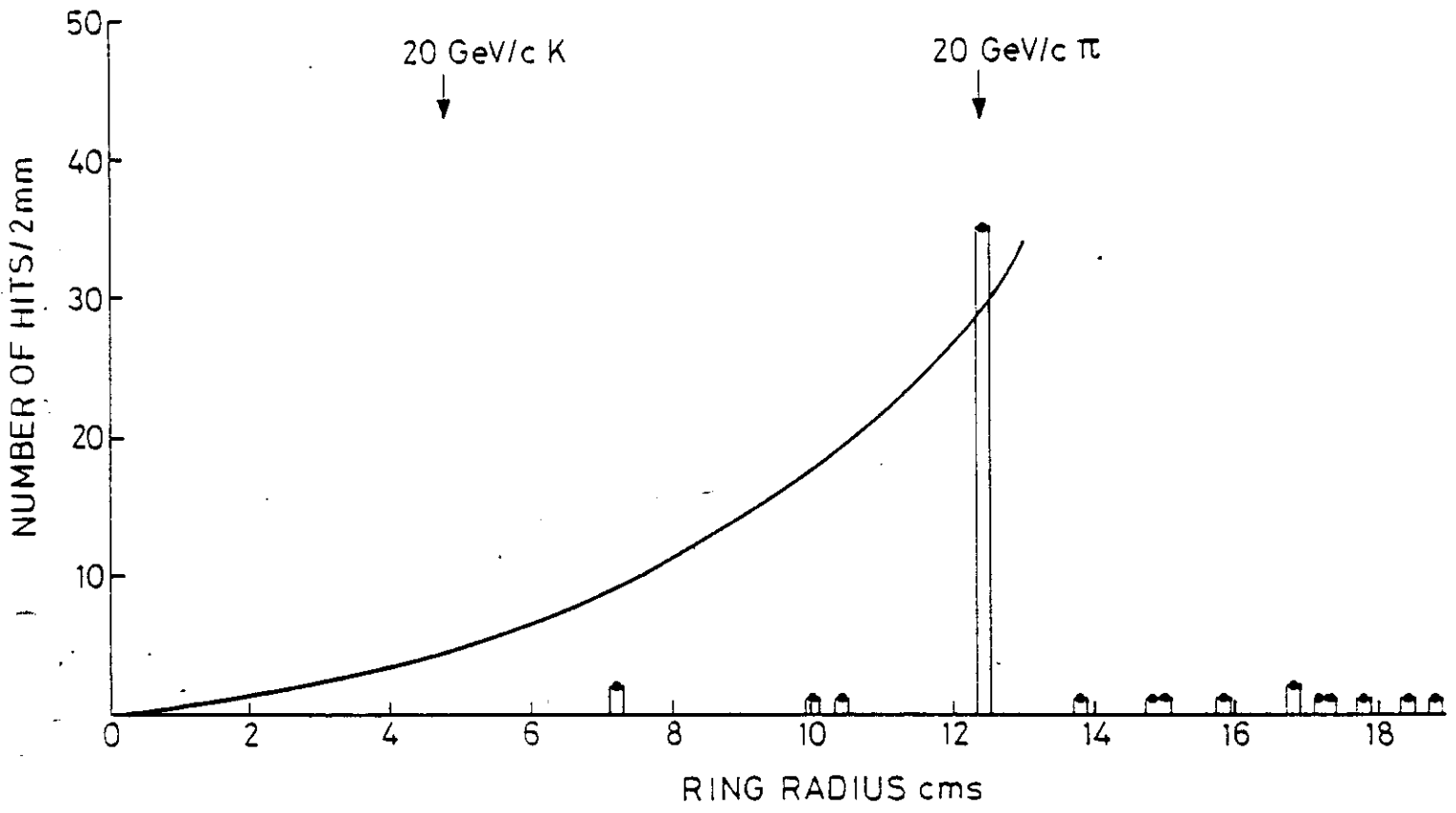


Fig 19

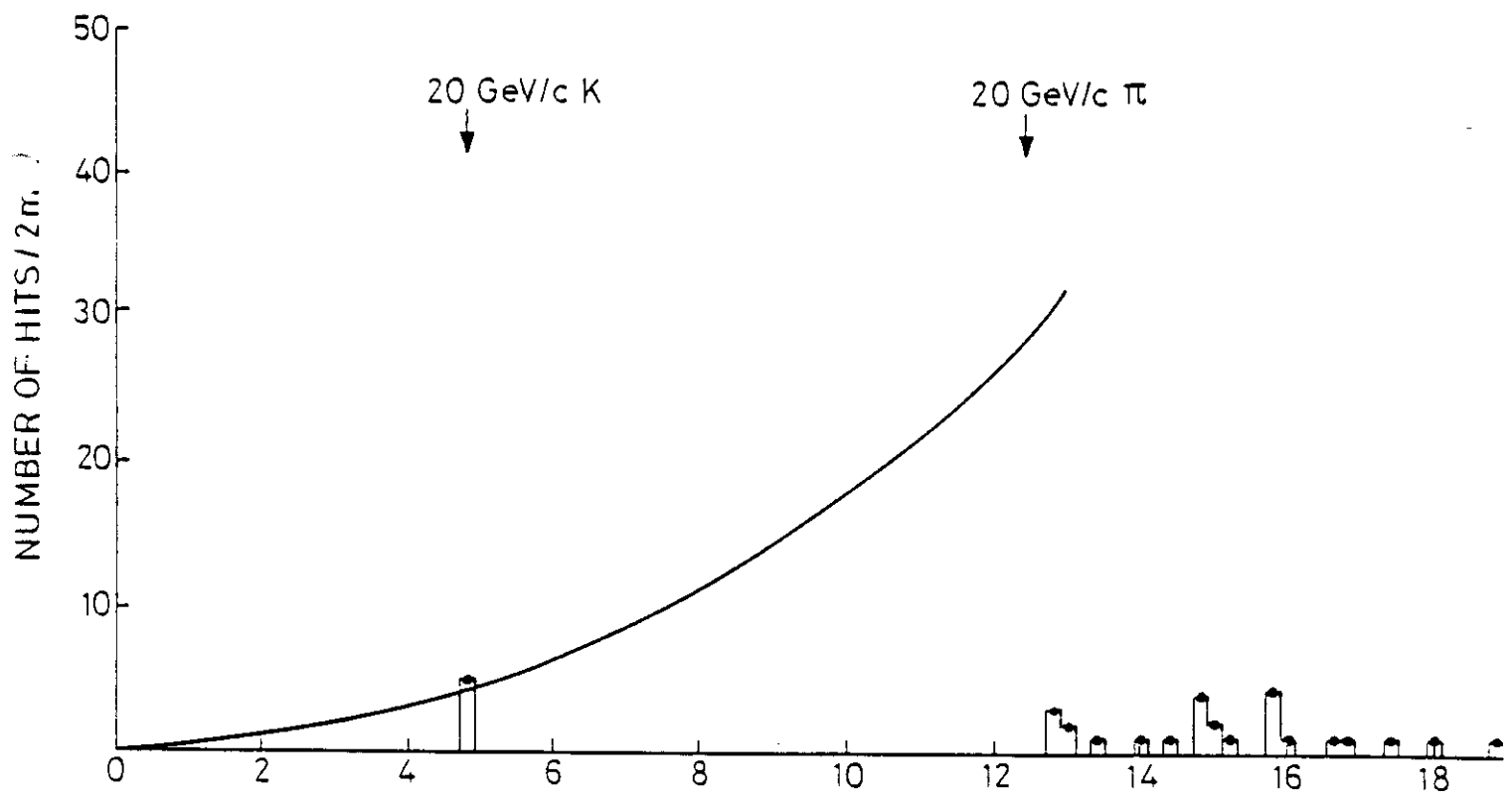


Fig 20

x PION CENTRE
+ KAON CENTRE
□ PROTON CENTRE
• RING POINT



FIG 21

1st. CHOICE IDENTIFICATION EFFICIENCY

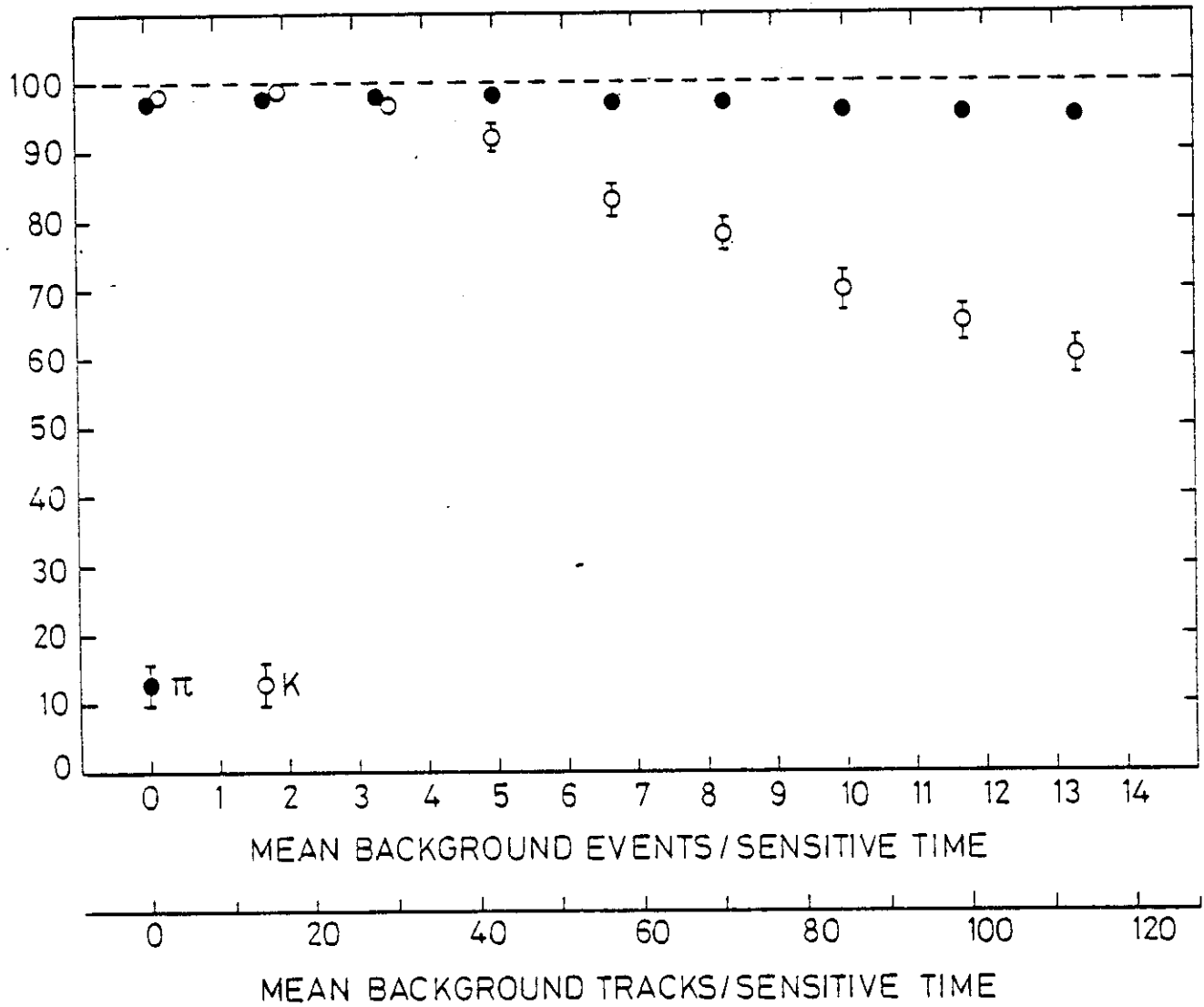


Fig 22

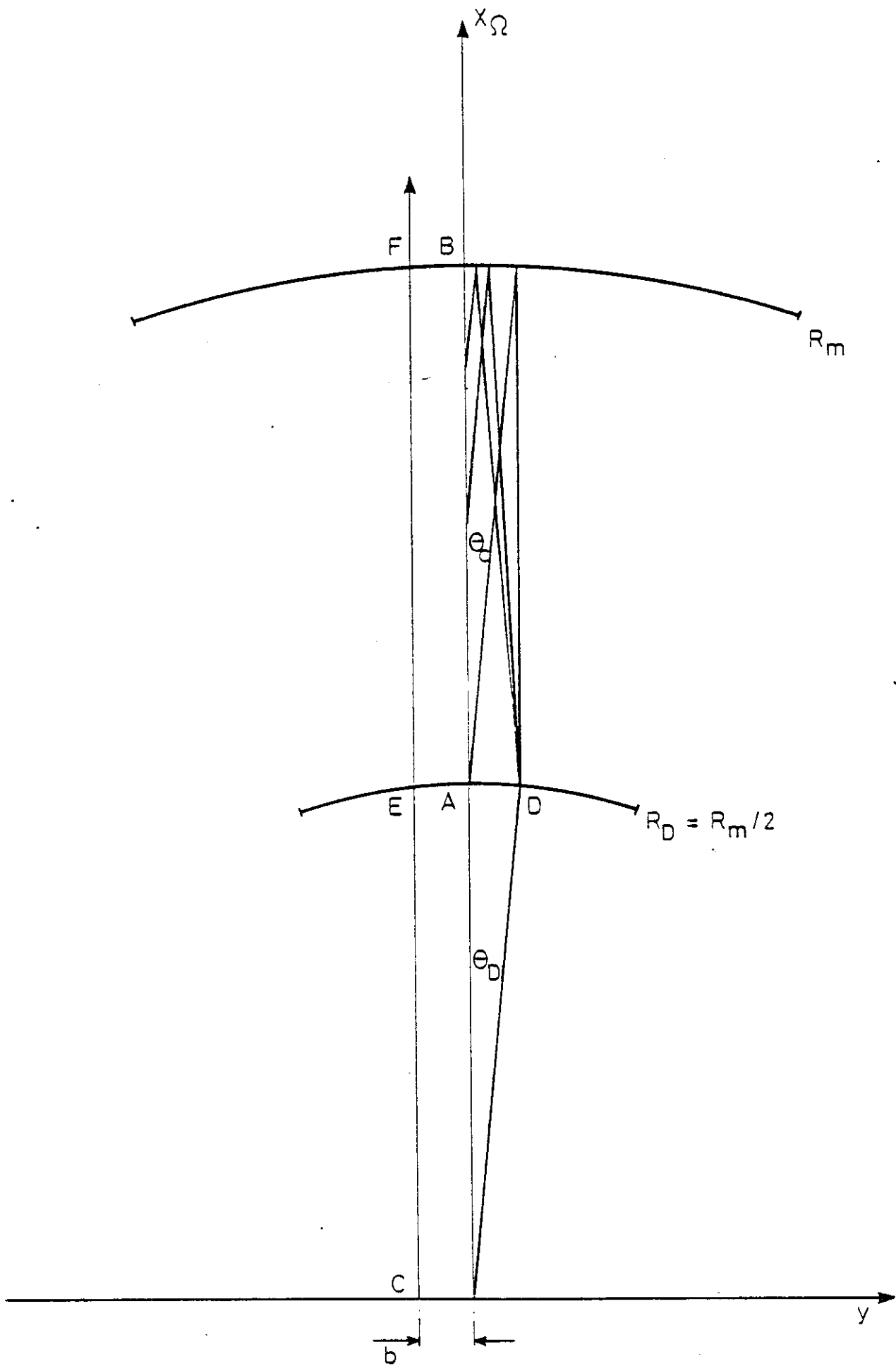


Fig 23

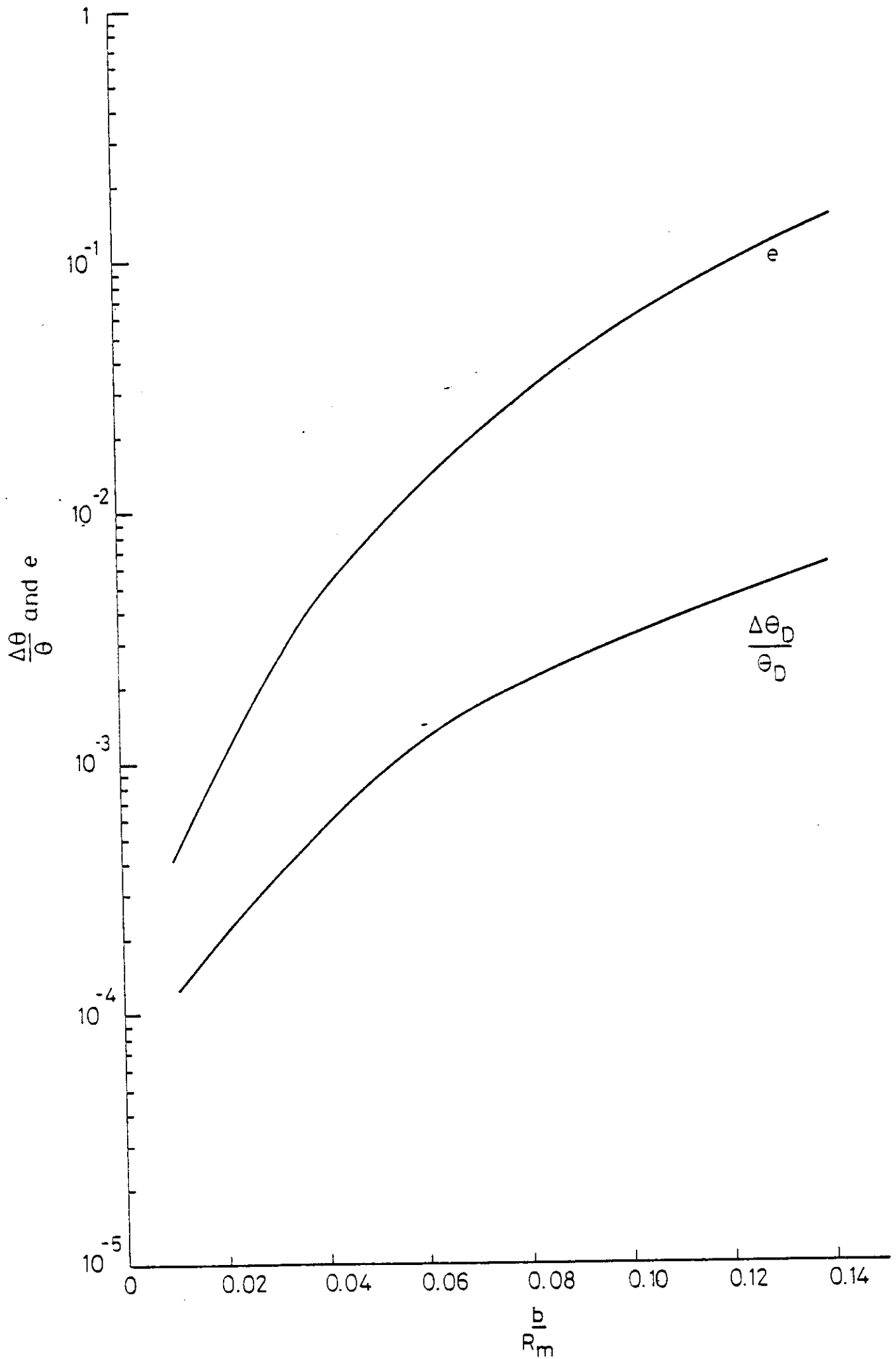
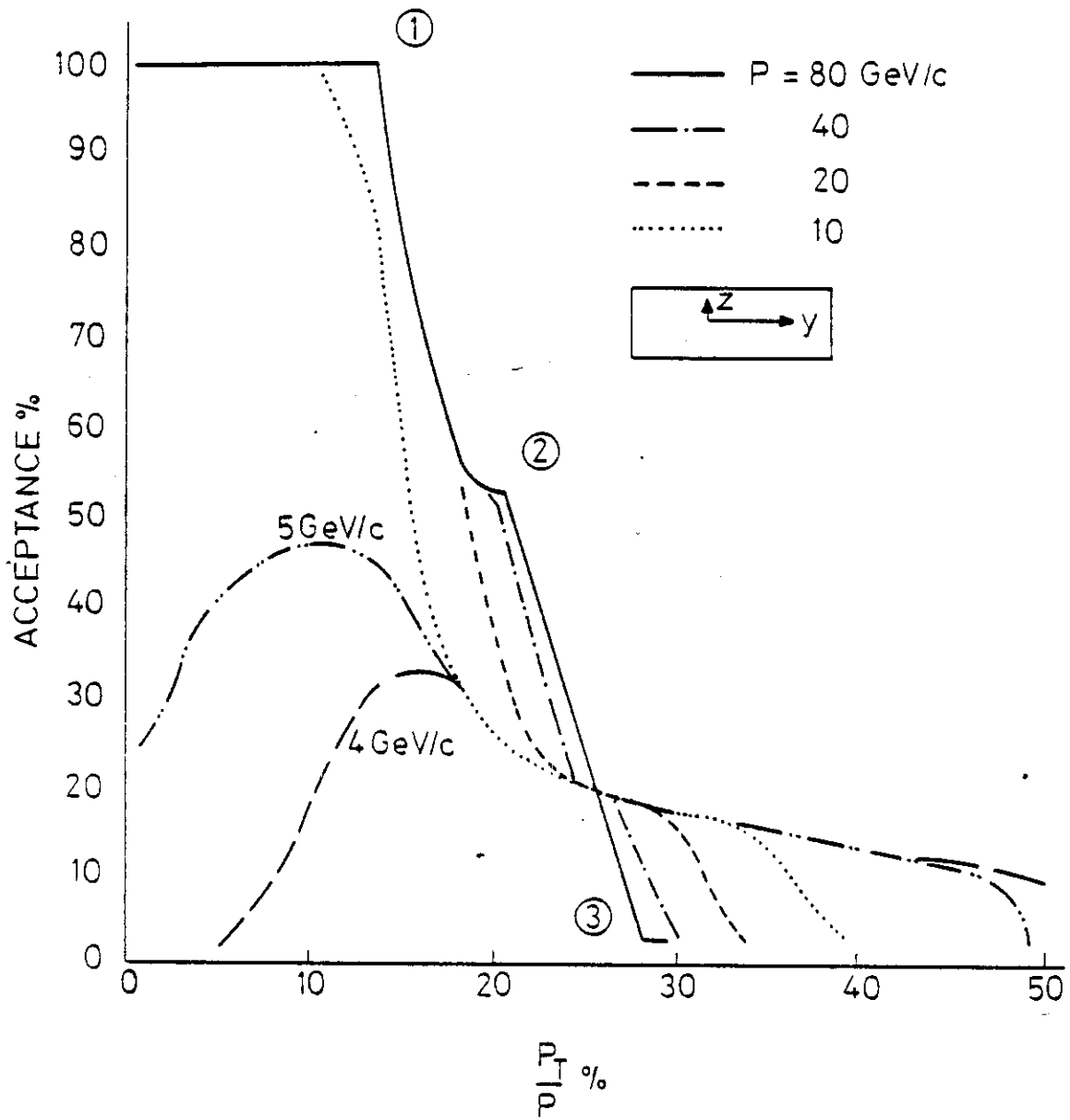


Fig 24



RING IMAGE DETECTOR AT $X_{\Omega} = + 500\text{cm}$

TARGET AT $- 135\text{cm}$

RING IMAGE APERTURE $\Delta Z = \mp 90\text{cm}$

$\Delta Y = \mp 160\text{cm}$

- ① IS FIXED BY ΔZ
- ② IS FIXED BY ΔY
- ③ IS FIXED BY $(\Delta Z^2 + \Delta Y^2)^{1/2}$

Fig 25

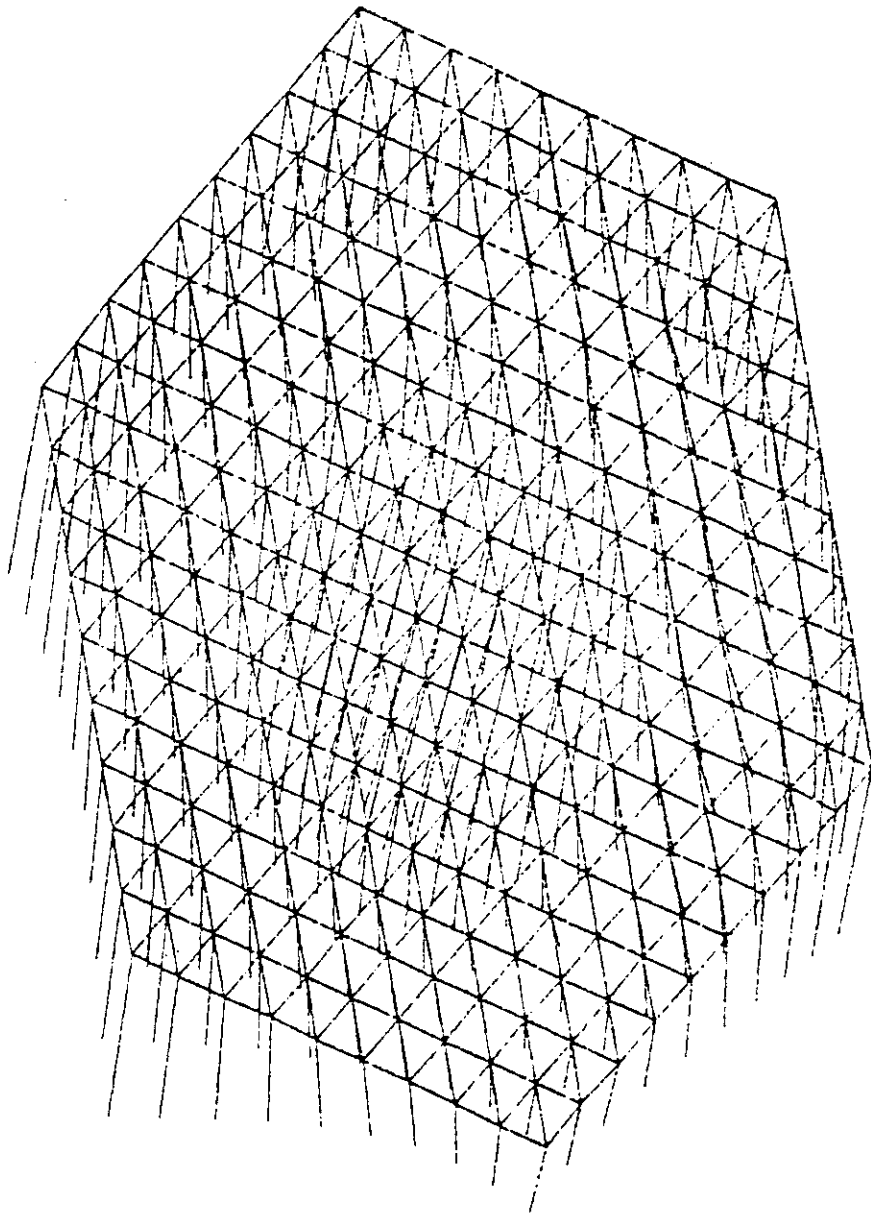
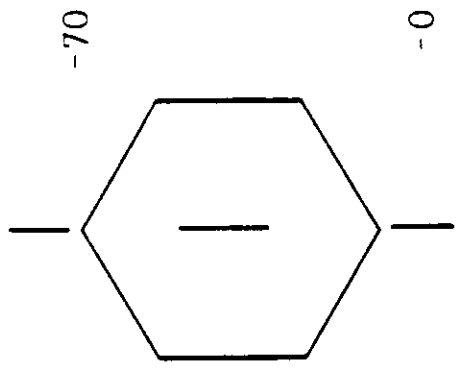
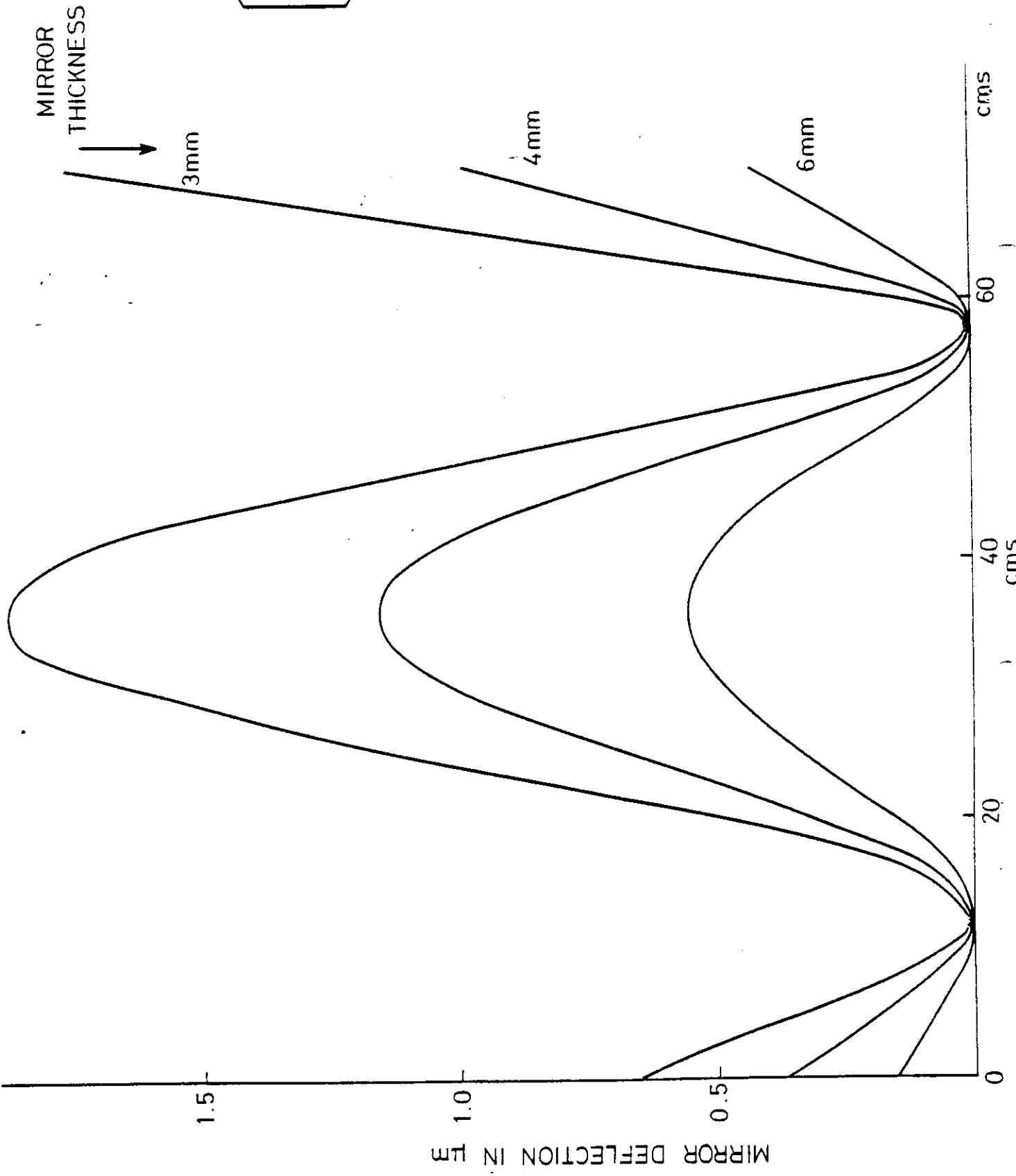


Fig 26



DISPLACEMENT PROFILES FOR 3, 4 AND 6mm THICK MIRRORS

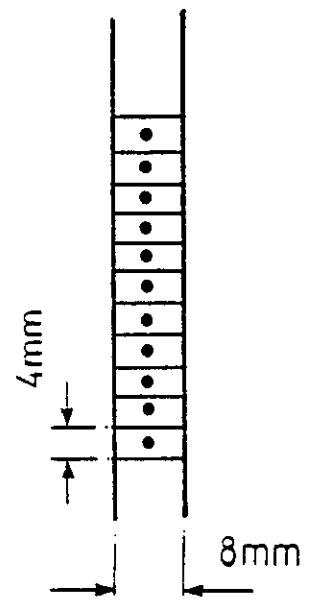
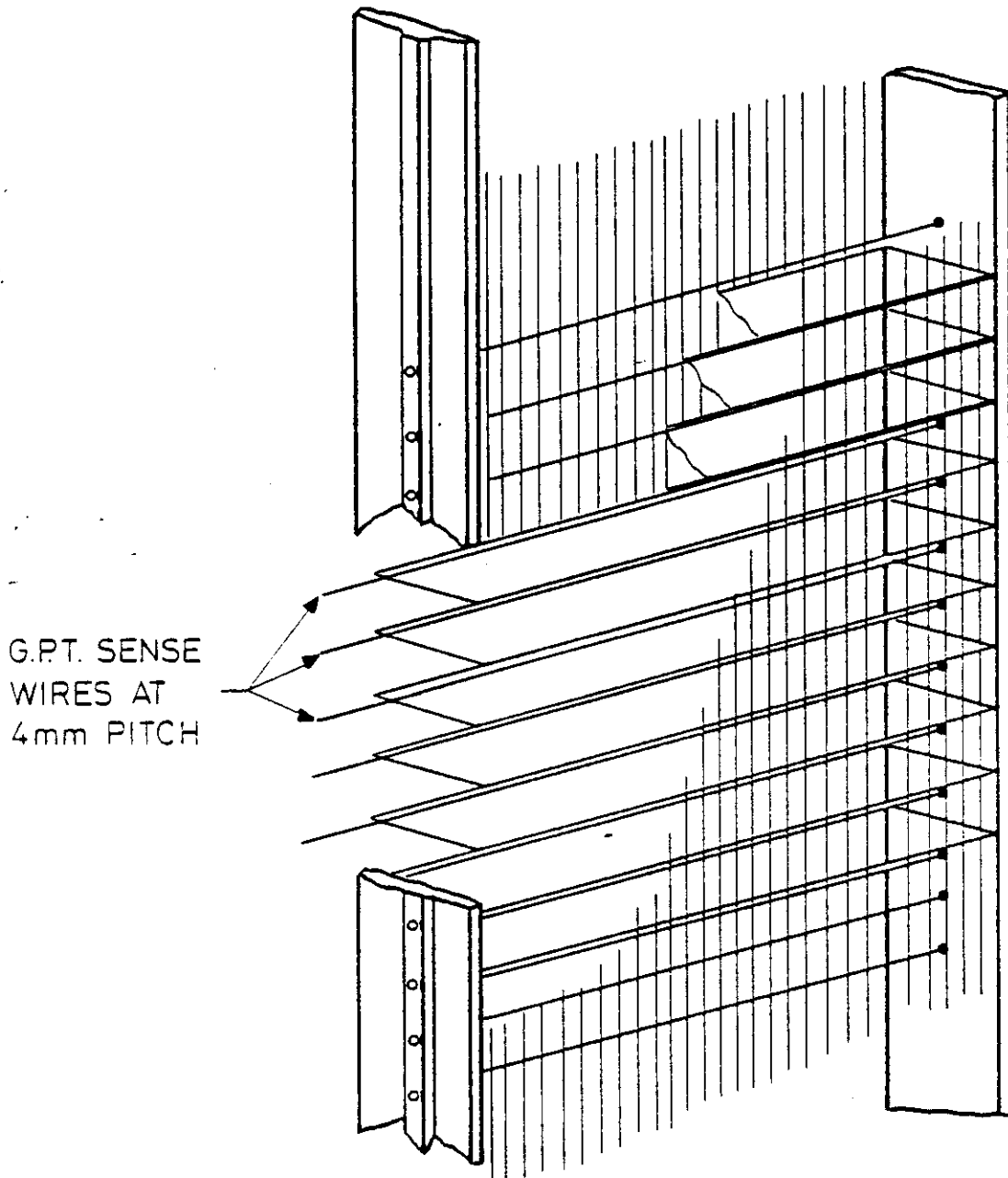


Fig 28

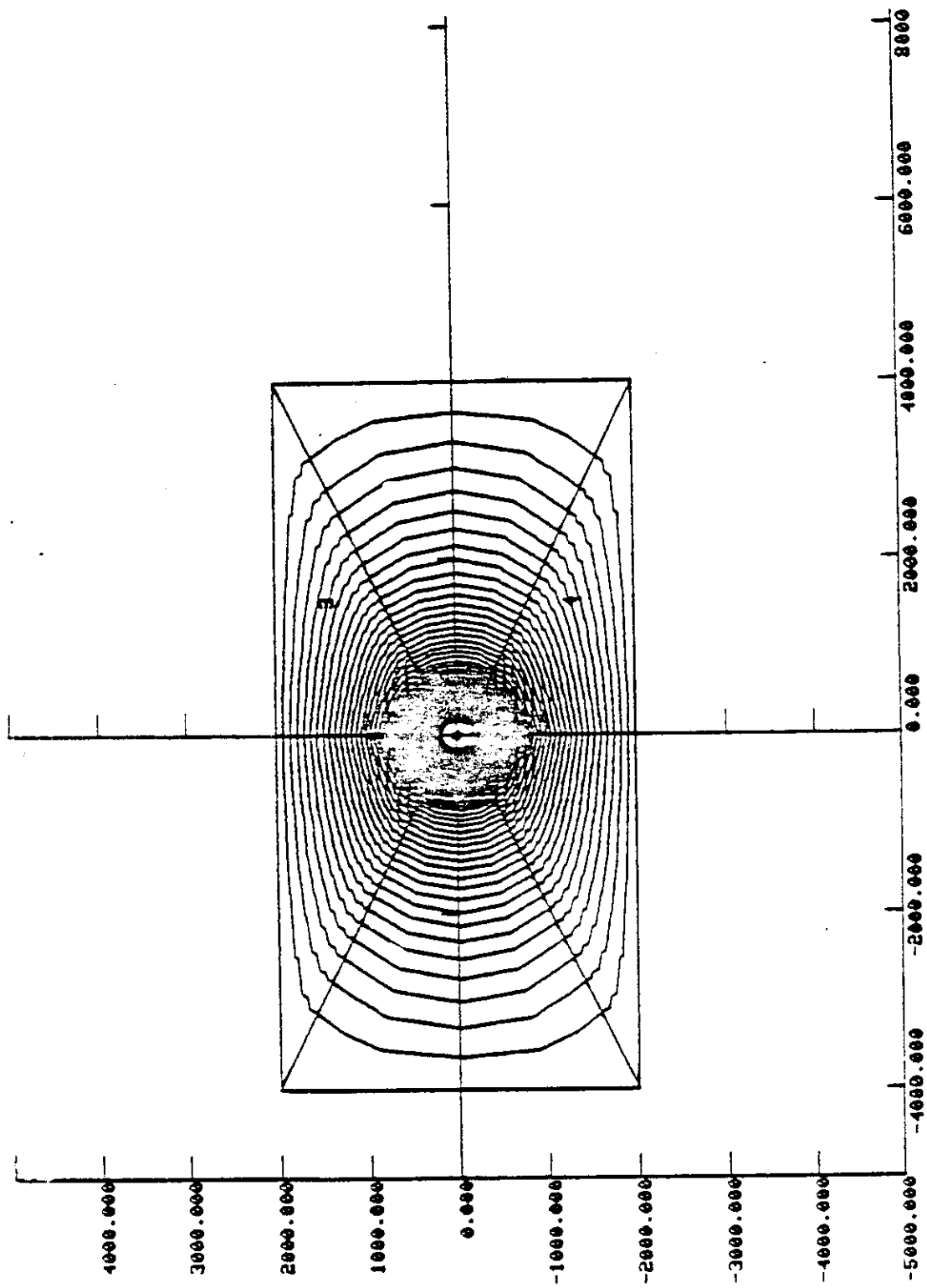


Fig 29

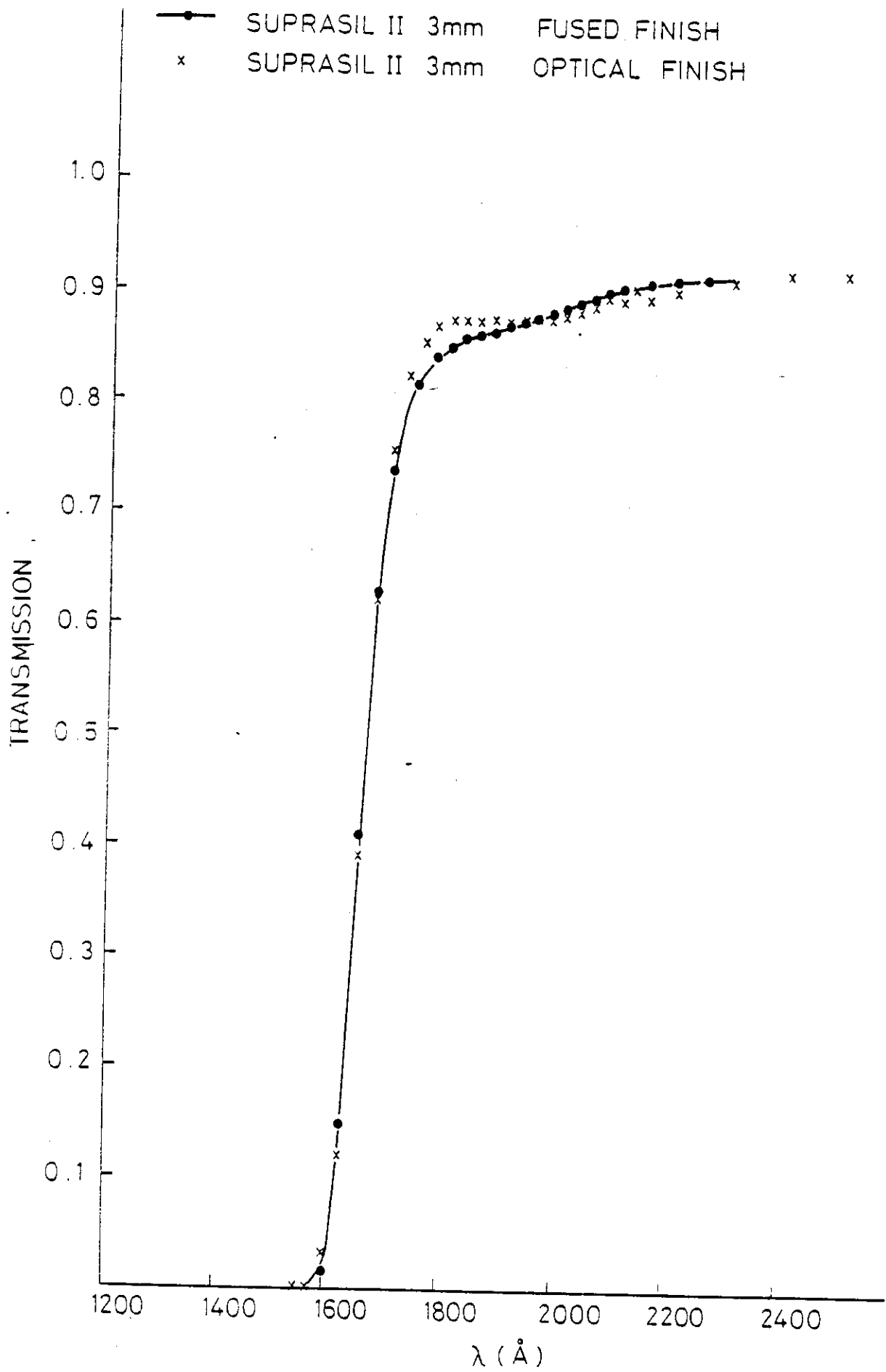


Fig 30

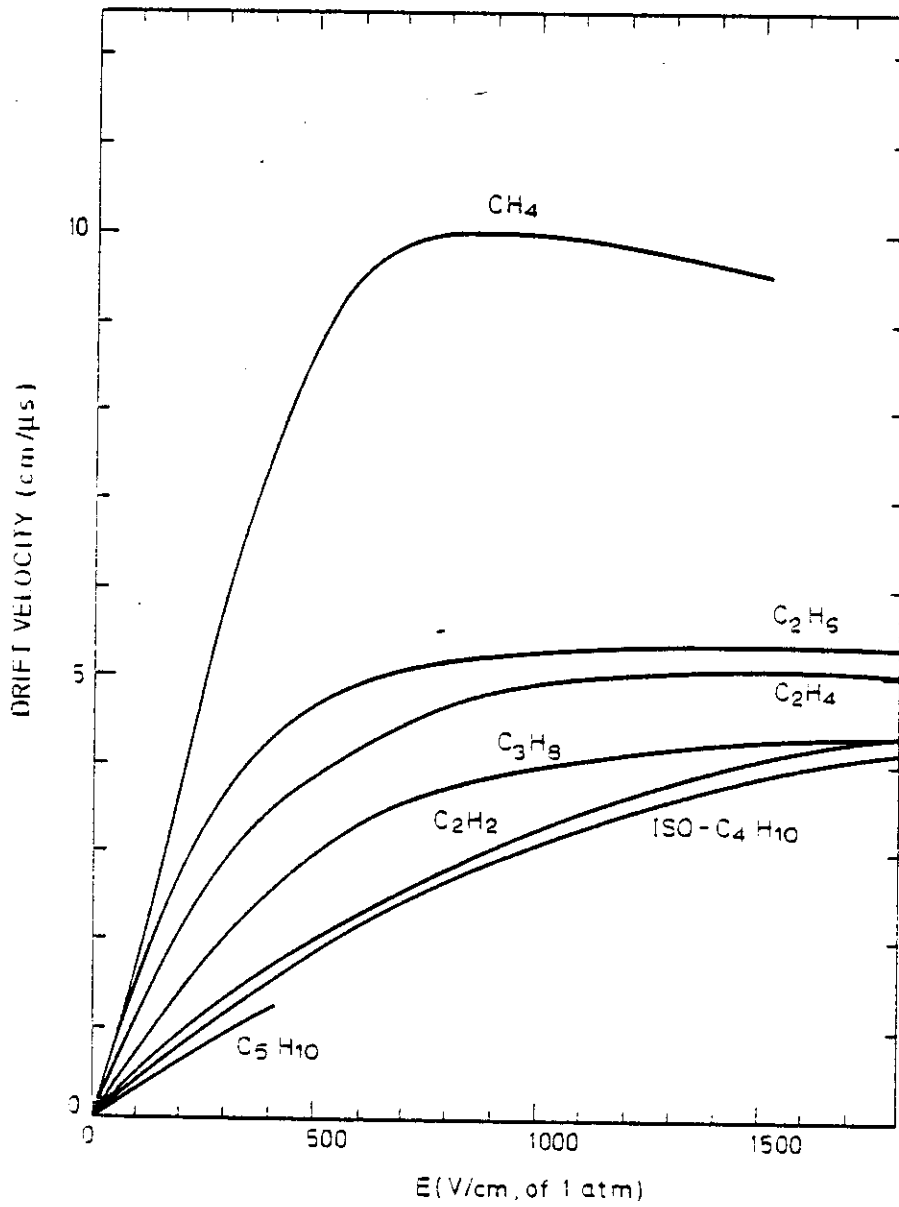


Fig 31

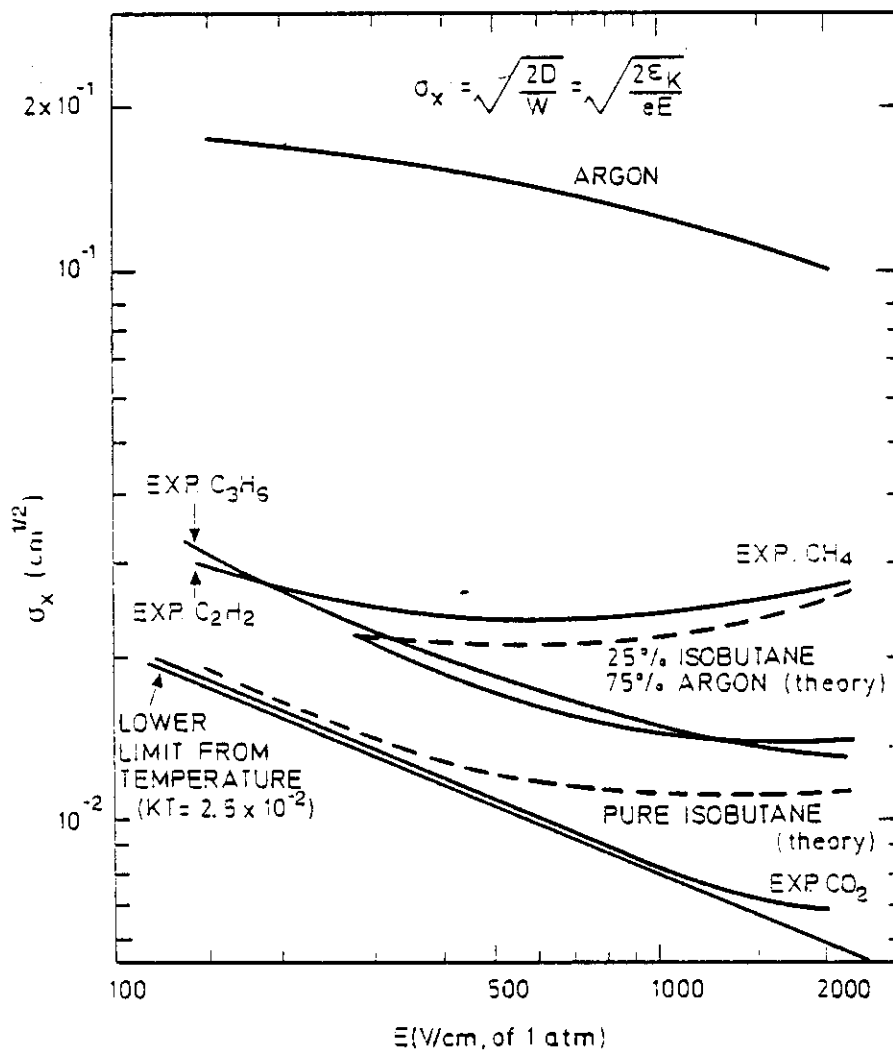


Fig 32

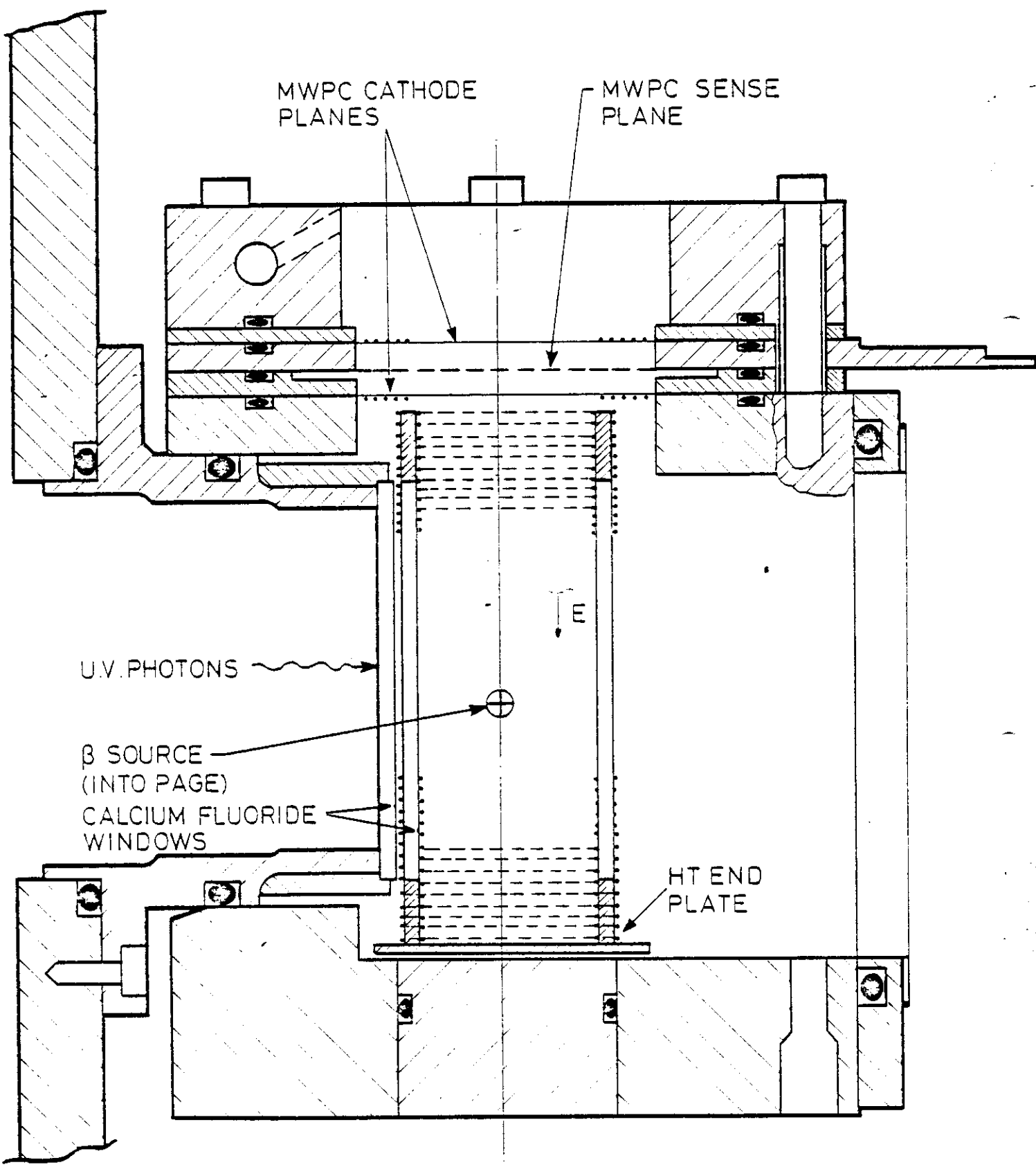


Fig 33

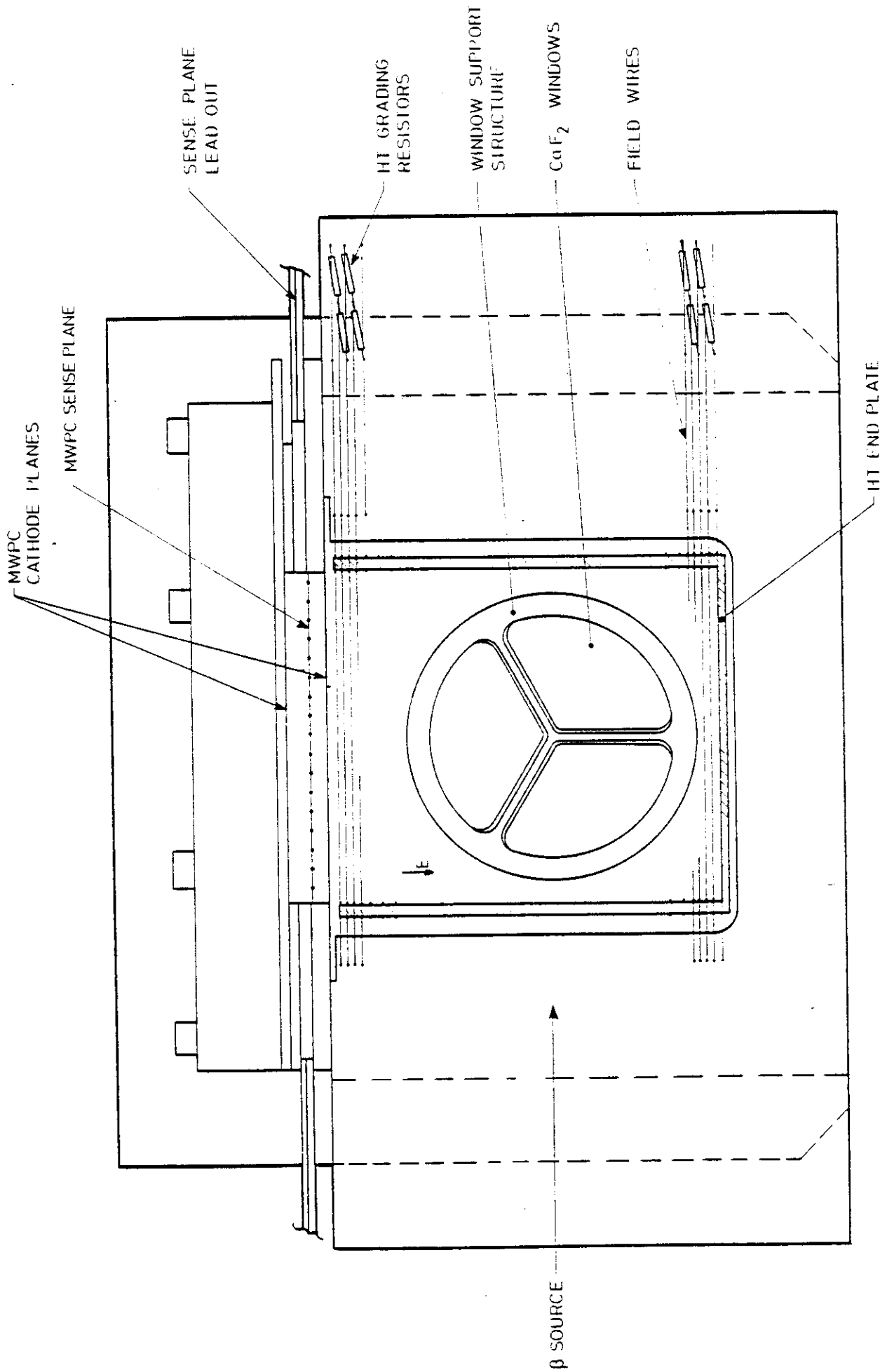


Fig 34

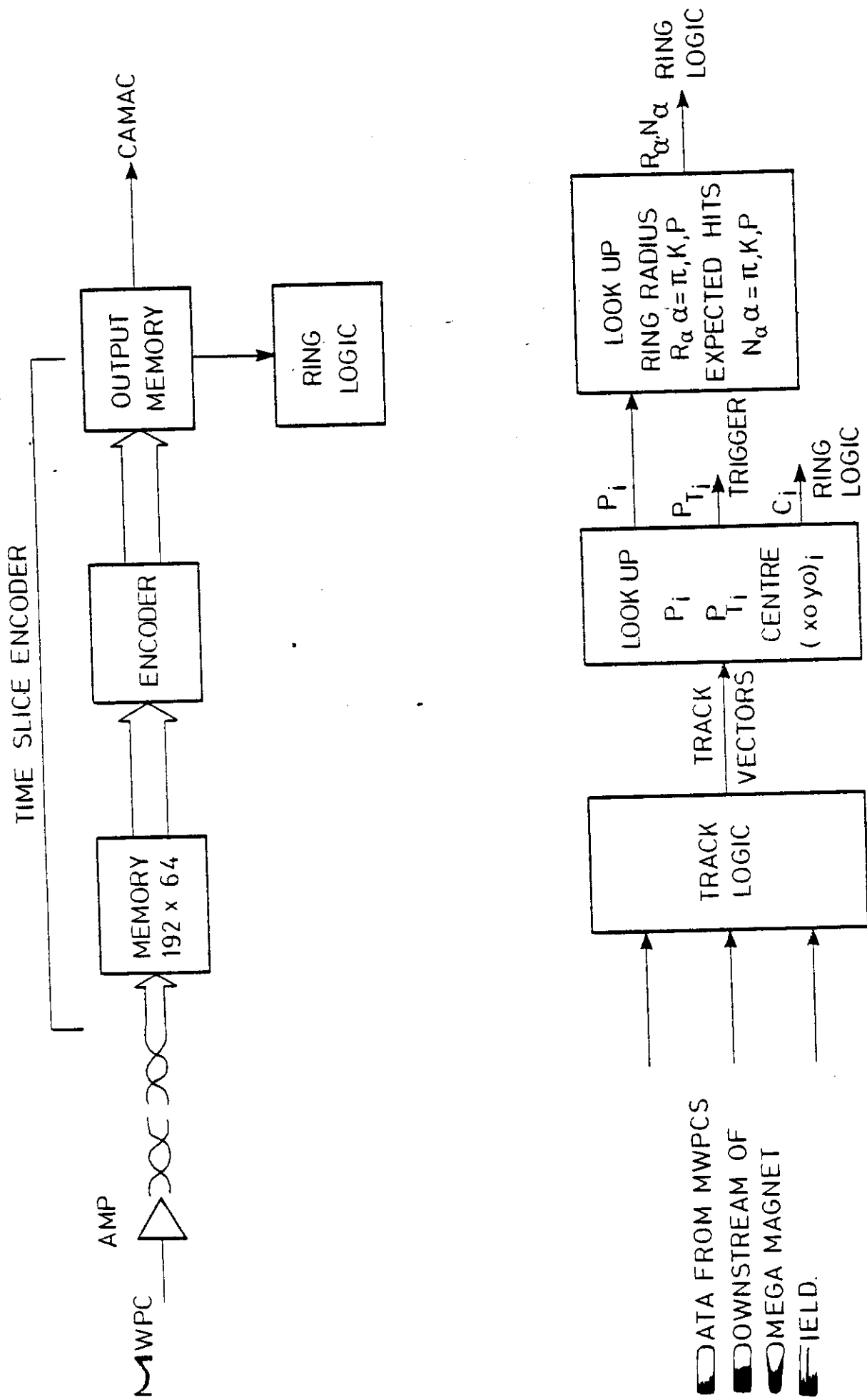


Fig 35

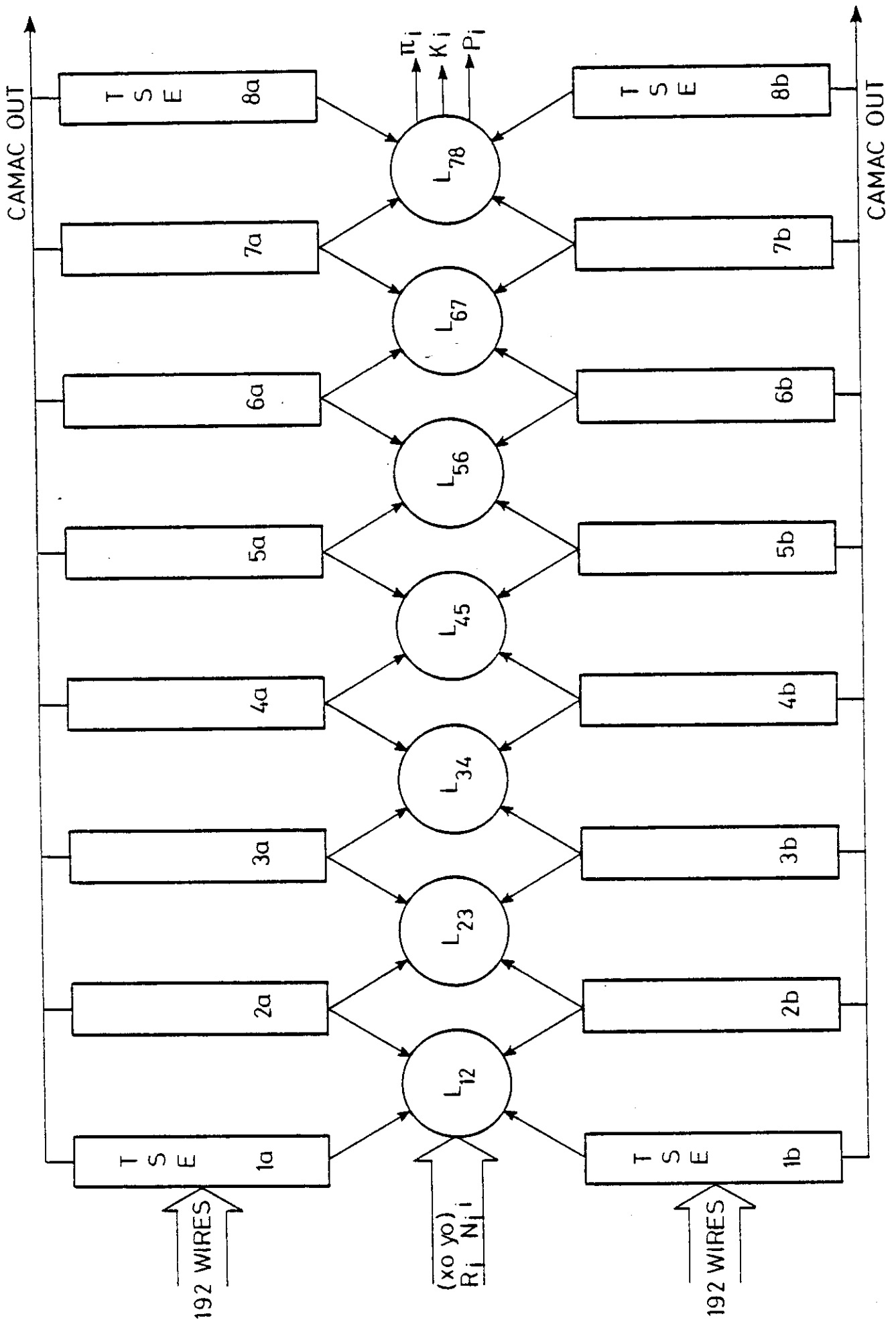
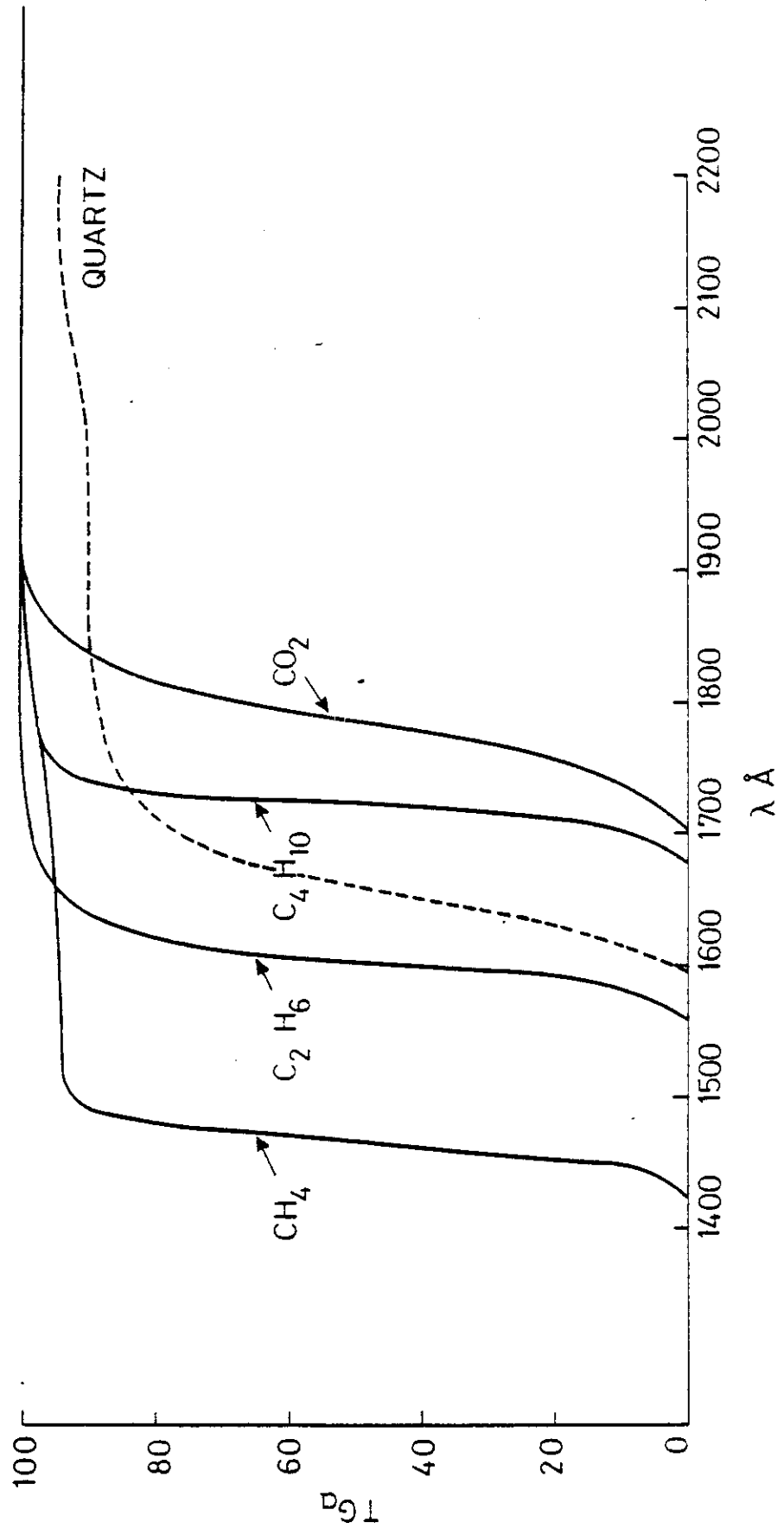


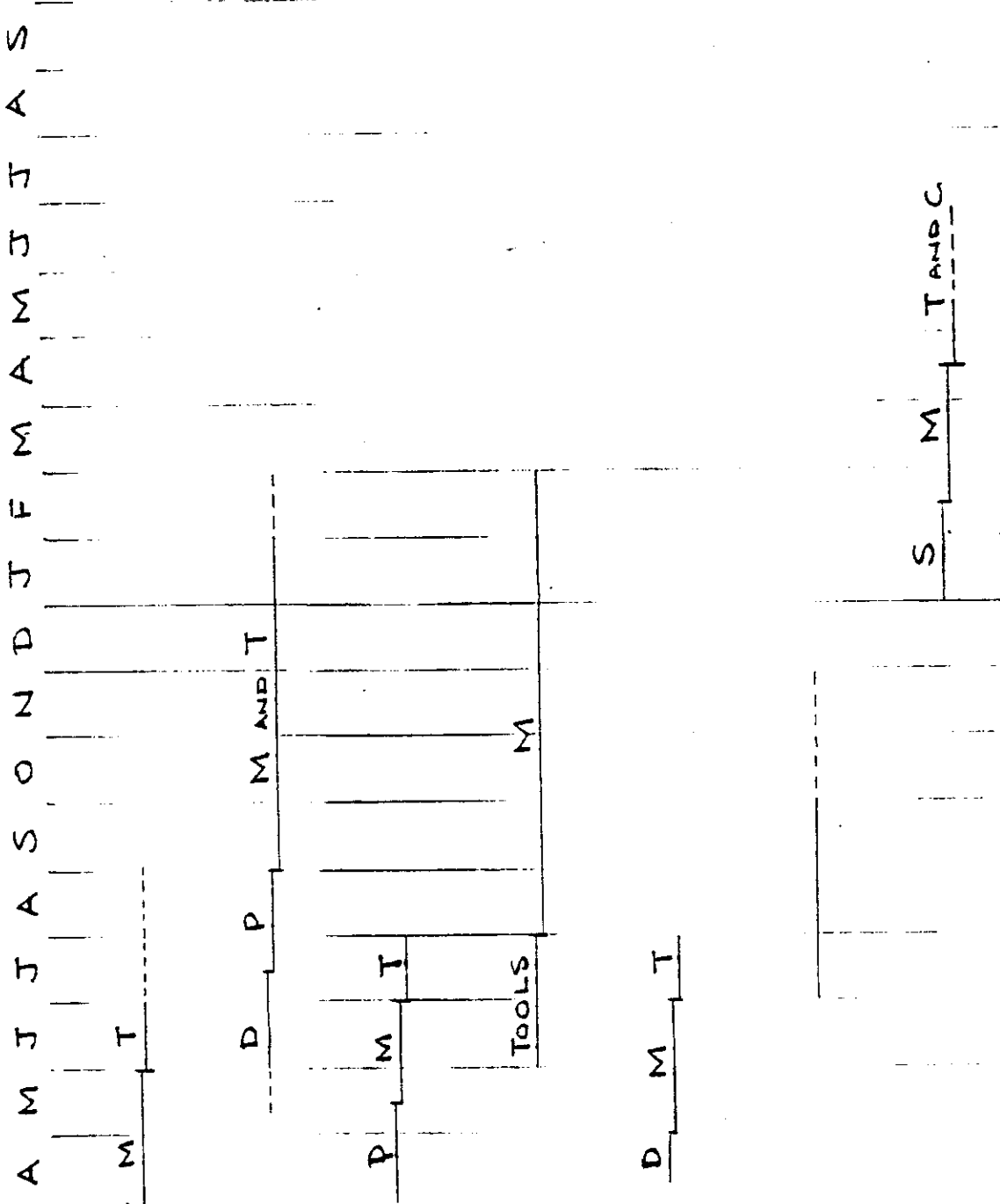
Fig 36



Fig*37

82

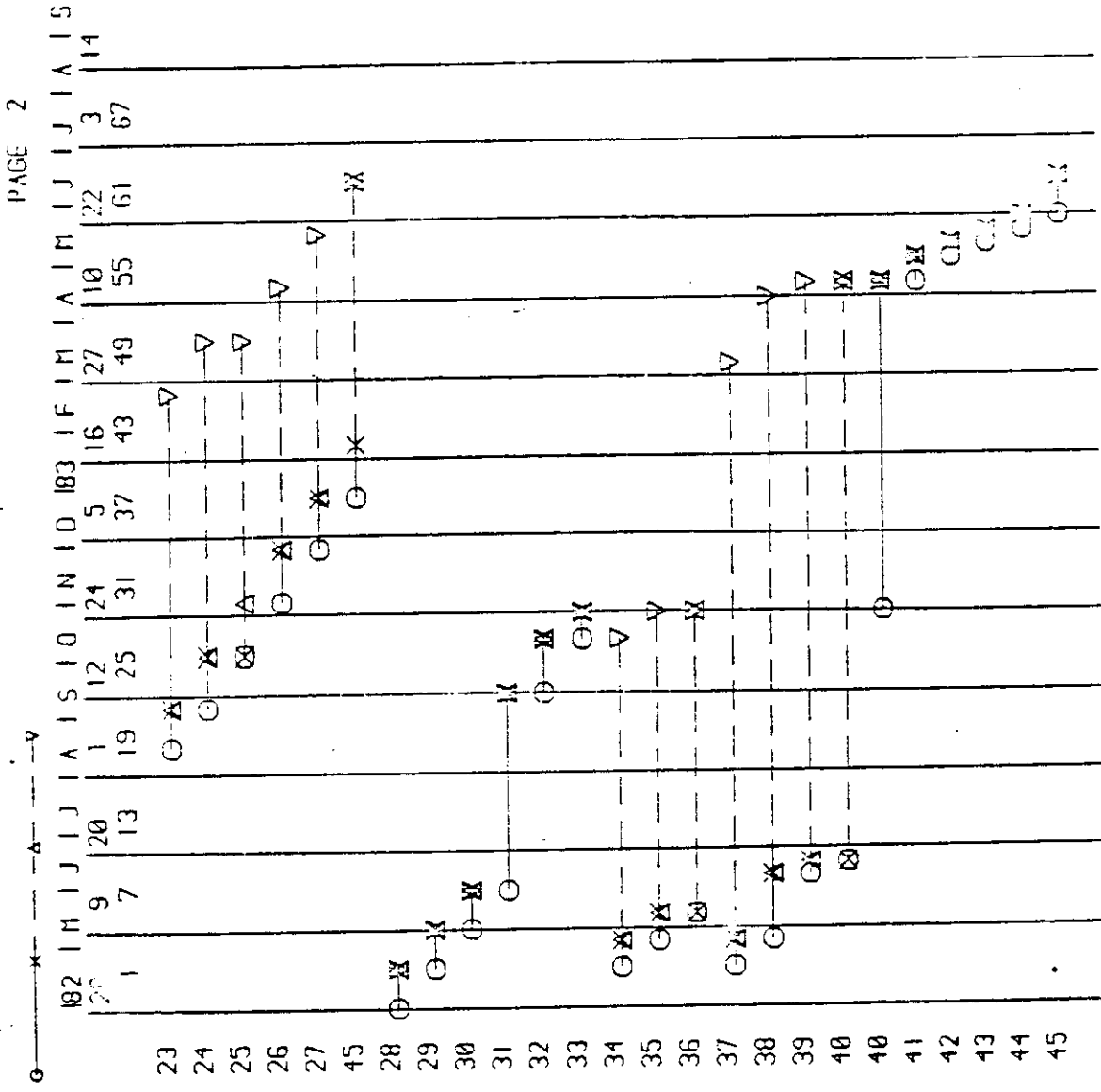
83



- 1. PROTOTYPE T.P.C.
- 2. PRODUCTION T.P.C.
- 3. MIRROR DEV.
- 4. MIRROR MNF.
- 5. BOX DEV.
- 6. BOX MNF
- 7. COUNTER ASSY

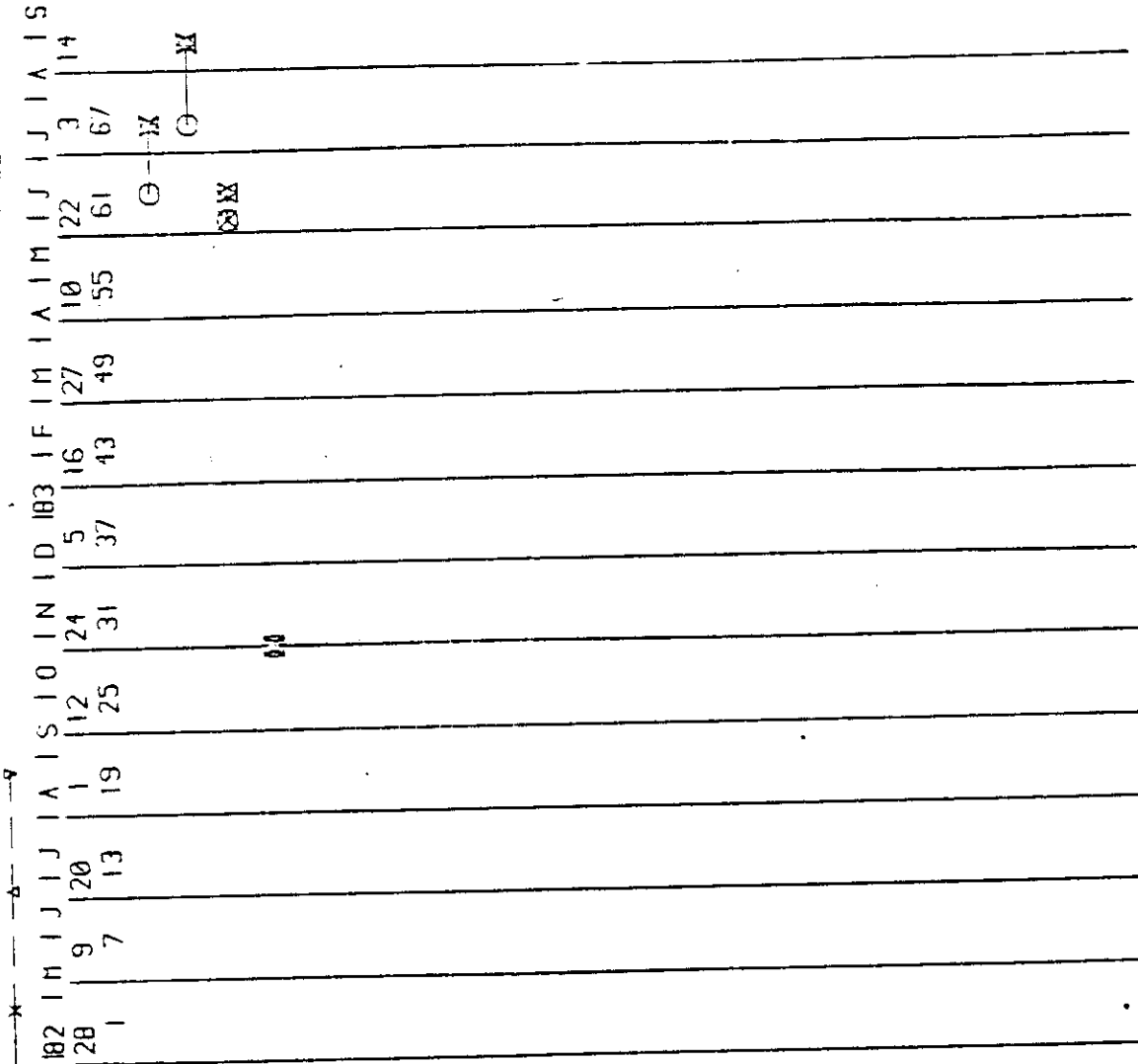
M = MANUFACTURE
 T = TEST
 D = DESIGN AND DRAW
 P = PURCHASE
 S = SHIP TO CERN

PROGRAMME FOR RING IMAGE CERENKOV
 COUNTER PRODUCTION



- 22 23 MNF PARTS
- 23 24 ASSY GAS SYSTEM
- 24 25 DUMMY
- 25 26 GAS TEST BOX
- 26 27 SHIP BOX TO CERN
- 27 45 ASSY COMMISSION BOX
- 1 28 SPEC MIRRORS
- 28 29 DES MIRROR MOULD
- 29 30 ORDER CASTING
- 30 31 MNF CASTING
- 31 32 MACH. CASTING
- 32 33 POLISH CASTING
- 28 34 ORDER GLASS
- 34 35 MNF GLASS
- 35 36 DUMMY
- 28 37 ORDER AL. DISCS
- 37 38 MNF SUPPORTS
- 38 39 GRIND SUPPORTS
- 39 40 DUMMY
- 36 40 DROOP MIRRORS
- 40 41 GRIND MIRRORS
- 41 42 CUT HEXS
- 42 43 COAT MIRRORS
- 43 44 TEST REFLECTIVITY
- 44 45 SHIP MIRRORS TO CERN

Fig 38c



INSTALL MIRRORS TPCS 45 46
 ALIGN MIRRORS TPCS 46 47
 DUMMY 16 45
 DUMMY 33 36

Fig 38d

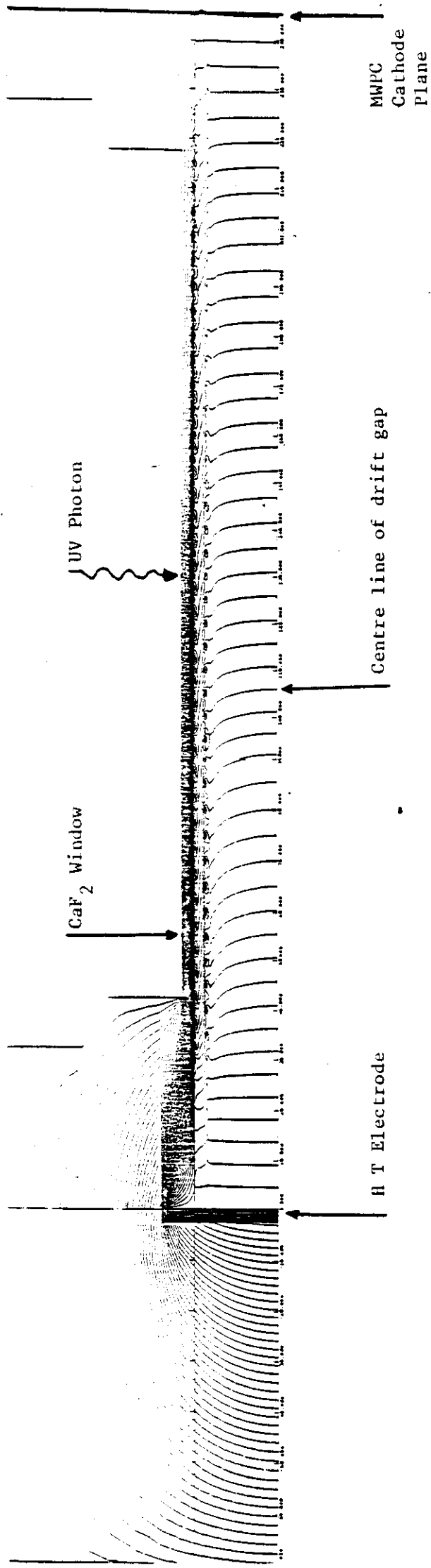


Fig 39

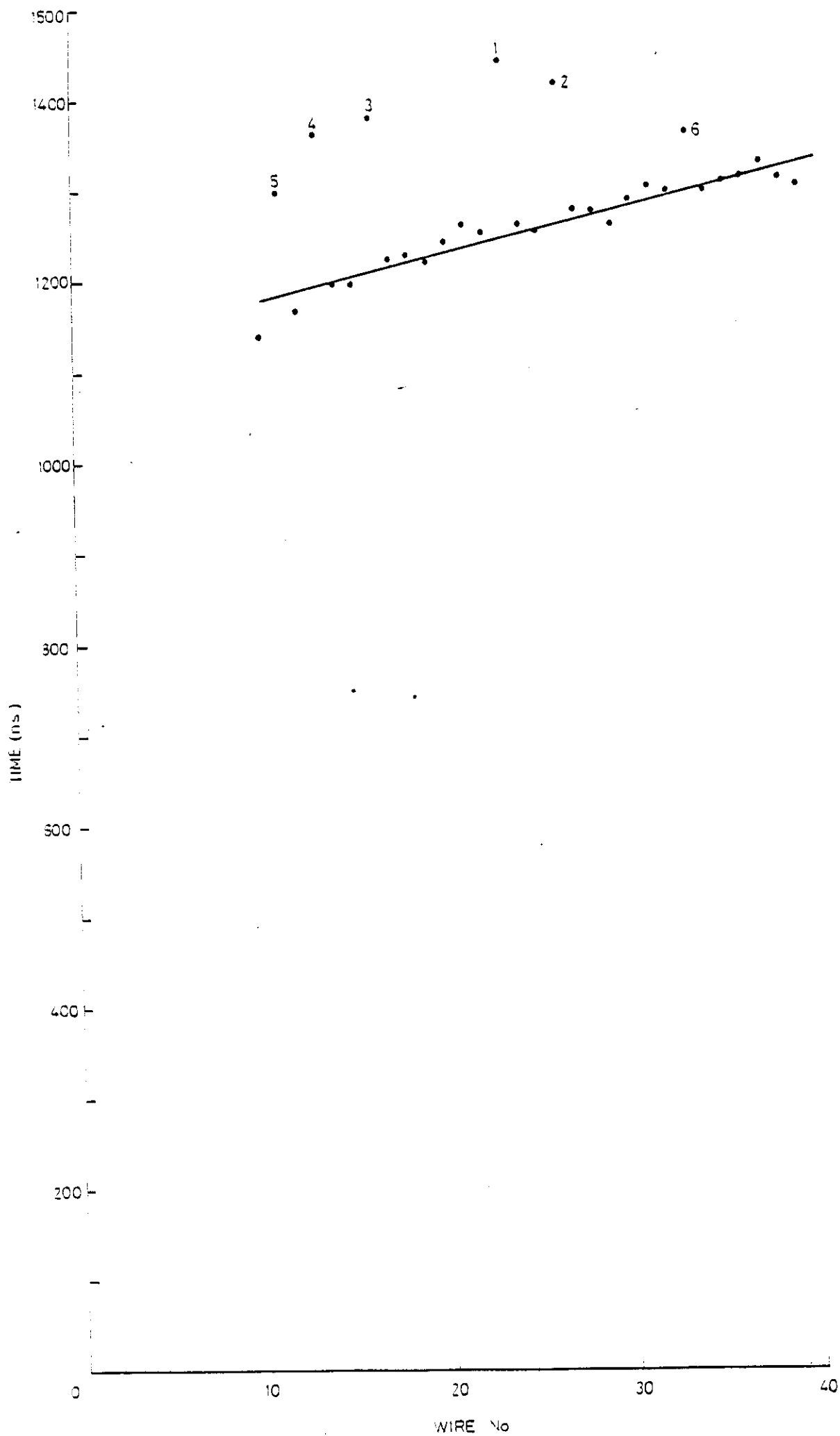


Fig. 40

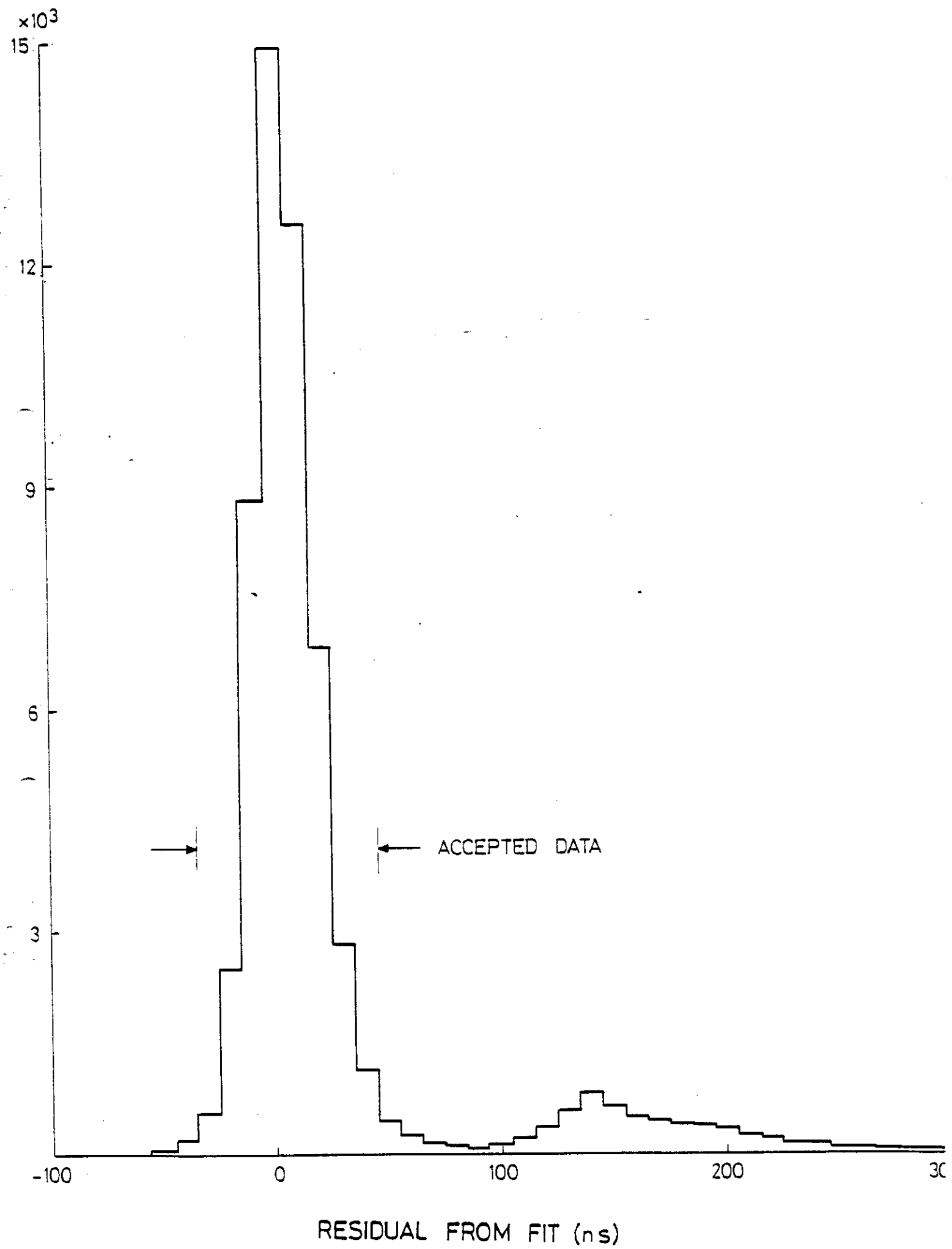


Fig 41

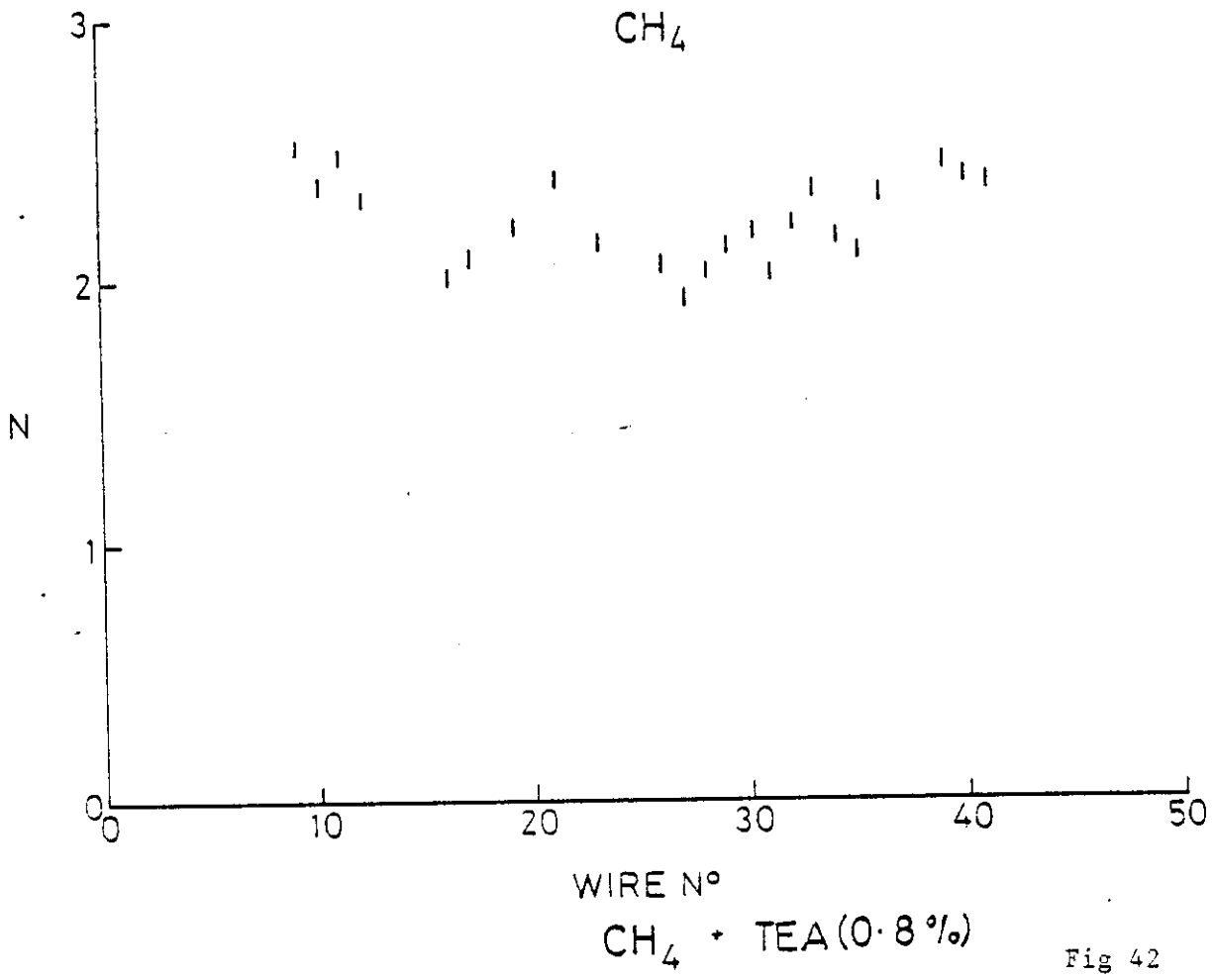


Fig 42

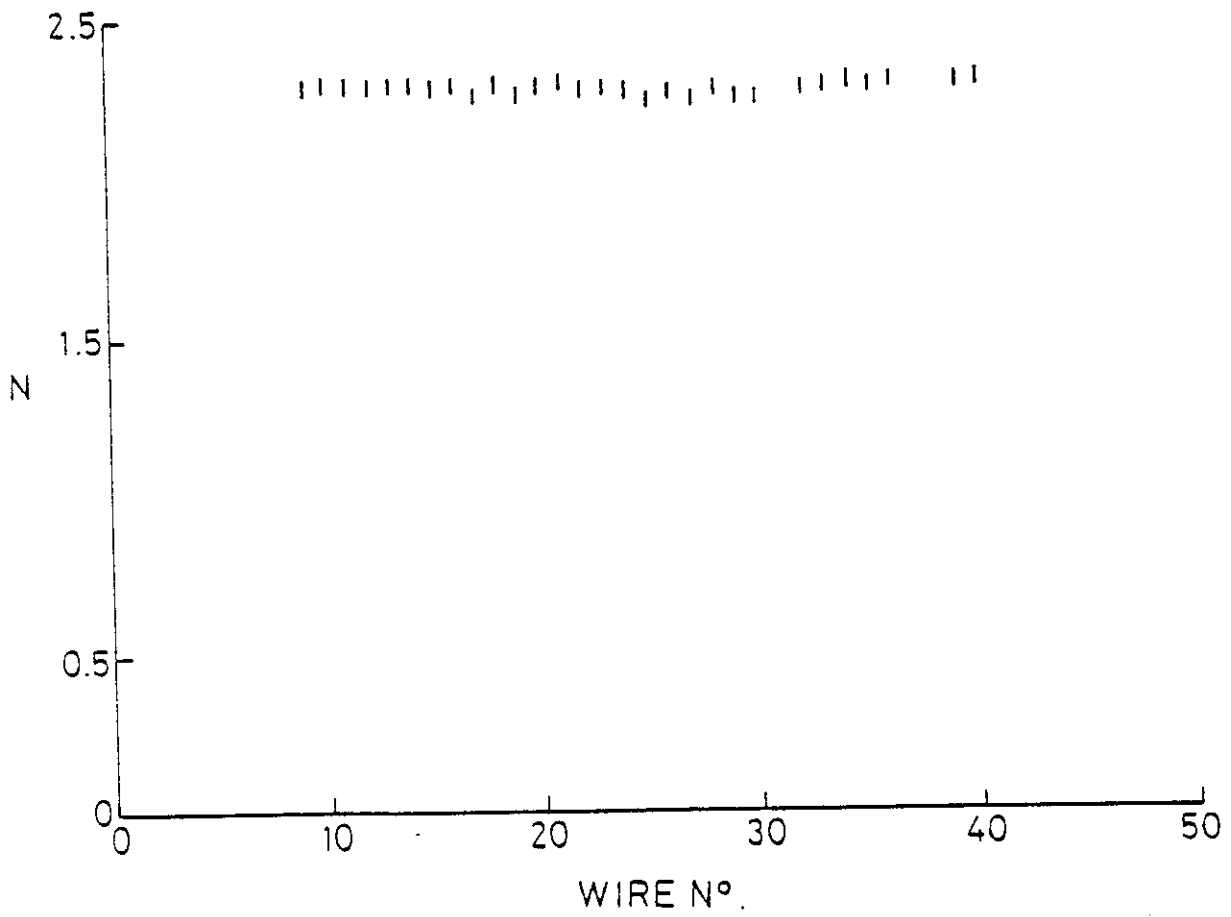
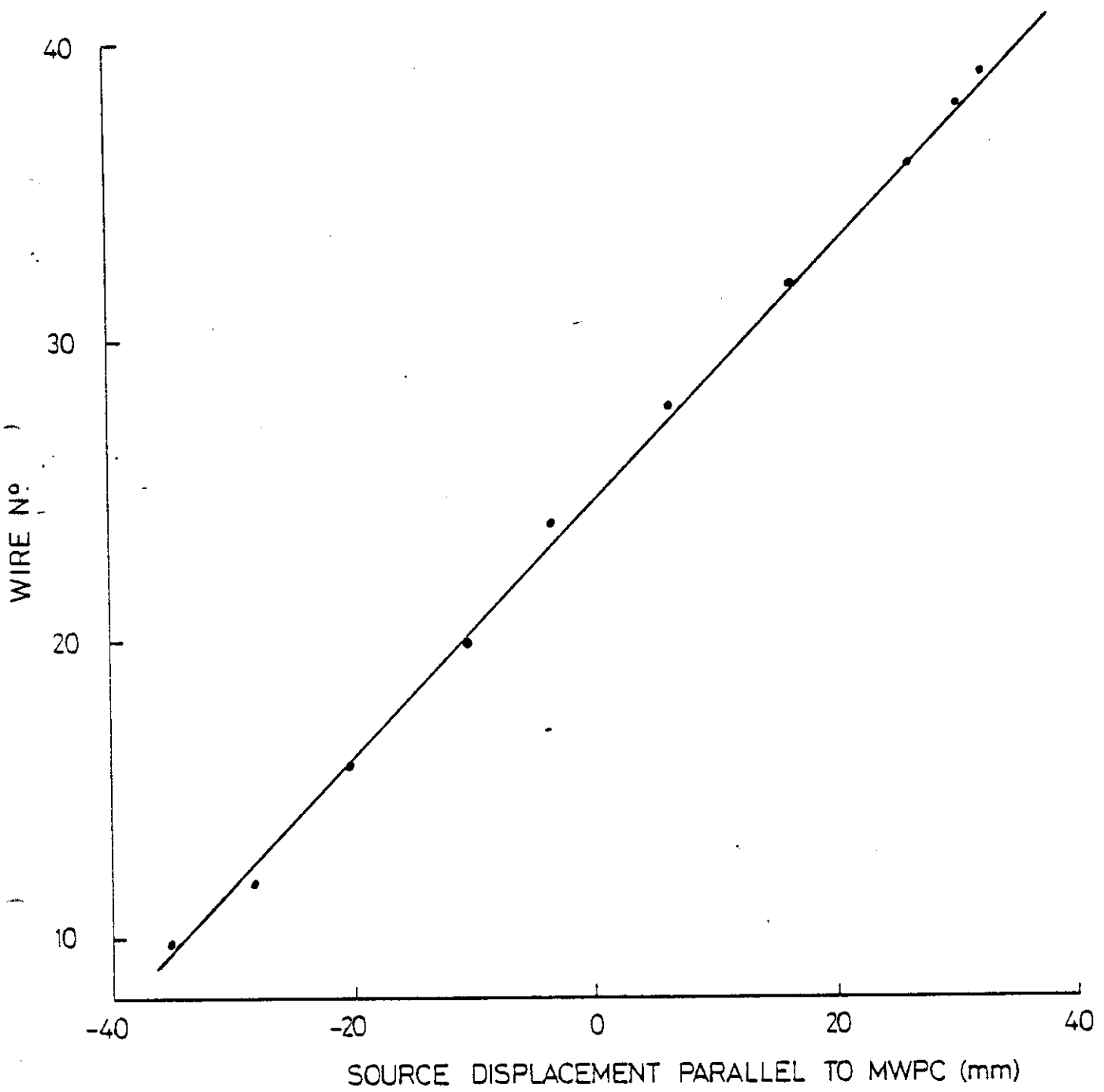
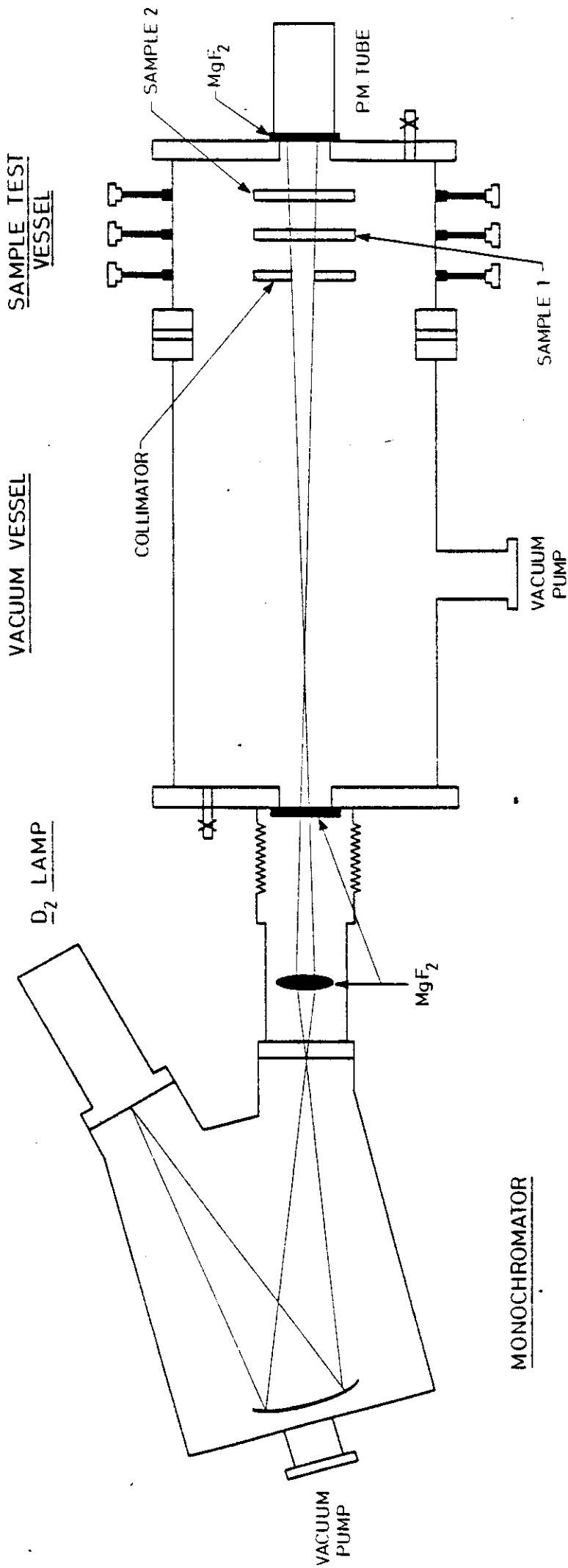


Fig 43



GRAPH OF WIRE NO Vs. DISPLACEMENT FROM CENTRE LINE OF A SOURCE 60mm FROM THE WIRE PLANE AND PARALLEL TO IT.

Fig 44



LAYOUT OF U-V TRANSMISSION MEASUREMENT SYSTEM

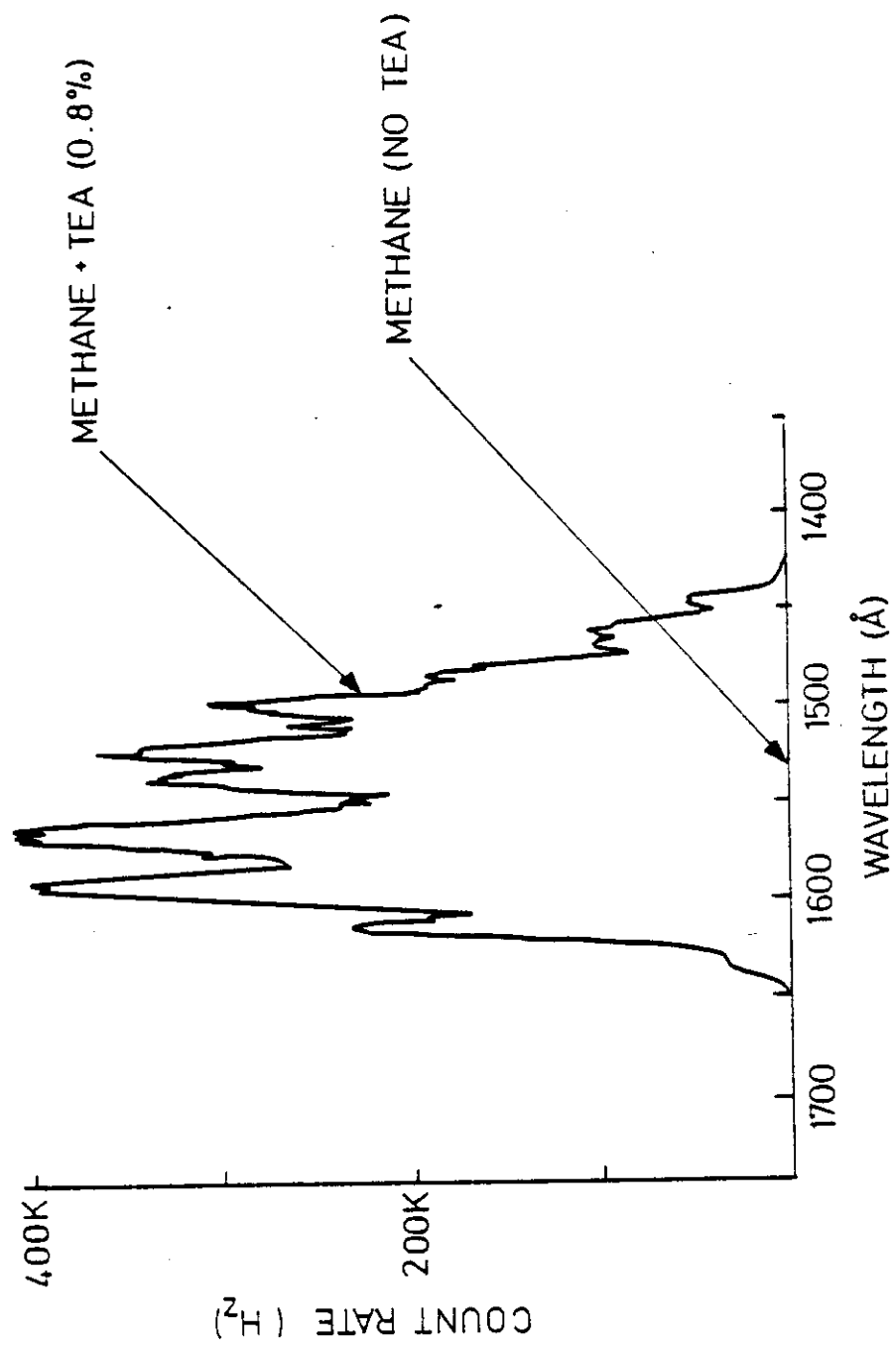


Fig 46

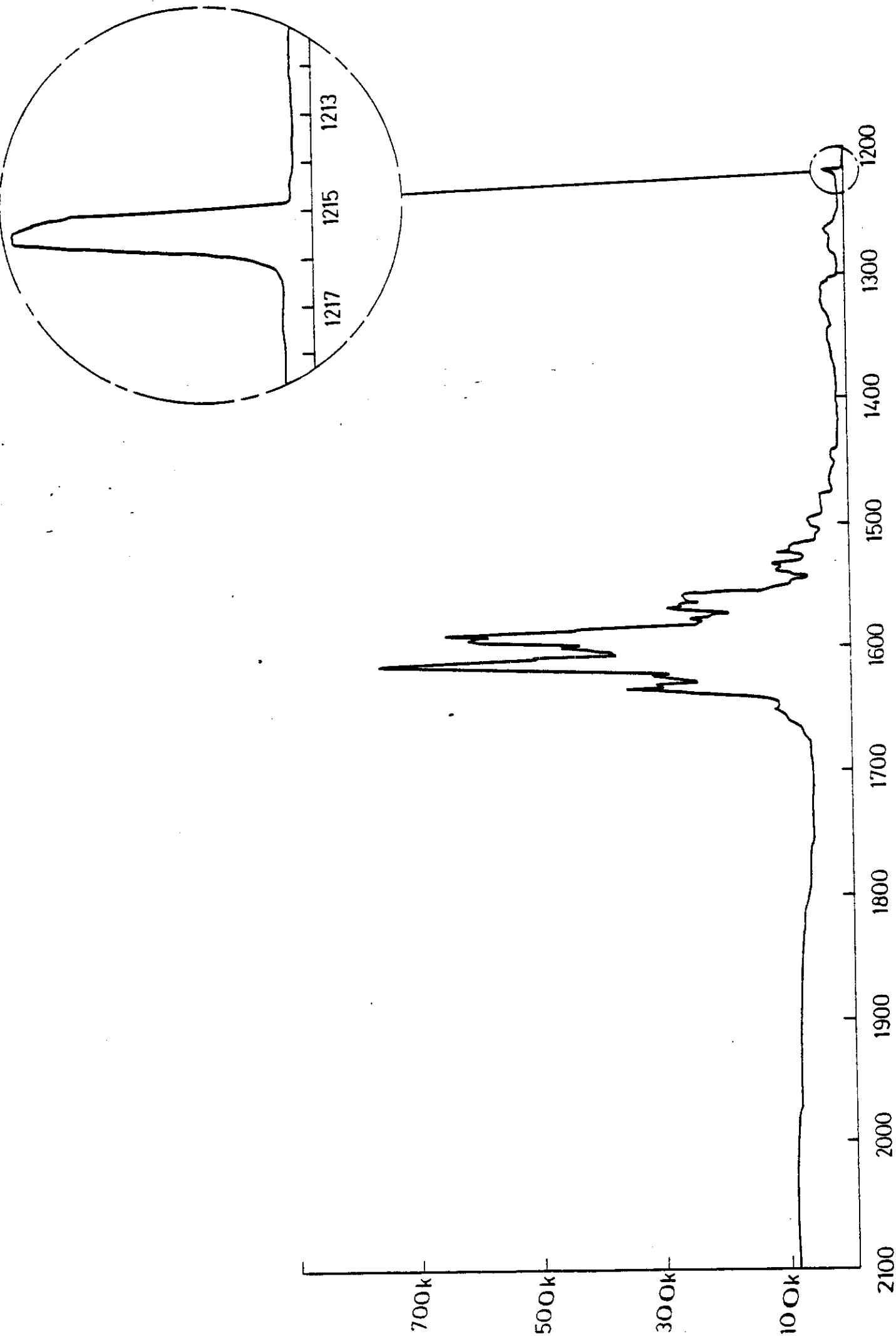
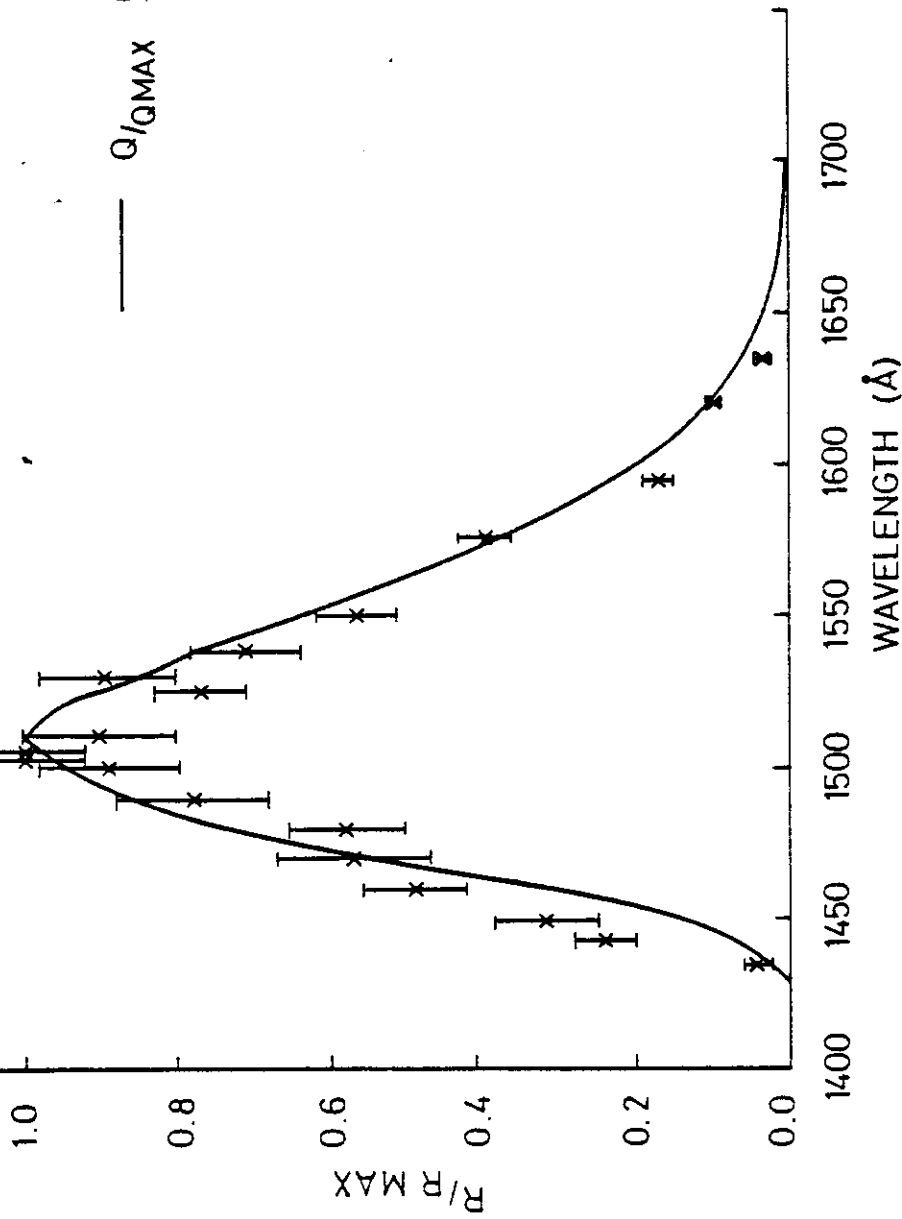


Fig 47

WAVELENGTH (Å)

TPC FILLED CH₄/TEA (0.8%)

— Q/Q_{MAX} CH₄/TEA - YPSILANTIS



RATIO OF BEAM INTENSITIES FROM TPC AND PHOTOTUBE
(BOTH CORRECTED FOR TRANSMISSION LOSSES IN WINDOWS)

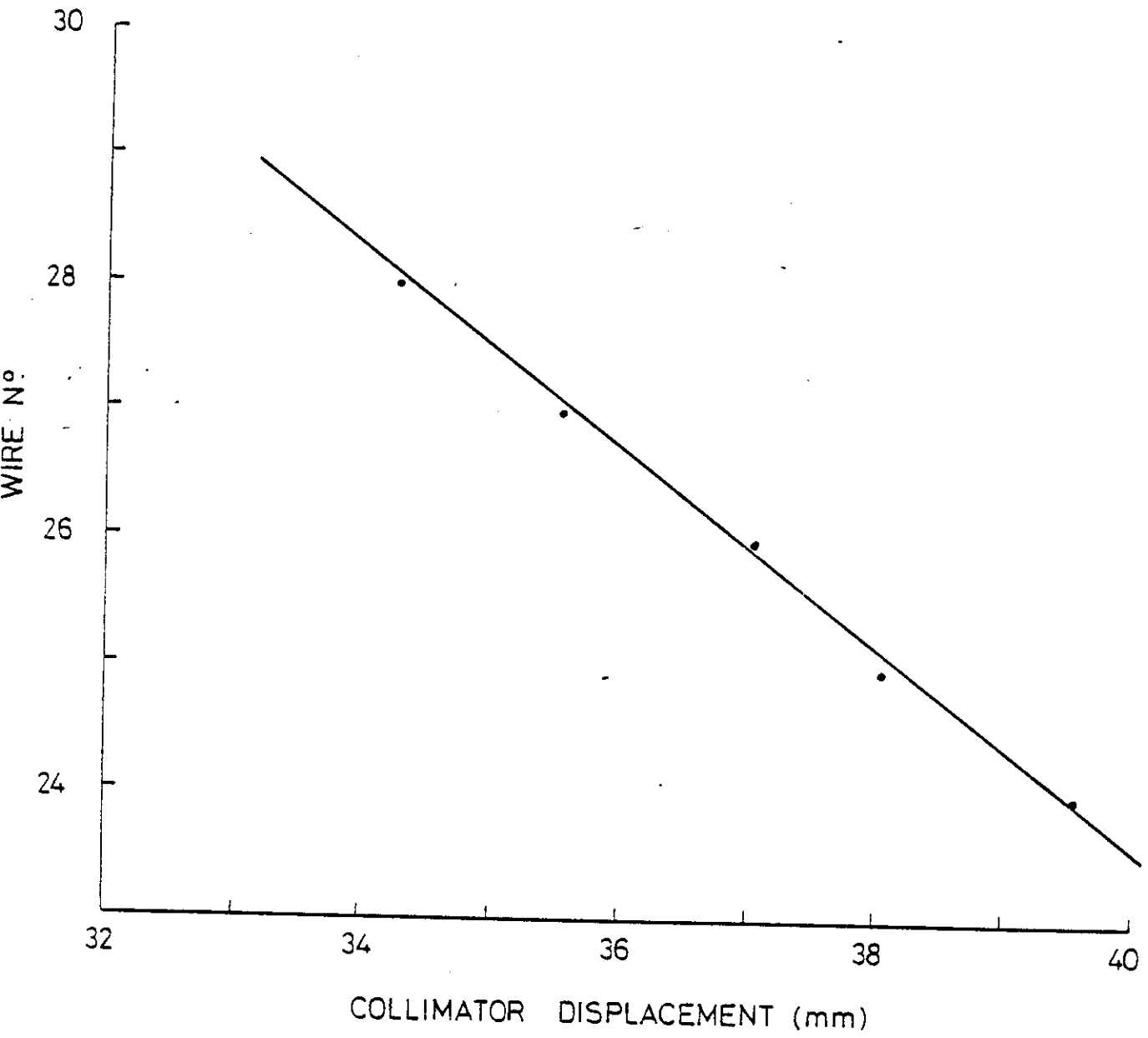


Fig 49

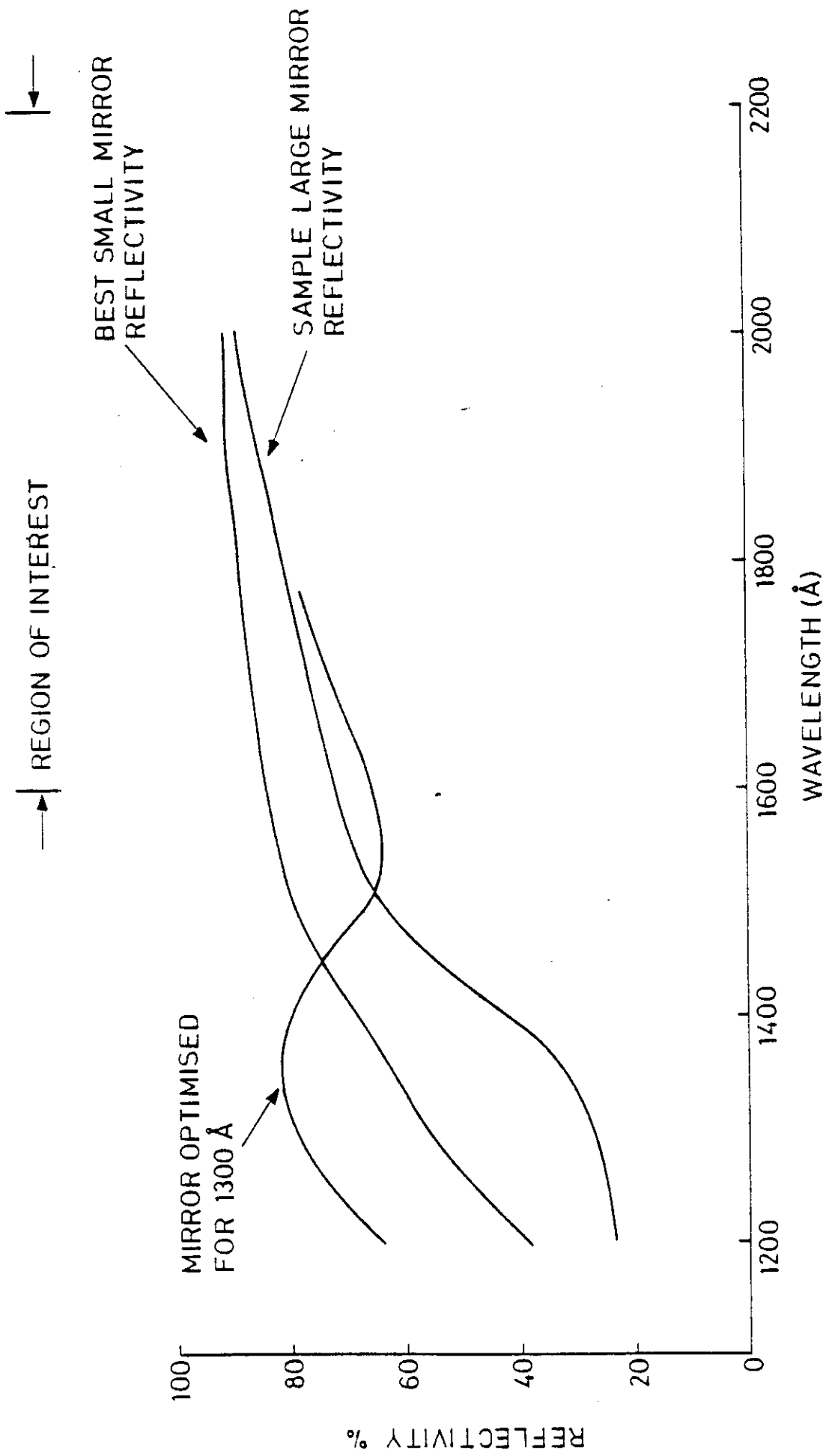


Fig 50

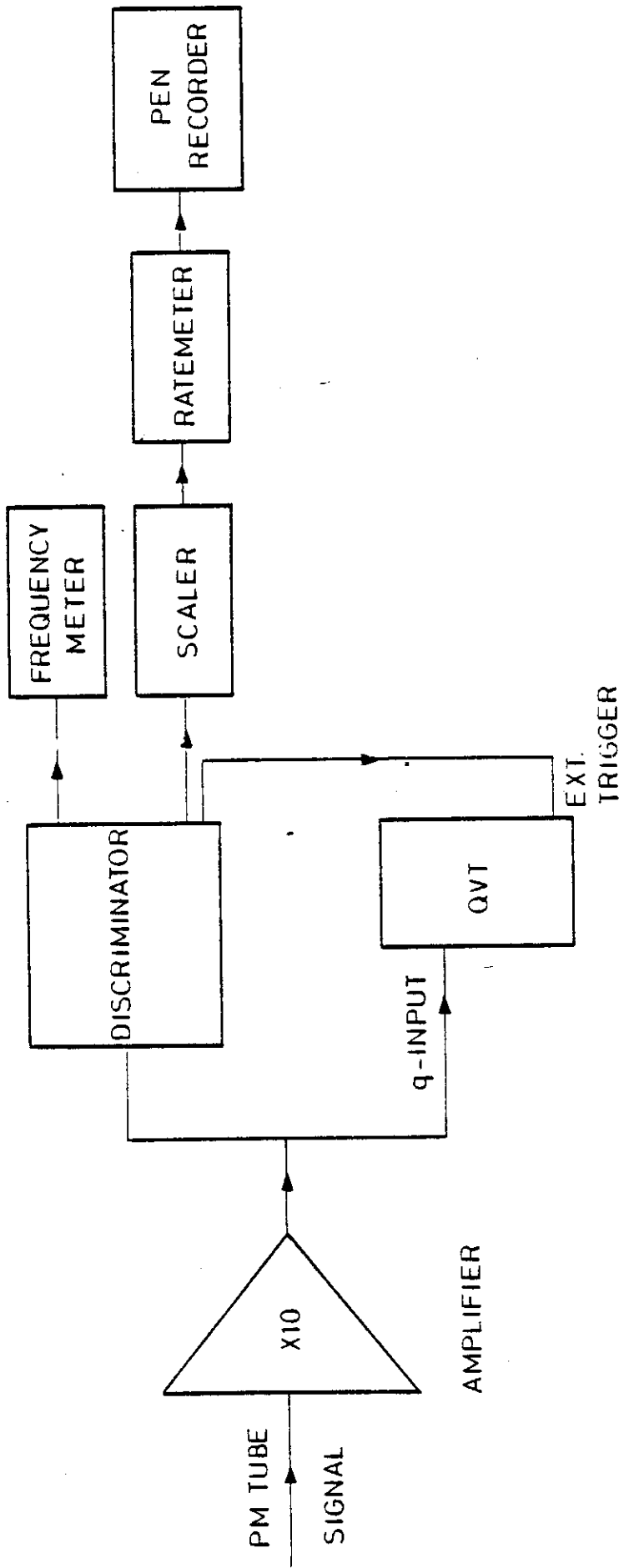


Fig 51

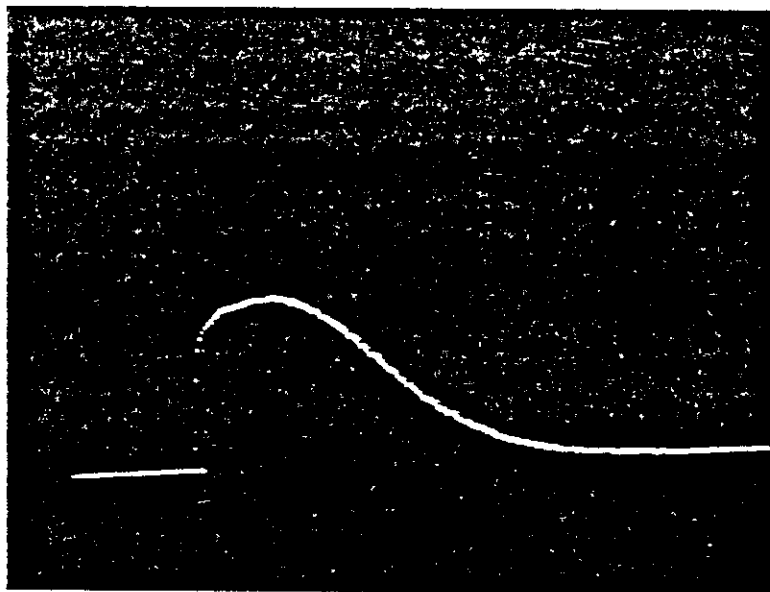
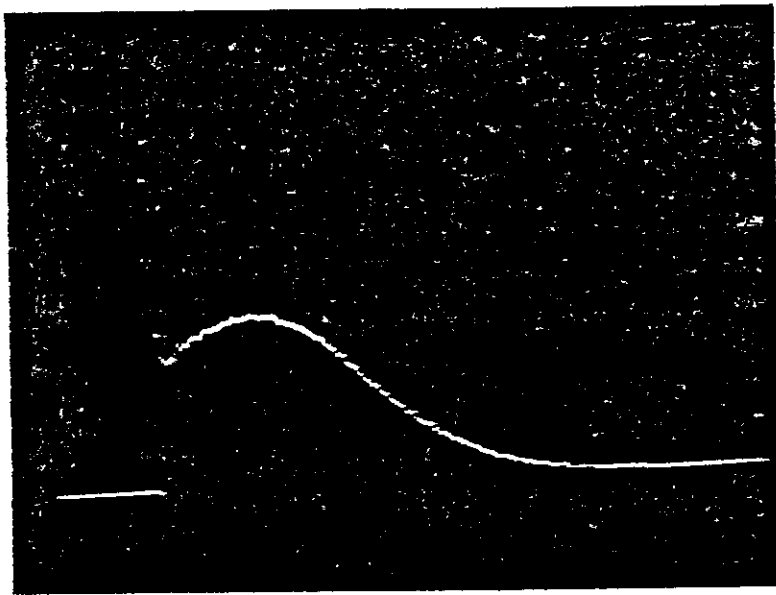
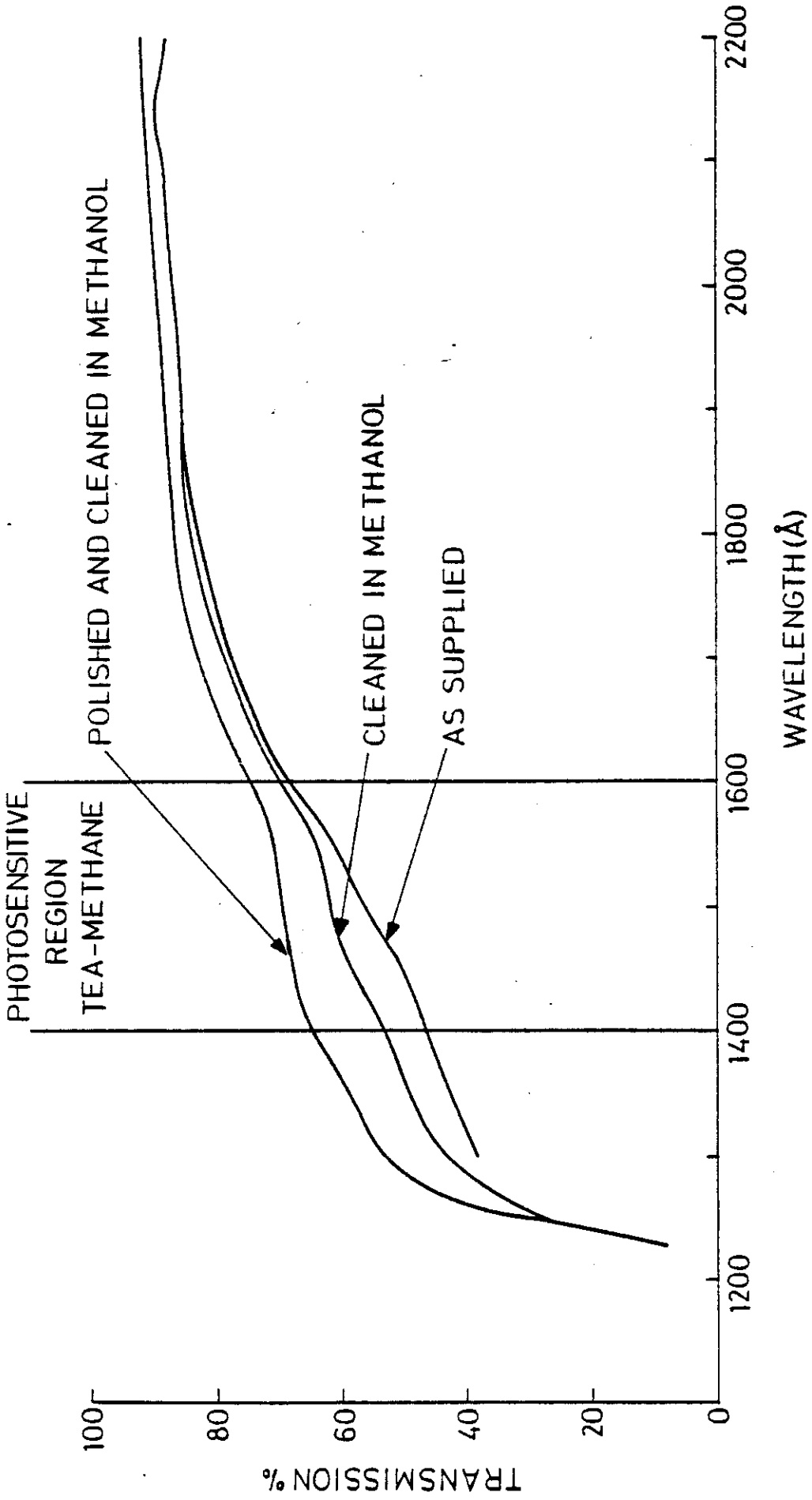
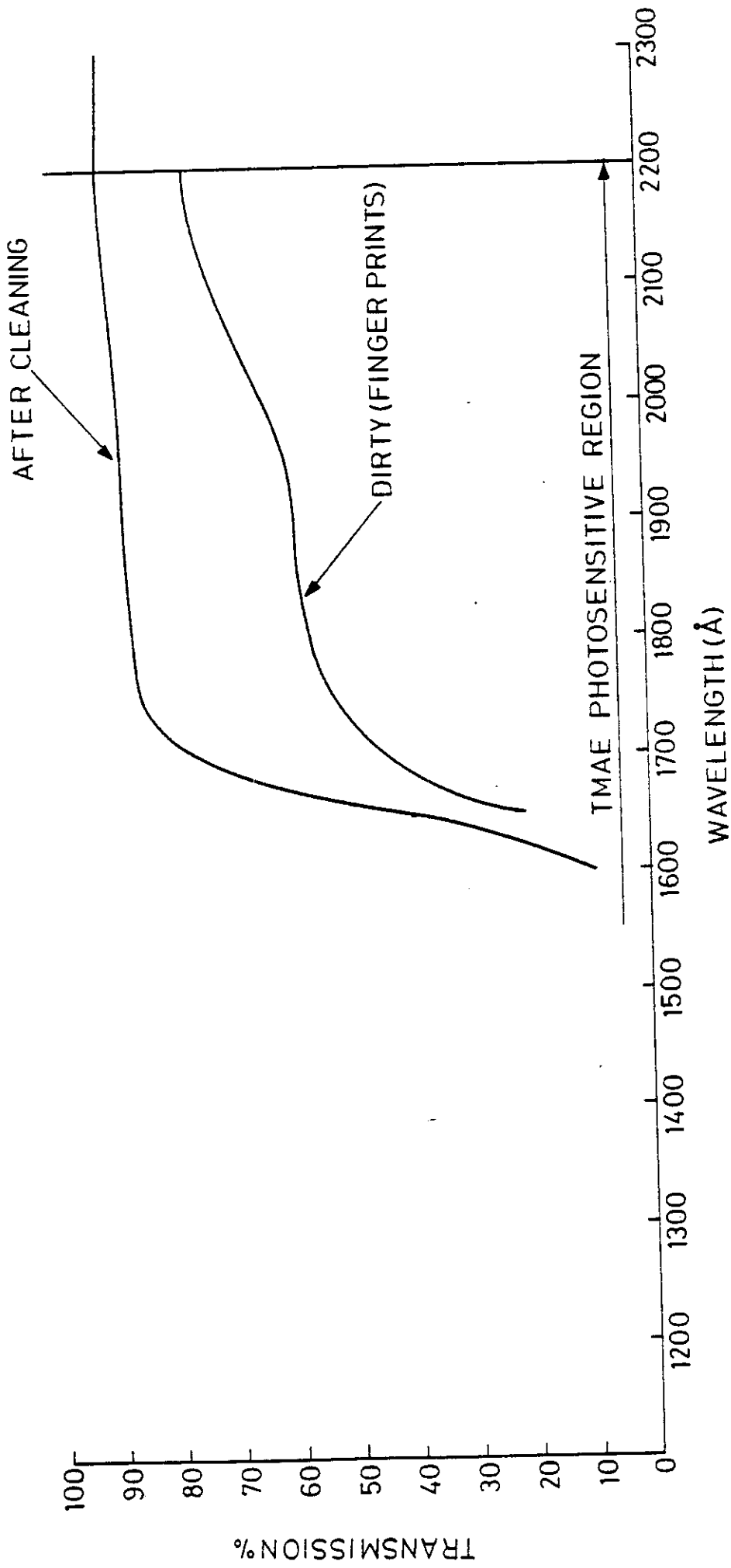


Fig 52



TRANSMISSION OF 3mm CdF₂



TRANSMISSION OF 3mm SUPRASIL II